Application of Wavelet Analysis for Examining Climate and Meltwater Runoff in the Paakitsoq Region, West Greenland

Jonathan D. Fuhrmann

Girton College

14th June 2012

UNIVERSITY OF CAMBRIDGE

M.Phil. in Polar Studies

This dissertation is submitted for the degree of Master of Philosophy

Scott Polar Research Institute
University of Cambridge

Girton College
University of Cambridge

I. Statement

This Dissertation was essentially the author's own work. All support and advice received is documented in the acknowledgements. The maximum permitted length of 20,000 words was not exceeded. Using the word count tool in Microsoft Word 2007, the length of this Dissertation was determined to be 19,316 words. This includes chapter and sub-chapter headings, references, citations, quotations and formulae. This number excludes this statement, the bibliography, appendices, abstracts, preface, acknowledgements, the table of contents, lists of tables and variables, and all graphs and tables as well as their captions.

The Appendices attached to this project contain figures which are essential to the dissertation rather than supplementary information, but their size and multitude would disrupt the flow of the text if included in the body of the dissertation. It is hoped that their presentation in the Appendices will facilitate the reading of this dissertation.

Jonathan Daniel Fuhrmann

14 June 2012

II. Abstract

Land-terminating areas of the Greenland ice sheet have experienced significant mass loss over the last two decades, and a feedback between surficial meltwater production, resultant basal lubrication and ice-sheet flow velocity during the summer ablation season has been suggested as an explanation. Meteorological conditions have long been known to be an important driver of surface melt, and the seasonal acceleration pattern observed in Greenland is overlaid by shorter trends as well as diurnal fluctuations and even shorter one-off discharge and acceleration peaks. This project aims to investigate the relationship between net shortwave radiation, air temperature and proglacial discharge using wavelet analysis in order to establish the variability of discharge on short (<1-3 days) timescales and how this is driven by meteorological factors on similar (<1-4 days) timescales. Wavelets produce a high-resolution breakdown of the time series in the frequency domain, allowing for a study which is continuous in three dimensions: time, frequency and power of variability. Both univariate and multivariate analyses are performed, providing an improvement over conventional time-series analysis which requires data to be split into arbitrary sections if these are to be analysed separately. Diurnal fluctuations are found in each of the time series analysed, although their magnitude and the duration and consistency of their presence varies both between series and years. The relationships between air temperature and discharge and net shortwave radiation and discharge are found to differ. Air temperature covaries with discharge on shorter timescales (up to 1 day) while net radiation exhibits stronger coherence with discharge on longer timesclaes (3-4 days).

III. Acknowledgements

I would like to express my heartfelt thanks to the following people, without whom this dissertation would not have been possible:

My supervisor, Dr Ian Willis, for his invaluable insight, advice and suggestions;

Dr Ruth Mugford, Alison Banwell, Dr Cameron Rye (Oxford University) and Dr. Gareth Rees for their help with various data and software issues;

Dr Nick Kingsbury at the Department of Engineering, University of Cambridge, for his help with signal processing theory;

My fellow MPhil students, for company, camaraderie and commiseration during long hours in the Wubbold Room;

All the staff at SPRI, for making it such a pleasant workspace;

My friends and family, for their encouragement and support and for providing feedback on various drafts.

Table of Contents

IV. List of Figures and Tables

1. Introduction

The ice sheets of Greenland and Antarctica are among the largest potential contributors to isostatic sea-level rise (Shepherd and Wingham, 2007). The Greenland ice sheet (GrIS) alone contains enough freshwater to raise sea levels by ~7m if it were to melt completely (Wang et al., 2007; Bartholomew et al., 2010). Since the 1990s, temperatures over the GrIS have warmed by ~2°C as the negative relationship between the North Atlantic Oscillation (NAO) index and temperatures over Greenland has broken down (Hanna et al., 2008). Instead, temperatures over southern Greenland have exhibited a positive correlation with rising northern-hemisphere average temperatures (Hanna et al., 2008) – enough to increase the length of the ice sheet's melt season, the areal extent of summer ablation (Figure 1.1) and the amount of meltwater runoff from the ice sheet (Hanna et al., 2008; 2011). Further warming of 2-12°C over the course of the 21st century has been predicted (Gregory et al., 2004), significantly more than the global average as high-albedo sea ice is replaced by darker seawater for longer time periods each year (Serreze et al., 2007). Robinson et al. (2012) suggest that an average warming of 0.8-3.2°C over Greenland would be sufficient to cause the disappearance of the GrIS over the next 1000 years, and CO_2 levels are predicted to be high enough by 2100 to effect such a change.

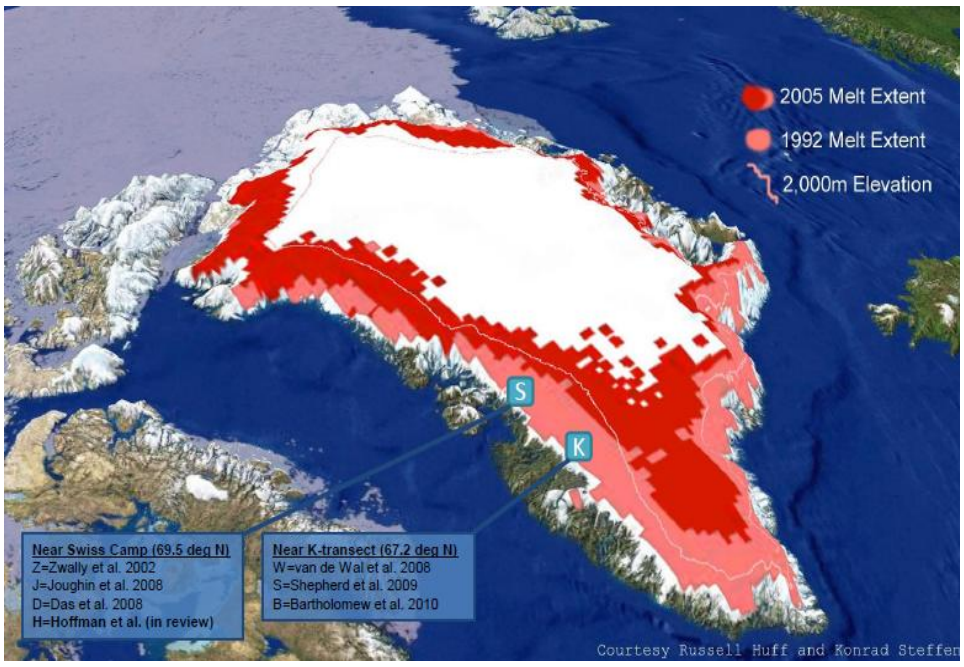

Figure 1.1: Melt extent on the GrIS in 1992 (bright red) and 2005 (dark red). The 2000m elevation contour is drawn in red. From Hoffman (2011), Courtesy of R. Huff and K. Steffen.

Recent GrIS mass-balance estimates suggest accelerating mass loss. Rignot et al. (2011) derive a total average mass loss of ~217 Gt yr^{-1} from satellite gravimetric data, which makes for average mass loss acceleration of 22 Gt yr^{-2} over the period 1999-2009. This is contrasted by an insignificantly negative mass balance of -22.1 km^3 yr^{-1} over the period 1958-2006 (Hanna et al., 2008). However, this accelerated mass loss in the 21st century is not distributed uniformly across the ice sheet. Dividing the ice sheet into six interior (>2000m above sea level (asl)) catchments and six marginal ones (<2000m asl), Luthcke et al. (2006) find that the interior of the ice sheet gained mass from 2003-5 while the marginal catchments, particularly the southeastern part of the ice sheet, lost mass at a higher rate.

Approximately 80% of current GrIS mass loss is offset, for now, by a shift in storm tracks and related cooling and increasing snowfall at elevations above ~2000m asl (Schuenemann and Cassano, 2010; Sorensen et al., 2011; Sundal et al., 2011). The future development of the GrIS is poorly constrained due to computational and theoretical limitations of global climate models and their forcings, but also due to a limited understanding of the causes of the changes occurring particularly in marginal areas of the GrIS.

Marginal areas of the GrIS can be grouped by their location: mass loss from marine-terminating and land-terminating catchments is thought to be driven by different factors. Tidewater glaciers have been observed to undergo episodes of dynamic thinning at unsustainably high rates. Jakobshavn Isbrae on the west coast of the GrIS doubled its velocity and thinned by up to 15m yr^{-1} from 1997-2005, with an influx of warm water into Jakobshavn Fjord causing rapid ice-tongue thinning and a drop in its buttressing effect (Holland et al., 2008). However, improved lubrication of the bed by increased surface melt and effective drainage may also have played a role (van de Wal et al., 2008; Sundal et al., 2011). Similarly, Kangerdlugssuaq and Helheim Glaciers in south-eastern Greenland, together draining over a third of the south-eastern GrIS by volume (Rignot and Kanagaratnam, 2006), experienced anomalous and unsustainable rates of mass loss 2003-2005, retreating up to 5km in a single winter (Howat et al., 2007). These sudden mass-loss

events followed a long period of ice thinning and acceleration near the grounding line and represented some 40% of the GrIS's total mass loss increase over those years (Howat et al., 2007).

Land-terminating areas of the GrIS are also experiencing mass loss, but this is driven by different mechanisms. They have been found to respond to changes in surface temperatures and resulting ablation and runoff very quickly, with variations on interannual (van de Wal et al., 2008), seasonal, diurnal (e.g. Shepherd et al., 2009) and even shorter (Das et al., 2008) timescales. This is inconsistent with the long-held view that most motion here occurs due to ice deformation near the bed (where stresses are greatest) – surface changes would take centuries or longer to propagate through ice several hundreds of m thick and response times would be far longer than those observed (Zwally et al., 2002). They suggest a mechanism for accelerated mass loss whereby increased melting lubricates the ice-sheet bed in summer, once a hydrological connection is established between surface and bed. In slow-flowing parts of the ice sheet, this could produce seasonal accelerations of up to 100% above long-term averages (van de Wal et al., 2008). Accelerated flow then moves more ice to lower elevations, further enhancing ablation rates. The basic notion of a relationship between melt rates, runoff and flow velocity and mass loss has attracted a great deal of interest over the last decade (e.g. Jobard and Dzikowski, 2006; Shepherd et al., 2009; Bartholomew et al., 2010; Hoffman et al., 2011; Sundal et al., 2011).

Since most of this projected mass loss will contribute to runoff from the ice sheet and to sea-level changes, it is of crucial importance to understand the meltwater-driven velocity forcing of land-terminating parts of the GrIS. Studies on the GrIS have mostly been undertaken using physically based modelling (Pimentel and Flowers, 2010; Schoof, 2010; Schoof and Hewitt, 2011; Sundal et al., 2011). However, the relationship between climate, runoff and flow velocity has also been studied on a variety of glaciers in the Himalayas (Singh et al., 2000), Alps (Gurnell et al., 1992; Willis et al., 2002; Jobard and Dzikowski, 2006), the Canadian Arctic (Moore and Demuth, 2001; Bingham et al., 2003) and Svalbard

(Hodson et al., 1998; Hodgkins, 2001), often using statistical techniques.

Accurate assessments of potential ice-sheet contributions to future sea-level rise are of particular relevance given that the collapse of former ice sheets has caused sea-level rises of as much as 20m in ~500 years in the last 15,000 years (Shepherd and Wingham, 2007). While the sudden collapse of the GrIS on such timescales is unlikely (Parizek and Alley, 2004), even a far slower and smaller contribution to rising sea levels would have considerable adverse impacts on human society (Stern, 2006). Such assessments must needs incorporate studies of the exact nature of runoff, resulting mass loss, and its interaction with climatic, oceanic and dynamic drivers in different areas.

2. Aims

This project aims to provide a new perspective on the temporal variability and evolution of the interaction between shortwave radiation, air temperature and runoff in the Paakitsoq region by investigating time series of these variables from 1997-2005. This will be achieved using a methodology that has been previously applied in hydrological studies of glacial and fluvial catchments, but not in an ice sheet context.

Discharge data from a lake which marks the confluence of the proglacial streams draining the Paakitsoq area of the GrIS is monitored by ASIAQ, a Greenlandic government institution, who run a hydrology project involving monitoring stations for water level (which can be converted to discharge) and other variables. There are several meteorological stations in the area, with JAR1, 2 and 3 and the Swiss Camp meteorological station, all maintained by the Greenland Climate Network (Steffen and Box, 2001), all situated within the Paakitsoq area itself. Data from JAR1 is continuous from 1997 to 2005 (with periods of missing data in 2000 and 2003) and will be used here.

Wavelet analysis of the time series forms the core of the project. Conceptually based on the Fourier transform, wavelet methods originate in signal processing and are frequently applied in time series analysis more generally (Nason, 2006) and in the geophysical and hydrological sciences specifically (Foufoula-Georgiou and Kumar, 1994; Lafrenière and Sharp, 2003; Melesse et al., 2009).

The specific objective of this dissertation is to examine the structure of variability in meteorological and hydrological time series within and between individual melt seasons using analysis in the frequency domain rather than the time domain. The focus is on short timescales, particularly the diurnal scale and up to 3 days in the univariate and 4 days in the multivariate analysis. This will be achieved using two methods:

a) The continuous wavelet transform (CWT) is applied to analyse interannual, seasonal,

diurnal and other variation in the time series in three dimensions – time, frequency and amplitude.

b) Multivariate analysis will be performed in order to study the co-variation between air temperature and discharge, and between net shortwave radiation and discharge, and how these relationships change over the course of the observation period. Wavelet coherence (WCO) and the phase difference between the series will be considered, as well as the average coherence of the two series over the entire period.

3. Literature Review

3.1 Drainage and Flow of the GrIS at Paakitsoq

The Paakitsoq area, being relatively low-elevation and with high seasonal melt and runoff, contributes a disproportionately large amount to total runoff from the GrIS (Box et al., 2006). Increasing mass loss occurs to a significant extent due to dynamic changes at tidewater glaciers resulting (at least partly) from oceanic causes (Rignot and Kanagaratnam, 2006; Howat et al., 2007; Holland et al., 2008), but land-terminating areas of the ice sheet have been the subject of growing interest particularly since Zwally et al. (2002) suggested a connection between melt, drainage of water to the bed and local flow velocities. This goes against the old consensus of slow-flowing, land-terminating parts of the GrIS moving primarily by ice deformation since the ice sheet is cold-based (Parizek and Alley, 2004). Were this the case, dynamic velocity responses to climatic change would occur with lag times of centuries and longer (Huybrechts et al., 2004). Findings of short-term flow variation as a result of increased surface melt and resulting basal sliding are therefore of particular importance. Such evidence suggests that runoff contributes to increased ice mass loss and accelerated sea-level changes not only directly by flowing into the sea, but also indirectly by affecting the flow speed of the ice sheet towards lower (warmer) elevations (Palmer et al., 2011). Satellite data have confirmed that the GrIS's margins respond to surface melt on various timescales (Joughin et al., 2010). This section provides a brief overview of observations and theory on intra- and interannual runoff evolution as well as the implications thereof on flow velocity.

Bamber et al. (2007) note three pathways through which ice sheets can respond to external forcings on short (annual/decadal) timescales. These include ice-shelves and their buttressing effect which can exert significant control over the flow velocity of glaciers lying behind them, and direct ice-sheet/ocean interactions which tend to deliver more energy into the ice sheet than the atmosphere. Finally, they note the possibility of meltwater

drainage to the bed of ice sheets, causing acceleration and vertical uplift.

3.1.1 Mass Balance, Melt and Runoff

Ablation contributes some 50% to mass loss from the GrIS, the other major factor being calving from tidewater glaciers (Parizek and Alley, 2004; Rignot and Kanagaratnam, 2006). Both of these are affected by increases in supraglacial meltwater availability, but through different mechanisms (van de Wal et al., 2008). In order to understand the impact of summer ablation on flow variation and the possibility of a resulting further indirect contribution to mass loss from land-terminating areas, an accurate quantification of melt and runoff is necessary. It is important to distinguish between the two as not all meltwater necessarily leaves the ice sheet as runoff: mass balance estimates must account for the possibility of meltwater retention in the ice via slow percolation and potential refreezing to form superimposed ice (Janssens and Huybrechts, 2000; Wang et al., 2007). These effects need to be considered in all areas other than the dry-snow region which lies upglacier of the -27°C isotherm where melt never occurs, and the wet-snow region where melt occurs but runoff does not because the snowpack never becomes saturated. The area studied here is lower than 1500m and therefore lies below the runoff line. It includes the slush zone, where the snowpack becomes saturated so that runoff occurs, and the area below the snowline where ice is exposed. Plots of average melt extent over the period 2000-4 in the summer/autumn months of May-October (Figure 3.1) show that Paakitsoq consistently experiences melt in these months. However, this does not necessarily translate into runoff because as temperatures drop the formation of superimposed ice becomes more likely (Wang et al., 2007). Such impermeable ice layers in the snowpack can also change runoff pathways and affect the time lag between melt and discharge, complicating the interpretation of discharge variability.

The Kangerlussuaq Transect (K-transect), situated 2 degrees latitude south from Ilulissat, has one of the longest observational records of mass balance and shows a statistically significant increase in mass loss, but also high interannual variability. The ablation rate

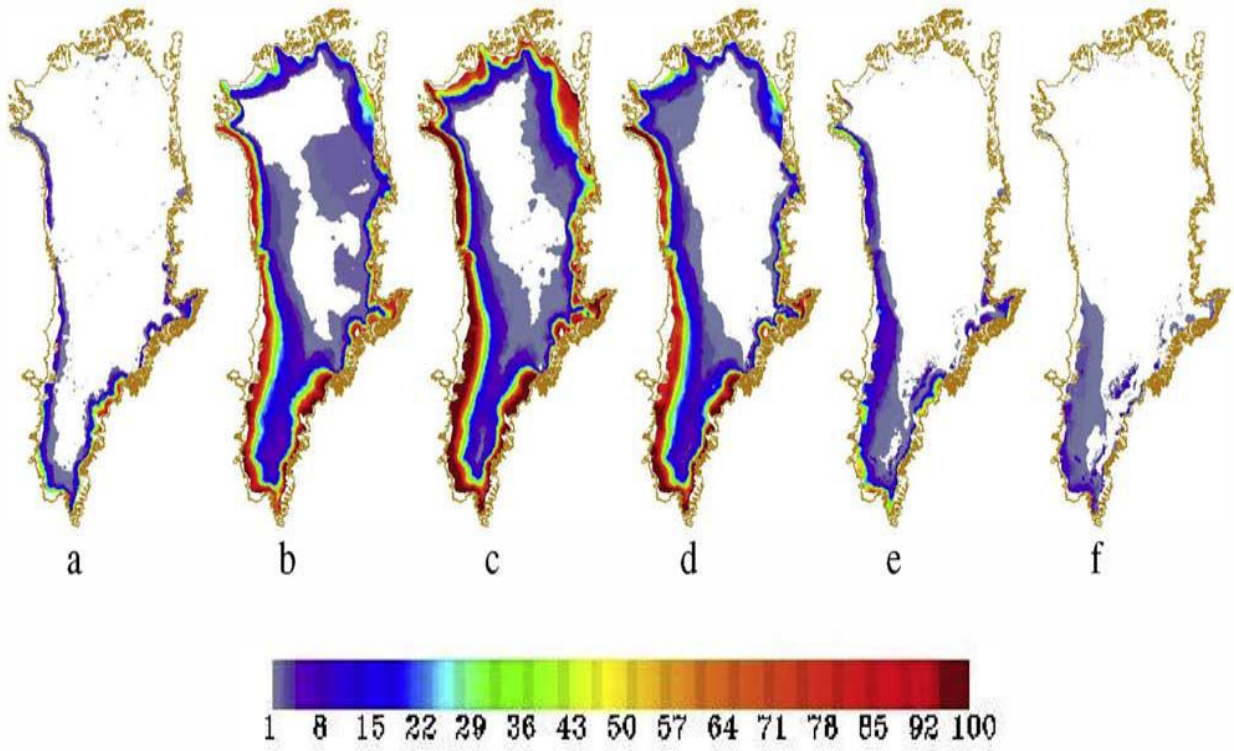

Figure 3.1: Illustration of average (2000-2004) melt quantities in the months of May-October (a-f).White signifies no melt. Note the central western margin where the Paakitsoq region is located, which is consistently non-white. Source: Wang et al. (2007)

varies between 2.8 and 5.6m a^{-1}, although the ice margin has stayed roughly constant since 1985 (van de Wal et al., 2008). This increase in mass loss is temporally coincident with a similarly significant increase in air temperatures as measured by coastal weather stations in southwest Greenland – but these conclusions are also applicable to the low-lying ablation areas of the GrIS (Hanna et al., 2008). They find that runoff has increased by 40% across the GrIS, and tends to correlate well with the area affected by snowmelt in any given year. It is worth noting, however, that the proximity of the Paakitsoq area to Jakobshavn Isbrae to the south (Figure 4.2), one of Greenland's largest glaciers which has recently experienced rapid retreat (Motyka et al., 2011), has led to suggestions that the glacier's extended retreat may influence or even partly cause the thinning rates and mass loss observed near Swiss Camp (Krabill et al., 2004; Mottram et al., 2009).

While the increase in melt that causes the changes in runoff outlined above is largely offset by increases in precipitation (particularly over western Greenland; Hanna et al., 2008; Schuenemann and Cassano, 2010), the possibility of meltwater indirectly affecting the GrIS's mass balance has received growing attention over the last decade.

3.1.2 Connections between Meltwater Availability and Flow Velocity

Surface meltwater affects ice-sheet flow dynamics via the bed where, if surficial water can access it, basal sliding can occur even if the pressure melting point is not reached and the ice sheet is therefore cold-based. Such an unusually direct link between surface hydrology (which is controlled by climate) and basal hydrology (which controls fast flow) would provide a very direct way for climatic changes to influence flow behaviour of marginal parts of the GrIS (Christoffersen and Hambrey, 2006).

Links between surface melt and flow velocity have been observed in a variety of settings. Gurnell et al. (1992) note a temporal relationship between climatic inputs (temperature, radiation, wind speed and direction, humidity and precipitation) and proglacial discharge at Haut Glacier d'Arolla (HGdA), Switzerland. They find that the glacier's drainage system evolves supraglacially, but also within and beneath the ice over summer. This affects the manner in which diurnal climatic inputs translate into discharge with changing lags and diurnal amplitudes. Lags between peak temperature/radiation and runoff decrease over the course of summer to a minimum of 2-3 hours (Gurnell et al., 1992).

Similarly, discharge variations are controlled by snow-/icemelt and the evolution of the drainage system throughout the glacier at Baounet Glacier, France (Jobard and Dzikowski, 2006). They identify distinct stages of runoff evolution, starting with a period of low, stable discharge with little variation which is followed by increasing diurnal amplitudes and decreasing lags between peak temperature and discharge. This regime persists for a while, probably due to a lack of snow cover which means supraglacial runoff becomes more consistent, until meltwater inputs fall again and diurnal amplitudes decrease (Jobard and Dzikowski, 2006). This is similar to the findings of Gurnell et al. (1992) and Richards et al. (1996) at HgDA, another temperate glacier at a similar latitude.

Glaciers at higher latitudes have exhibited similar behaviour. Moore and Demuth (2001) note that summer discharge is determined primarily by winter snow accumulation and summer temperatures at Place Glacier, Canada. Similarly, Gulkana and Black Rapids

Glaciers in Alaska recorded unusually low flow speeds during the record-breaking heatwave of summer 2004 which produced very high quantities of runoff (Truffer et al., 2005). This suggests that the relationship between meltwater input into a glacier and its flow velocity is not linear, although transient speedups are noted: the relationship is thus likely to be complex (Truffer et al., 2005).

Bartholomaus et al. (2008) similarly attest that meteorological variables alone are insufficient for modelling basal motion satisfactorily. At land-terminating Kennicott Glacier, Alaska, they find that the evolution of the subglacial drainage system plays a central role in determining flow speed response to meltwater inputs as this determines the percentage of the bed accessible to pressurised water. The drainage system undergoes significant change after the drainage of a supraglacial lake which produces a spike in water inputs and brings about a change in drainage and flow regimes alike. Pre-lake drainage, diurnal variations in horizontal flow and vertical uplift occur, with proglacial discharge having low electrical conductivity indicating low residence time. This is because high pressure means that part of the meltwater moves through the glacier quickly, while the remainder enters storage in the inefficient, and possibly unconnected, distributed drainage system (Bartholomaus et al., 2008). After the lake drainage, they note that the drainage system has grown and changed enough to transmit all incoming meltwater, and stored water will gradually be released and register high electrical conductivity due to its long residence time in the glacier. Bartholomaus et al. (2008) conclude that it is not water inputs that determine flow velocity, but the switch from net water storage to net water release brings about the switch from diurnal variation to the absence thereof. The causal link to drainage system evolution remains, however.

John Evans Glacier in Arctic Canada is an entirely cold-based glacier which has been studied as a relatively close analogue of the GrIS. Boon and Sharp (2003) observe the opening of a crevasse and its gradual filling with meltwater over 12 days. These days saw only slow gradual drainage and are associated with crevasse propagation towards the bed. Once the resulting pond had drained completely over a short period of time, several new crevasses

were found, all aligned perpendicular to the direction of the stream feeding the lake. Boon and Sharp (2003) suggest that initial connections to the bed might have refrozen due to their small size and very cold englacial ice (~-15C); continued fracturing would have been required to establish a larger-scale connection with the bed, where meltwater may have encountered further resistance from an inefficient winter drainage system (Bingham et al., 2003). While temperate glaciers may allow for faster hydrofracturing and drainage, completely cold glaciers apparently require greater inputs and longer time for the development of efficient surface-bed drainage systems.

On the GrIS itself, Zwally et al. (2002) were the first to note large seasonal fluctuations in flow velocity in the Paakitsoq area. They find that velocities peak between late July and early August, with a rapid drop to minimum velocities in late August/early September and a slow, gradual return to slightly higher winter averages. This velocity pattern exhibits very high levels of correlation (R^2=0.96) with cumulative positive degree days (PDDs), which also determine the area of the ice sheet that experiences melting; the timings of melt cessation and the transition from acceleration to deceleration also tend to coincide. Zwally et al. (2002) conclude that the interaction between temperatures, ablation, flow to the bed and resulting basal sliding despite a cold bed is a mechanism for rapid ice-sheet response to climatic change which could lead to a feedback loop.

Hoffman et al. (2011) identify several scales of velocity changes caused by meltwater supply to the bed. The seasonal (summer) speedup is apparent from 24-hour velocity averages and beginns roughly a month following the onset of PDDs. Diurnal changes tend to be more localised and depend on peak daily temperatures, while sudden, one-off acceleration events tend to register only at individual stations and have a small overall impact on total flow (Hoffman et al., 2011). Using InSAR, Joughin et al. (2008) find that in the Swiss Camp area, seasonal speedup of up to 36m a^{-1} can occur. This is an increase of 50% over winter averages and is correlated with melt rates which can exceed 2m a^{-1}.

At the K-transect just south of the Paakitsoq region, flow velocity follows the onset of

melting with some lag, rising gradually but with significant shorter-term variations of up to 30% over weekly timescales (van de Wal et al., 2008). The response of velocity to melt rates is found to be strongest and fastest near areas with many moulins/crevasses, suggesting a causal link between the two variables. However, van de Wal et al. (2008) do not confirm the long-term feedback loop suggested by Zwally et al. (2002): short-term correlations between flow speed and meltwater supply exist, but they find that the hydrological system adapts to the higher meltwater fluxes over time so that the feedback loop breaks down (van de Wal et al., 2008; Bartholomew et al., 2010).

This coupling between surface melt and ice dynamics occurs due to the production of high basal water pressures once surface water accesses the bed via crevasses and moulins, which can be temporary or persist over many years (Catania and Neumann, 2010; Palmer et al., 2011). Palmer et al. (2011) identify good correspondence between patterns of seasonal acceleration in a given catchment and the volume of meltwater accumulated there; within a catchment, the greatest acceleration was found near supraglacial sinks or streams, as shown in Figure 3.2 for the Paakitsoq catchment. Acceleration is thus far from consistent spatially and exhibits a number of gradients: velocity increases over summer averages tend to decrease upglacier, particularly beyond the equilibrium line (Figure 3.3; van de Wal et al., 2008; Shepherd et al., 2009), and towards topographic sinks (although not all topographic lows exhibit acceleration). Indeed, some areas do not accelerate at all (Palmer et al., 2011).

It is worth noting that the seasonal speedup resulting from basal lubrication is observable not only in slow-moving parts of the ice sheet but also on outlet glaciers terminating both on land and in the sea. Bartholomew et al. (2011) identify clear temporal patterns in the relationship between air temperature and discharge from Leverett Glacier on the western part of the GrIS. Runoff is found to start up slowly, lagging above-zero temperatures by days, before increasing rapidly and growing episodically to an overall maximum of 317 $m^3 s^{-1}$, with gradual growth defined by diurnal cycles whose amplitude increased with time, and by four large, single-day pulses. The early-summer meltwater “pulses” are also

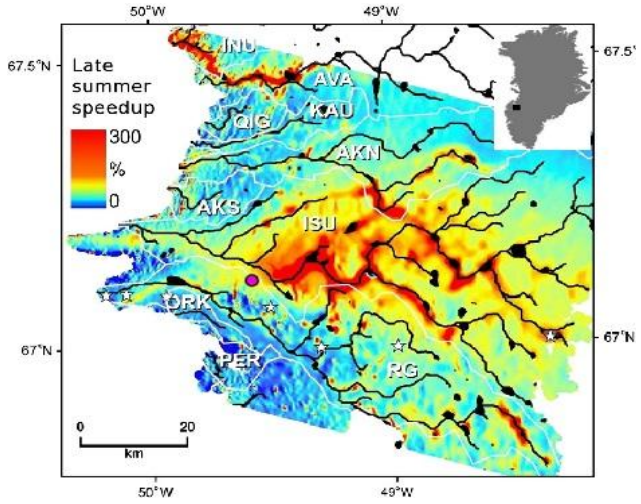

Figure 3.3: Supraglacial catchments (white lines) near the K-transect (white stars). Late-summer velocity changes relative to winter averages are shown (colour scale) along with meltwater streams and topographic sinks (black lines/spots, respectively). Location in Greenland shown in the inset.Source: Palmer et al. (2011)

apparent in records of electrical conductivity (EC) and suspended sediment content, which implies variation in residence time of water in the hydrological system. This pattern is known from valley glaciers, where lower EC suggests that water was transported along the bed rapidly so that fewer solutes dissolved into it (Bartholomew et al., 2011).

Observations from Russell Glacier, just to the north of Leverett Glacier, suggest that velocities peak at up to 70-100% above winter average flow rates (Bartholomew et al., 2010). The air temperature and discharge developments noted drive changes in the hydraulic efficiency of the subglacial drainage system, which is found to be the main control on the exact relationship between meltwater inputs and the resulting dynamic change. In late summer, once earlier meltwater has created a more efficient system, very large throughputs are required to produce a velocity response, explaining why a gradual slowdown to winter flow rates is punctuated by short peaks which correspond to extreme meltwater events (Bartholomew et al., 2010). Shepherd et al. (2009) note that the local coincidence of meltwater input and the velocity changes and vertical uplift detected at Russell Glacier are indicative of hydraulic jacking of the glacier as meltwater inputs drain via the subglacial hydrological system. The relatively short lags of ~2h imply that the transport mechanism through the ice to the bed must also be efficient, at least in late summer.

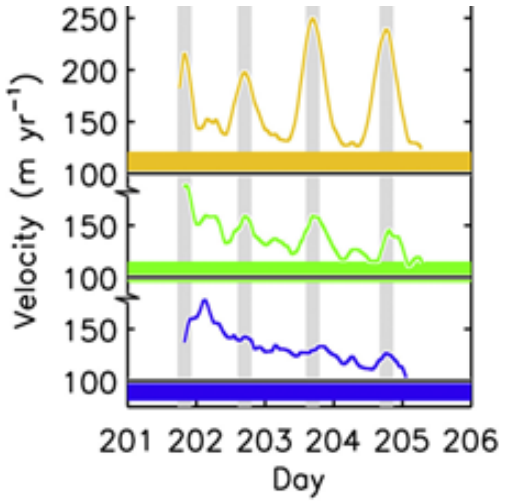

Figure 3.2: Flow velocity variations at various distances from the ice margin on Russell Glacier: 37km (yellow), 53km (green) and 72km (blue). The respective winter flow speeds are indicated by the bold lines. Source: Shepherd et al. (2009)

3.1.3 Supraglacial Lakes and Drainage Events

Sundal et al. (2011) note that the summer acceleration events noted on land-terminating parts of the GrIS tend to occur further upglacier as the melt season progresses, roughly following the timing of the onset of surface melt at a given elevation. This implies that a warming climate might allow local acceleration due to hydraulic jacking to occur further upglacier in the future – but there is a possibility that this is already the case due to longitudinal coupling of upglacier and downglacier ice. Price et al. (2008) suggest that while summer acceleration near the ice-sheet margins results from local basal lubrication, this may not be the case further upglacier, although the distances over which such a connection might occur are unclear.

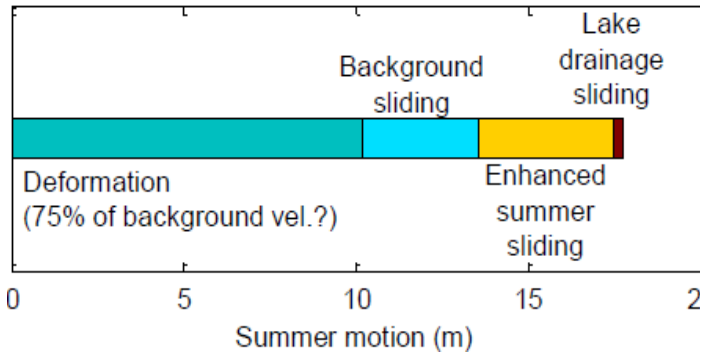

Figure 3.4: Approximate breakdown of components of average summer flow velocity. Dark and light blue represent winter background deformation and sliding rates, respectively; yellow represents enhanced summer sliding and red sliding from lake drainage events.. Source: Hoffman et al. (2011)

The aforementioned peaks in meltwater input, which can cause velocity increases even in late summer when the drainage system is presumed to be effective, are likely to be due to the accumulation of meltwater at the ice surface before draining „en masse“. Das et al. (2008) describe the drainage of one such supraglacial lake near Swiss Camp over the course of just hours. They note that lakes can play an important role in crevasse propagation to the ice-sheet bed by supplying the weight and water required to stop the crack from refreezing (up to >50 million m^3; Box and Ski, 2007). Once a connection to the bed is established, a moulin forms and other cracks which may have formed in the process gradually close as meltwater flows down the moulin. The daily resupply with meltwater prevents the moulin's closure. Warming temperatures could lead to the earlier formation of lakes and a more widespread distribution, affecting overall flow velocity. It is worth noting, however, that flow velocity changes due to lake drainage events currently contribute only minimally to the overall flow of the GrIS (Figure 3.4).

Of the lakes observed on the GrIS over the 2005-9 period using MODIS imagery, 55%, and 59% of total lake area, were located in the southwestern part of the ice sheet (Selmes et al., 2011). Lakes are unusually frequent here relative to the length of ice-sheet margin (relevant as they occur in a band near the margin), and they also experience fast drainage more often (61%) than in most other areas. Despite the strong indication that lake drainage events produce strong local acceleration, the region with greatest overall mass loss (southeast) has the fewest lakes and fast drainages, suggesting that the dynamic thinning of tidewater glaciers in this region is unrelated to supraglacial lakes but to oceanic effects and possibly bed topography (Sundal et al., 2011).

Hoffman et al. (2011) note that the direct effects of lake drainages on actual flow velocity tend to be short and local, spreading out like a blastwave from the moulin where they occur for a short distance. Their other major contribution is their ability to alter the englacial and subglacial hydrological systems, altering the way in which surface meltwater accesses the bed and drains towards the terminus.

In general, the hydrological system of a glacier is shaped by persistent water inputs which increase the throughput capacity of the system, and creep closure, a function of overburden pressure, which lessens its capacity. Meltwater inputs are absent during the winter so that each melt season, the ice sheet's drainage system tends to start out as an inefficient cavity system (Bartholomew et al., 2010; Schoof, 2010; Sundal et al., 2011).

3.1.4 Surface Meltwater Routing Through and Under the Ice

Surface meltwater reaches the bed via moulins, which route water through the ice rapidly via shafts and plunge pools (Benn et al., 2009), or crevasses, in which case englacial routing is more tortuous and takes significantly longer. For a crevasse to reach the bed, it is necessary that water levels in the crevasse be no more 15m below the ice surface, and that tensile stresses be >150 kPa (van der Ween et al., 1998). This hydrofracturing process, i.e. hydrologically driven fracture propagation, is known from Himalayan and Arctic glaciers

with different thermal regimes (Benn et al., 2009), but also from high Arctic glaciers (Bingham et al., 2003). The stress intensity factor, which needs to overstep a critical value for crevasse formation and propagation to occur, is a function of tensile stresses in the ice as well as water pressure (if the crevasse is water-filled; van der Ween et al., 1998). Water can also slowly percolate through ice at its PMP, although this is a slow process and refreezing may occur within the ice, producing superimposed ice (Bartholomew et al., 2011; Hoffman et al., 2011). The time lag between the onset of surface melt and seasonally increased basal flow can vary from days to weeks (Benn et al., 2009; Hoffman et al., 2011) and reflects this variety of englacial pathways.

Once at the bed, supraglacial water can significantly impact on the drainage system underlying the GrIS. Winter drainage systems tend to consist of cavities which form as sliding ice separates from the bed on the lee side of obstacles (cavitation; Figure 3.5b) – these may be autonomous or interconnected via a dendritic channel network (Walder,

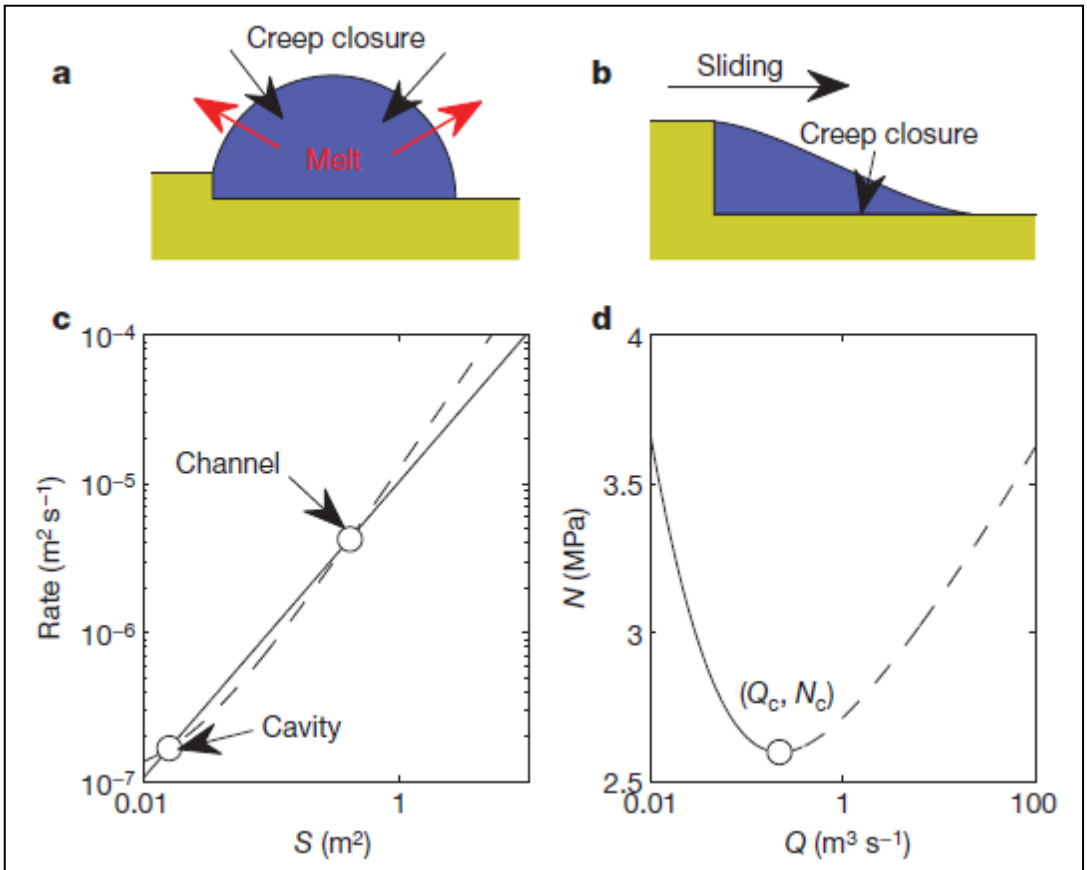

Figure 3.5: Subglacial hydrological systems (schematic). a) Röthlisberger channels (incised into the ice, rather than the bed); b) Cavities; c) rate of conduit opening (dashed line) and closure (solid line); d) net effective pressure N vs discharge Q. The switch to a channelised system occurs at (Q_c, N_c). Source: Schoof (2010)

1986). In winter, when there is no surface melt, creep closure and cavitation and frictional melting will balance, producing an inefficient steady-state system that can cope with the small quantities of water that flow along the bed during this period. Since even small increases in water input will cause a large increase in water pressure and acceleration (Bartholomew et al., 2010), the onset of melt in summer can produce rapid acceleration: as net effective pressure (ice overburden – water pressure) drops, basal sliding occurs.

As long as an inefficient drainage system persists beneath an area of the ice sheet, the positive feedback between surface melt, runoff and basal sliding is maintained as outlined by Zwally et al. (2002). However, sustained inputs of high quantities of meltwater can bring about a switch to a more efficient, channelised drainage system in which any given meltwater quantity is transported at significantly lower pressure (Schoof, 2010; Figure 3.5a). Indeed, the hydraulics of a channelised hydrological system fundamentally differ from a cavity-based system – flow localisation into fewer, larger channels and a rising volume-surface area ratio mean that increasing discharge actually lowers pressure as the channel becomes larger (Walder, 1986). Schoof (2010) highlights the point at which the switch to an efficient drainage system will occur – the point at which the conduit opening rate exceeds the closing rate (Figure 3.5c) and at which net effective pressure is at a minimum (Figure 3.5d). This could translate into a critical melt rate (Sundal et al., 2011). Since a channelised system forms once a certain level of net effective pressure and discharge is reached, the resulting channelised system will qualitatively be the same whether discharge increases suddenly or gradually at the onset of melt. This may explain the earlier peak in flow speed in high-melt years – but also why these peaks are shorter, and followed by much lower velocities (Sundal et al., 2011). High-melt years see an average summer acceleration of 39% over winter averages, while low-melt years see 102% acceleration in their study area in west Greenland. Sundal et al. (2011) conclude that the duration of the fast-flow period (2x winter averages), is inversely proportional to melt intensity.

3.2 Time-Series Analysis and the Fourier Transform

Time series are most commonly represented in the time domain: their graphs are usually in time-magnitude space, showing the magnitude of the signal at any point in time. In many cases, however, this does not convey all the information contained in a function effectively, particularly if the exact nature of the variation of a time series is of interest. The frequency domain contains useful information about a function that may not be apparent from the time-domain representation. This may include information about periodicity or regularity at certain frequencies which can be useful when interpreting the causes and effects of anomalies and changes over time. (Mohlenkamp and Pereyra, 2008)

The discrete Fourier transform is a basic mathematical operation that represents a square integrable, continuous function of time t [i.e. f(t)] over the interval [0,1) as a function of frequency; that is, it produces a representation of f(t) in the frequency domain by decomposing the function into components of only standard trigonometric functions (sine and cosine; Ogden, 1997). It does so using the following formula (after Mohlenkamp and Pereyra, 2008), where f(n)=a_n is the frequency-amplitude representation of a function f(t):

$$a_n = f(n) \coloneqq \int_0^1 f(t) e^{-2\pi \mathrm{int}} dt \qquad \text{where n is a complex number.} \qquad (1)$$

It is worth noting that the complex exponential (-2πint) is never zero for any value n, meaning that when calculating the integral, all values of the function are considered at each given frequency. That is, a small change in any part of the signal will affect Fourier coefficients across the entire signal (Mohlenkamp and Pereyra, 2008); this implies that there is no temporal resolution inherent in the Fourier transform: it is well-localised in frequency but global, i.e. not resolved at all in time.

The discrete Fourier transform can be modified to become the continuous Fourier transform by periodically extending f(t) from the interval [0,1) to [a,b) and letting a → -∞ and b → ∞. The integral will have to be calculated for the interval (-∞,∞) in this case, but

the effective methodology is the same as with the discrete Fourier transform.

It would be desirable to obtain a perfect representation of the time-frequency content of a signal, but this is not possible using the Fourier transform as demonstrated by Heisenberg's uncertainty principle. Given a function f(t) and its continuous Fourier transform f(ξ), the time and frequency averages are then denoted by

$$x = \frac{1}{\| f(x) \|^2} \int x \mid f(x) \mid^2 dx \tag{2}$$

and

$$\zeta = \frac{1}{\| f(\zeta) \|^2} \int \zeta \mid f(\zeta) \mid^2 d\zeta \tag{3}$$

respectively, with the variances then being given by

$$\Delta_x = \frac{1}{\| f(x) \|} \sqrt{\int (x - \bar{x})^2 \mid f(x) \mid^2 dx} \tag{4}$$

and

$$\Delta_\zeta = \frac{1}{\| f(\zeta) \|} \sqrt{\int (\zeta - \bar{\zeta})^2 \mid f(\zeta) \mid^2 d\zeta} \tag{5}$$

(Carmona et al., 1998).

The Heisenberg uncertainty principle then states that

$$\Delta_\zeta \Delta_x \geq \frac{1}{2} \tag{6}$$

This implies that it is impossible to achieve perfect localisation in both time and frequency, and that there is effectively a tradeoff between the two.

A major shortcoming of the Fourier transform, then, is that its perfect frequency localisation means that all temporal resolution is lost. It basically gives information on the average frequency content over the entire duration of the signal, whereas it may often be

desirable to retain information on when certain frequencies occur in the signal. For example, the function

$$f(t) = \cos(20\pi t) + \cos(50\pi t) + \cos(100\pi t) + \cos(200\pi t) \quad (7)$$

which is shown in Figure 3.6a, has a constant frequency content over time which is shown in its Fourier transform (Figure 3.6c). The function shown in figure 3.6b, however, has a very similar Fourier transform despite being completely different: the same frequencies are present in the function, but each occurs on its own at a separate time rather than all frequencies being present throughout the function. This information is lost in the transformation (Carmona et al., 1998).

The Short-Term Fourier Transform (STFT) is an alternative to the discrete and continuous Fourier transforms which achieves time localisation to an extent and is therefore more useful when dealing with nonstationary functions, i.e. ones whose frequency content varies over time (Polikar, 1996). It uses a window function of a certain width ω (in time), usually a real function g(t) with a concentration of energy in low frequencies, which is shifted along the function to be transformed (Kumar and Foufoula-Georgiou, 1994). The Fourier transform Gf(ω,n) is then calculated individually for each interval:

$$Gf(\omega, n) = \int_{-\infty}^{\infty} f(t) g(n-t) e^{in\omega t} dt \quad (8)$$

(after Kumar and Foufoula-Georgiou, 1994).

While the STFT thus alleviates the problem of all temporal resolution being lost, it is still subject to the Heisenberg uncertainty principle: a narrower window will improve temporal resolution, but at the same time frequency resolution becomes poorer as a smaller section of the signal to be analysed is considered in each step. The logic behind this fact is that the size (or circumference) of the window remains constant (and depends on the particular window function) in two-dimensional time-frequency space. That is, a narrower – and more accurate – window size in the time domain leads to a wider, and less accurate, window in the frequency domain (Ogden, 1997). To illustrate, see Figure 3.7 which shows

the STFT of a function similar to that in Figure 3.6b using a window function of the form

$$g(t) = e^{-a\frac{t^2}{2}} \tag{9}$$

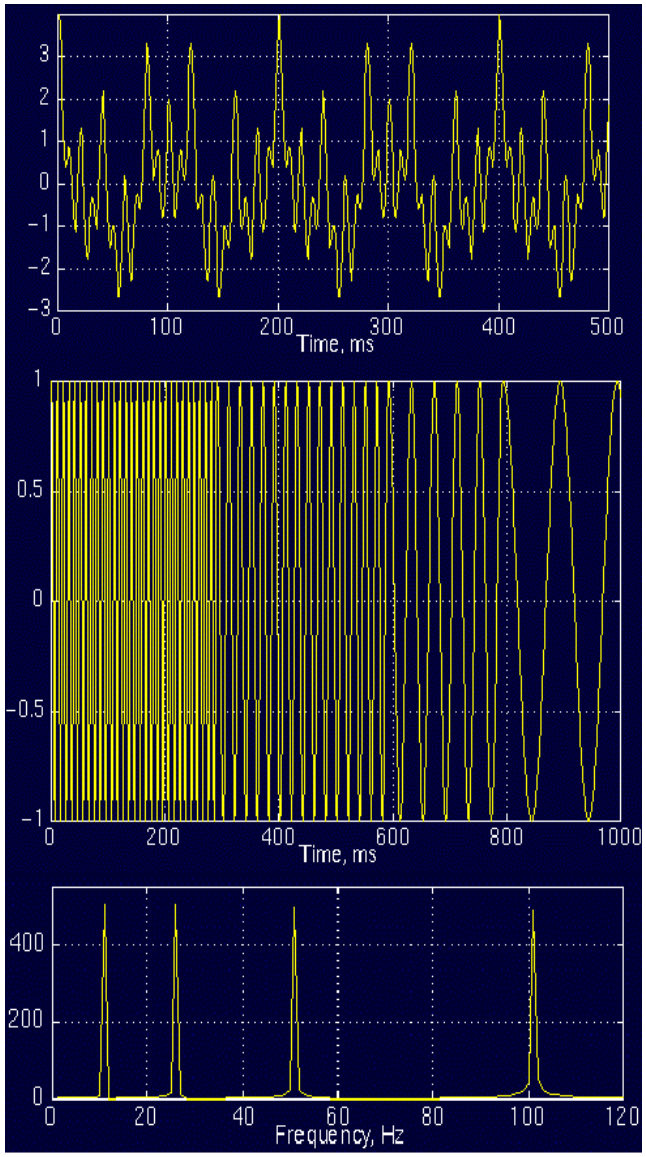

Figure 3.6: a) The graph of (7) (top); b) a different function with the same frequency content as (7) but at different times (middle); c) The Fourier transform of the two functions (approximate FT of b)). Source: Polikar (1996)

where *a* determines the width of the window in the time domain. Figure 3.7 shows the STFT in three-dimensional space, with time on the x-, frequency on the y- and amplitude on the z-axis. That is, it is possible to see the frequency content of a function *and* how it changes over time, which is impossible when using the normal Fourier transform. Figure 3.7 also shows the problem posed by Heisenberg's principle: the most accurate time resolution (top frame) is coupled with the poorest frequency resolution (bottom frame). Indeed, in the bottom frame time resolution is so poor that it is all but impossible to tell when one frequency stops occurring in the function and when another begins (as in Figure 3.6b). This problematic time-frequency localisation in the STFT means that if a signal has important features at various frequencies, then it is not possible to find a single optimal window for analysing the process with respect to all these features (Kumar and Foufoula-Georgiou, 1994).

3.3 An alternative to Fourier: the Wavelet Transform

Time series of natural phenomena have often been observed to exhibit an inverse relationship between the duration of an event and its frequency (Mohlenkamp and Pereyra, 2008). That is, low-frequency segments may well be present throughout the signal but may be punctuated by brief, high-frequency events. It therefore makes sense to analyse such time series using a elements that have similar properties – i.e. an inverse relationship between duration and frequency. Wavelets are one such function, providing high temporal resolution for high frequencies and low temporal resolution (but good frequency resolution) for low frequencies in the signal (Mohlenkamp and Pereyra, 2008). That is, low frequencies tend to correspond to a synoptic, non-detailed view of the signal while high frequencies contain detailed information on features of the signal which may only last a short time.

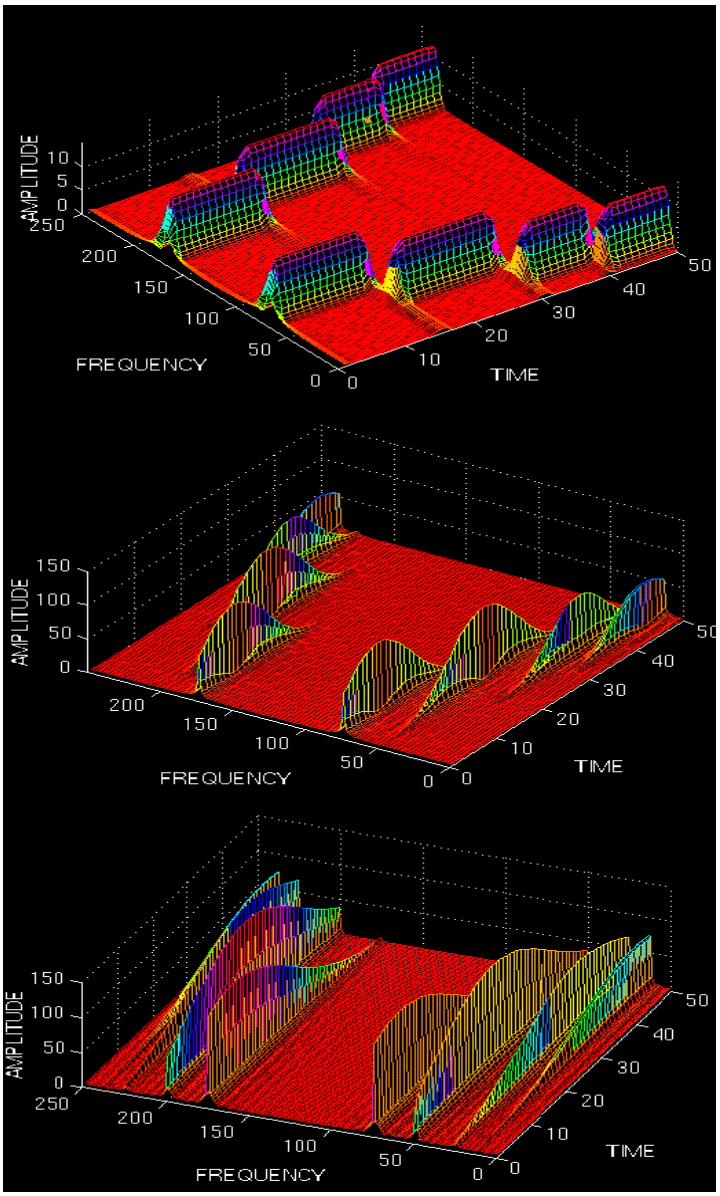

Figure 3.7: STFT of a function similar to that in Fig. 2b using (9) as a window function. Top: a = 0.001; Middle: a = 0.0001; Bottom: a = 0.00001. Source: Polikar (1996)

The wavelet transform is thus an improvement over Fourier methods, including the STFT, because it can achieve time-frequency localisation at all timescales (Mohlenkamp and Pereyra, 2008). Originating in signal and image processing, the continuous wavelet transform (CWT) was introduced into statistics in the 1980s and 1990s (Grossman

and Morlet, 1984; Daubechies, 1994). Wavelet methods have since become widely used for the analysis of time series (Nason, 2006). Instead of a window function, the CWT employs a wavelet function to generate a basis by which the signal to be analysed is multiplied. A wavelet function is oscillatory and tends to be short in order to ensure good resolution in both time and frequency (Polikar, 1996). The CWT is therefore similar to the STFT in that a function is shifted along the signal and short segments are analysed separately, but there are some crucial differences:

- The CWT does not apply the Fourier transform to the "windowed" signal, meaning that a single peak in the signal will correspond to a sinusoid – both positive and negative parts – in the CWT graph.
- A different window size is used for every spectral component, i.e. frequency band. This is what allows the CWT to retain its temporal resolution at all frequencies as low frequencies tend to require wider time windows and high frequencies narrower ones for optimum representation (Polikar, 1996). Figure 3.8 illustrates this differentiation between frequencies (on the y axis), with the lowest frequencies (highest levels) requiring less temporal resolution than higher frequencies (lowest levels). In an analogy to the STFT, this means that the size of the window function changes according to the frequencies under consideration (Lang and Forinash, 1998).

A wavelet function ψ(t) is derived from a mother wavelet Ψ(t), so-called because it can serve as a prototype from which many different wavelet functions with different regions of support (i.e. regions where the function is nonzero) are derived. The two main parameters

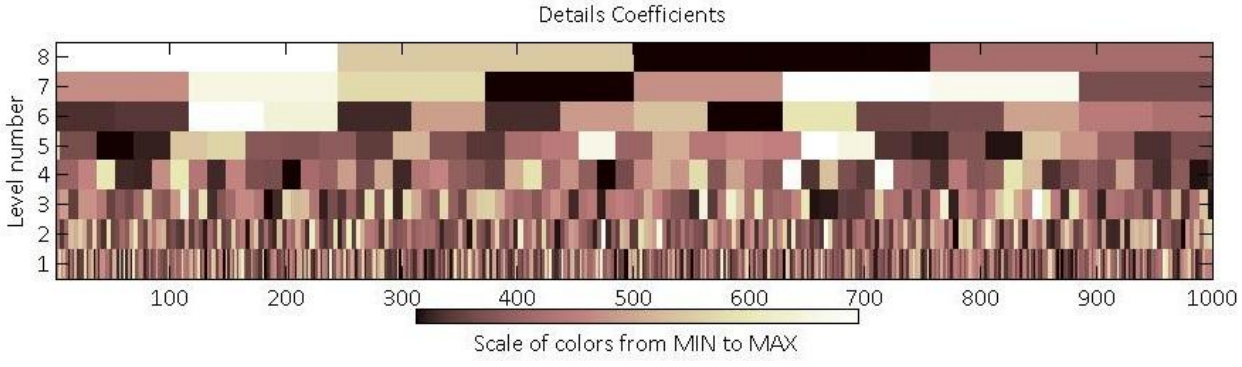

Figure 3.8: Wavelet Transform of a time series, highlighting the differentiation between spectral components.

defining a wavelet function are its translation τ>0 and scale s>0. Translation refers to the position of the region of support, which is shifted along the signal as its wavelet transform is calculated. This is the equivalent of the window function in the STFT being shifted along the signal and is relevant for the representation of time information in the frequency domain (Polikar, 1996). Scale is the equivalent of frequency in the STFT and is given by

$$s = \frac{1}{frequency} \tag{10}$$

so that a large-scale feature of a signal is one that occurs at a low frequency, such as the highest levels in Figure 3.8. The rationale behind wavelet methods providing accurate time and poor frequency resolution at small scales, and accurate frequency and poor time resolution at large scales is simple: small scales are likely to be localised in time and require high resolution in this dimension, while large-scale features are likely to persist throughout the signal, making it more important to resolve their frequency (Polikar, 1996). A wavelet function is effectively a band-pass filter (as opposed to a low- or high-pass filter), with a family of such functions, defined from the mother wavelet via varying translations and scales, able to cover all required scales (Hudgins et al., 1993).

Mohlenkamp and Pereyra (2008) derive the final wavelet function $\psi_{s,\tau}(t)$ using s and τ, as follows:

$$\psi_{s,\tau}(t) := \frac{1}{\sqrt{s}} \Psi\left(\frac{t-\tau}{s}\right) \tag{11}$$

such that $\psi_{s,\tau}(t)$ has an average of zero and a norm of one. Note the use of s in the denominator implying that larger scales dilate signals (unlike higher frequencies, which correspond to more compressed sequences) (Polikar, 1996). The CWT (Wf), then, is given by

$$Wf(s,\tau) = \int f(t)\psi_{s,\tau}(t)dt \tag{12}$$

showing that it, in effect, measures the powervariation of f(t) near time τ and at scale s.

One important drawback of the CWT is the large quantity of data it produces, and the

associated redundancy. In extreme cases, this can mean that the CWT's discrete counterpart, the discrete wavelet transform, or other, more specialised methods such as the dual-tree discrete wavelet transform (e.g. Kingsbury, 2005) become more efficient. However, for the purposes of this project data quantities – both the time series used as inputs and the CWT's outputs – are small enough that the CWT, which is also generally considered the best tool for feature extraction (Grinsted et al., 2004), is the most efficient tool (N.G. Kingsbury, personal communication).

3.4 Examples of Wavelets in Geophysics

The CWT in particular has frequently been applied to a variety of geophysical time series to investigate their variability on different timescales. Lafrenière and Sharp (2003) compare inter- and intraannual runoff variability in a nival and a glacial catchment in Alberta, Canada. They find that both are controlled to an extent by winter snowfall and summer meteorological conditions, as well as by long-distance oscillations such as the Pacific Decadal and the North Atlantic Oscillations. They note the importance advantage of wavelet analysis over traditional methods such as regression and Fourier analysis of being able to decompose data in three dimensions rather than two (time, frequency and amplitude), which is important because the relationship between meteorological factors and runoff changes over time. One crucial finding is that while shortwave radiation is the main energy source for icemelt in the glacial catchment, air temperature correlates more closely with melt and is a better proxy (Lafrenière and Sharp, 2003). Nival catchments are found to respond more quickly to temperature changes than glacial streams, which exhibit a phase difference of 4-6h on the 24h scale. Water storage and transfer times change over the seasons within both systems, with snowpack melting a particularly relevant source of gradual change in the phase difference between temperature and runoff in the glacial catchment (Janssens and Huybrechts, 2000; Hodgkins, 2001; Wang et al., 2007). Once the snowpack is gone, the exposure of low-albedo ice raises melt rates and an important storage reservoir is gone so that the system becomes more responsive to these meltwater inputs in late summer (Lafrenière and Sharp, 2003).

The Blue Nile River, which contributes over half of the Nile's flow volume, was investigated using wavelet analysis by Melesse et al. (2009). Analysing several decades of monthly runoff (Figure 3.9) and rainfall (Figure 3.10) data, Melesse et al. (2009) identify dominant frequencies of ~35 and ~65 months in both rainfall and runoff – this corresponds roughly to the timescale on which weather systems have a significant impact. Across the entire dataset, the seasonal trend between the wet and dry season is also highlighted. Similar trends are observed in monthly runoff, although with some lag behind rainfall.

Wavelet analysis is applied to daily and half-hourly local rainfall and runoff data from karstic springs in France by Labat et al. (2000), who find that such analysis performs significantly better on these nonlinear, highly nonstationary systems than other conventional correlation analyses. Signals are studied individually, but also jointly to understand the nature and cause of the variability in the runoff-rainfall relationship. On short (hourly and shorter) timescales, anthropogenic processes such as pumping as well as naturally intermittent processes can be identified and distinguished. On longer timescales, the wavelet transform allows the identification of inter-annual as well as annual and seasonal components to variation in runoff and its relationship to precipitation.

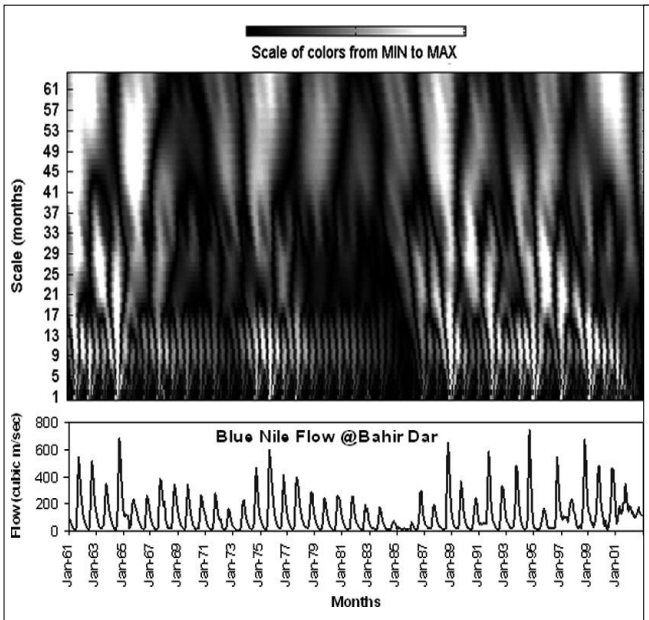

Figure 3.9: Continuous wavelet transform coefficients of monthly runoff data from the Blue Nile at Bahir Dar 1961-2003. The variation in rainfall is well reflected, as are temporary variations at different scales. Source: Melesse et al. (2009)

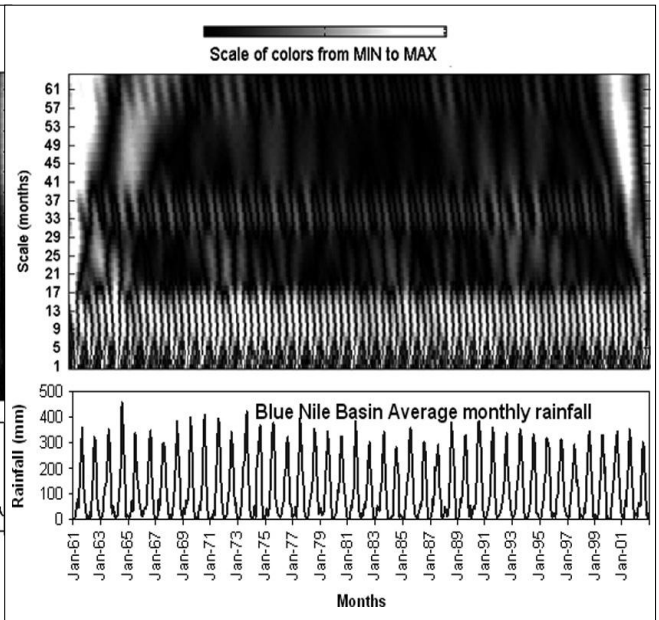

Figure 3.10: Continuous wavelet transform coefficients of monthly rainfall data from the Blue Nile basin 1961-2003; Strong seasonal variation at a scale of 4-16 months is apparent, as is variability at ~31-37 and 56-64 month scales. Source: Melesse et al. (2009)

4. Data and Methods

4.1 Study Site

The Paakitsoq area is a marginal region of the western GrIS close to the Swiss Camp (69.57°N 49.31°W, 1175m asl; Figure 4.1, 4.2), a research base maintained by CIRES at the University of Colorado Boulder. The area has been studied extensively both due to its relative accessibility and proximity to airports and because runoff from the ice sheet is used for the generation of hydroelectric power (Mottram et al., 2009). The potential causal and spatiotemporal links between icemelt, runoff and ice-sheet flow velocity have been extensively studied here (Zwally et al., 2002; Price et al., 2008), although the applicability of this data to wider regions of the ice sheet has been questioned (Hoffman et al., 2011). Similarly, research has been undertaken into englacial drainage (Benn et al., 2009; Catania and Neumann, 2010) and the surface lakes also visible in Figure 4.2 as dark blue spots (Box and Ski, 2007; McMillan et al., 2007; Das et al., 2008).

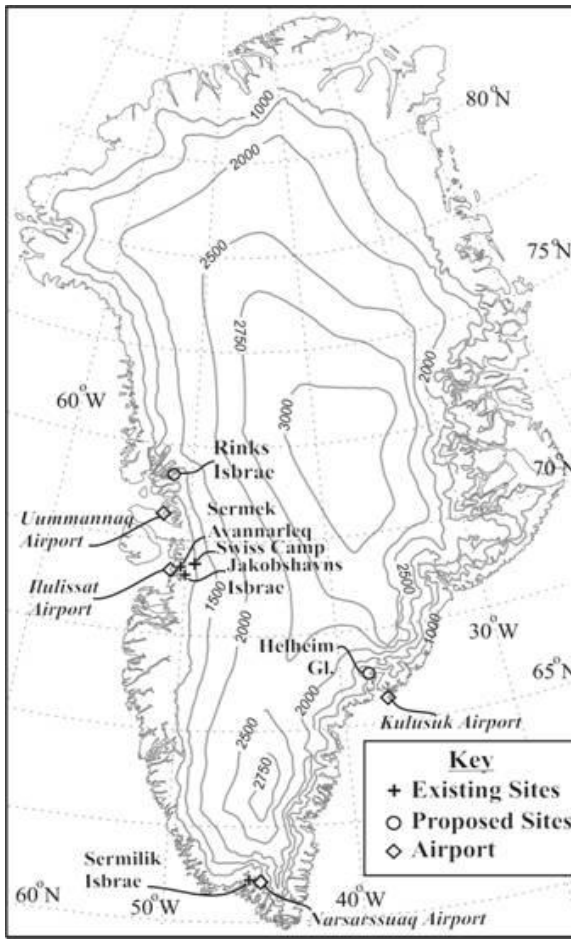

Figure 4.1: Map of Greenland with Swiss Camp, Ilulissat and Jakobshavn Isbrae noted. Weather stations Jar 1-3 are situated Swiss Camp and Ilulissat.

The Paakitsoq basin is situated north of Jakobshavn Isbrae and has a total catchment area of 326km², of which ~87% is covered by ice. Four land-terminating outlet glaciers drain the catchment, flowing into three lakes (Nos. 233, 326 and 187; Figure 4.2), the former two of which drain into the latter. This drainage pattern has been stable for >40 years (Kern-Hanssen, 1988), suggesting that spatial runoff patterns from the ice have been similarly consistent. Indeed, comparisons of satellite imagery with aerial photographs and

maps from the first half of the 20th century show stable drainage patterns supraglacially as surface topography is controlled predominantly by the undulating bed (Thomsen, 1988), which also means that the thickest ice is located east of Swiss Camp (Mottram et al., 2009; Figure 4.2). Generally, the ice slopes down towards the margins and also southward to the Jakobshavn basin.

The equilibrium line was between 1000m and 1250m asl in the 1980s (Ahlstrom, 2007), although observations by Zwally et al. (2002) suggest that this may have risen as high as 1400m asl by 2000, with Swiss Camp at 1175m asl and the JAR1 meteorological station, from which data used here originates, at 962m asl (Steffen and Box, 2001; Figure 4.2).

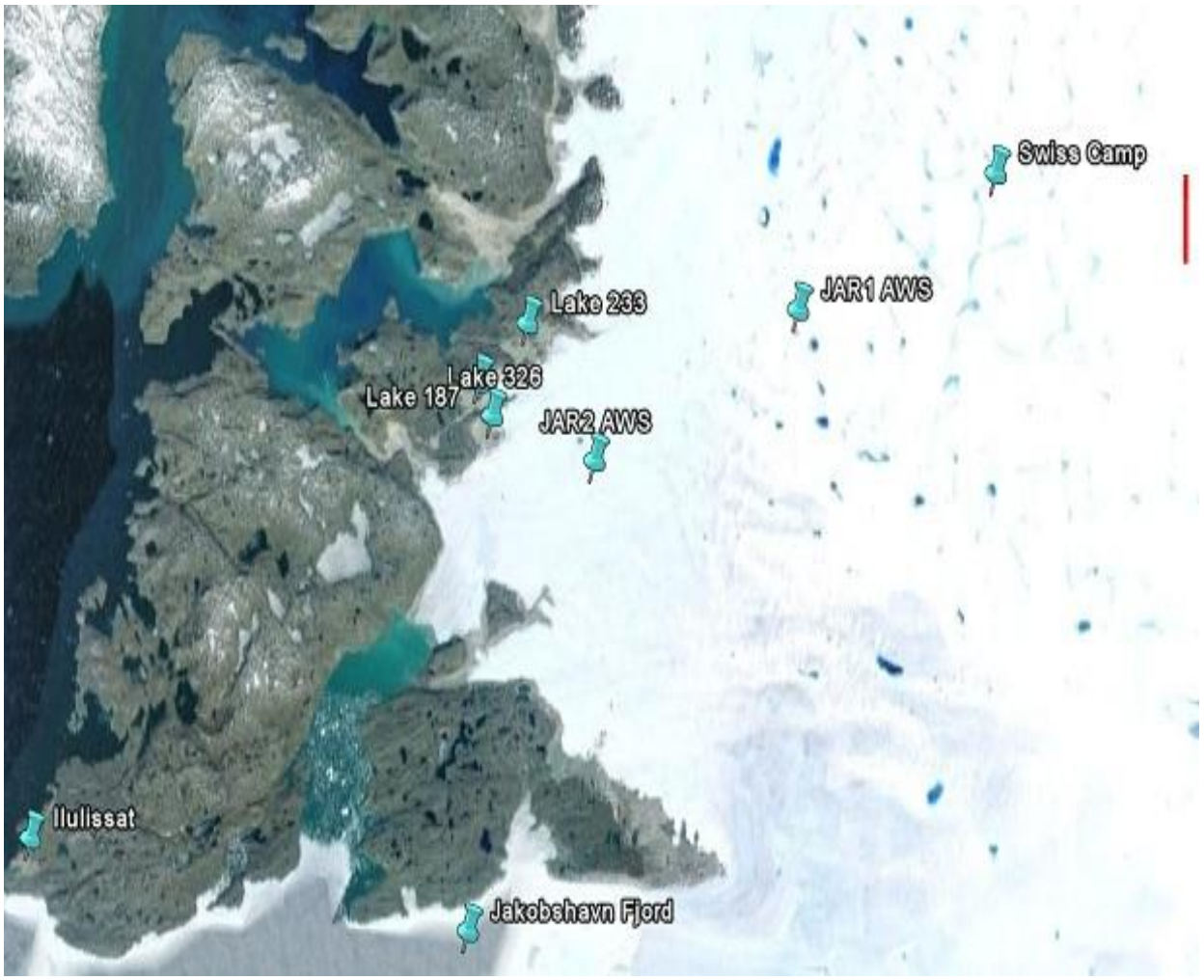

Figure 4.2: Map of the Paakitsoq region from Google Earth, 6th June 2012, showing the town of Ilulissat, Lakes 233, 326 and 187, and location of the JAR1, JAR2 and Swiss Camp AWS and Jakobshavn Fjord to the south. The red lineon the right edge of the image is 5km long for scale. Source: Google Earth.

4.2 Data and Treatment

4.2.1 Meteorological Data

Meteorological data are supplied by the Greenland Climate Network (GCNet; Steffen and Box, 2001). Data from the JAR1 automatic weather station (AWS) were used, which is situated at 69° 29' 54"N, 49° 40' 54"W and at an altitude of 962m asl (Figure 4.2). At this AWS specific calibration of instruments was not required and factory settings could be used for all instruments and measurements. There are other AWS nearby (JAR2 and Swiss Camp), but JAR2 has a significantly shorter record beginning in mid-1999 and Swiss Camp is actually upglacier from the drainage basins of the lakes outlined in Section 4.1. In fact, water from this area drains southwards towards Jakobshavn Isbrae (Mottram et al., 2009). Furthermore, AWS at elevations above ~1100m are at risk of measurement errors due to frost (Steffen and Box, 2001).

All data are collected directly from the AWS once they are revisited, so that there are no gaps due to data loss in transmission. However, sources of error do exist and may have affected some of the time series. The instruments and details of data collection are listed in Table 4.1.

Parameter	Instrument	Instrument Accuracy	Sample Interval
Air Temperature	Campbell Sci. CS-500	0.1°C	60 sec
Net SW Radiation	REBS Q* 7	5-50%	15 sec

Table 4.1: Instruments used to measure the variables used herein, with accuracies and sample intervals. Source: Steffen and Box (2001).

Incoming solar (shortwave) radiation can be affected, particularly during periods of midnight sun (Figure 5.16), by shading by the AWS platform itself, both on the upward-facing part of the pyranometer and the ice surface underneath the downward-facing part (as this changes the surface's albedo). This problem is minimised by arraying the AWS arm so that this problem only arises during two hours near midnight, slightly affecting the 3-hour average. Frost rarely causes a problem due to small instrument size (Steffen and Box, 2001).

Measurement errors can occur in air temperature, mostly due to overheating of sensors if they are non-ventilated, and at times when low wind speeds and high incident radiation occur jointly. Where this is suspected to be the case, Steffen and Box (2001) applied correction algorithms to the data. Similarly, relative humidity data have been corrected to reflect humidity relative to ice rather than water for subzero temperatures.

The raw time series were truncated to a length that allowed time series from all years in the observation period (1997-2005) to have the same start and end date/time. The hourly data were then averaged to produce 3-hourly series (to correspond to the 3-hourly discharge data) of length 1483, which corresponds to 4449 hours or 185 days and 9 hours, from 27th May, 09:00, to 28th November, 18:00. These series were then zero-padded (see Section 4.3.1) to a length of 2000 for use in wavelet methods.

In 2000, meteorological data are missing after 5th September, 1200. In 2003, several smaller gaps exist for net shortwave radiation: 18th Sept 1200-2100, 19th Sept 0000-0300, 27th Sept 18:00-28th Sept 03:00, 30th Sept 12:00-18:00. From 3rd October 21:00 to 4th October 21:00, data for both net shortwave radiation and air temperature are missing. Since complete datasets are needed for the multivariate wavelet methods used in Section 5.3, these gaps have been replaced with zeroes for this section. Since the gaps are short relative to the whole signal this is unlikely to have a significant impact apart from the missing autumn section in 2000. In the univariate CWT graphs (Section 5.2), the graphs corresponding to these years show gaps where data is missing.

4.2.2 Discharge Data

Discharge data were obtained by ASIAQ at Hydropower Station No. 187, at lake No. 437 (Figure 4.2). Discharge is measured by conversion from relative lake levels (Dorthe Petersen, 2010: personal comm.).

Three-hourly data is used from 1997 to 2005, with the annual series truncated to the same

beginning and end dates as the meteorological data for joint use of the series.

4.3 Methods

4.3.1 The Continuous Wavelet Transform

All transforms use the Morlet wavelet – first developed by Grossmann and Morlet (1984), it is defined by Daubechies (1994) as

$$morl(x) = e^{-\frac{x^2}{2}} \cos(5x) \tag{17}$$

and is shown in Figure 4.3. This wavelet is advantageous due to its relatively even balance between time and frequency localisation and resolution (Foufoula-Georgiou and Kumar, 1994; Grinsted et al., 2004), a feature which arises from the fact that its Gaussian envelop allows maximum overall localisation, or minimum uncertainty, within the constraints of Heisenberg's uncertainty principle (Labat, 2005; Aguiar-Conraria and Soares, 2011). It has accordingly been widely used in geophysical applications (e.g. Little, 1994; Lau and Weng, 1995; Schoene and Fiebig, 2009; Lenz et al., 2011) and is highly appropriate for this project,

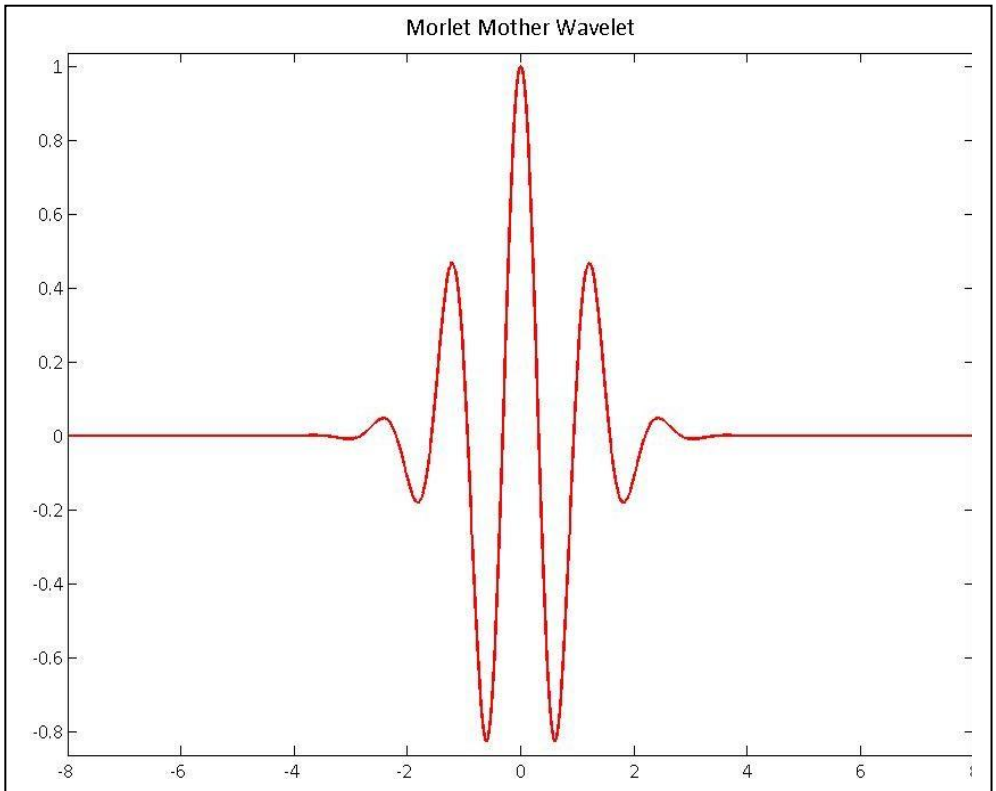

Figure 4.3: The Morlet mother wavelet used for all wavelet applications in this project.

which requires good resolution in both time and frequency. However, the Morlet wavelet is more affected by edge effects than other wavelets commonly used in geophysical applications such as the Mexican Hat wavelet (Cazelles et al., 2008; Torrence and Compo, 1998). Each signal is therefore padded with zeroes at each end to ensure that the actual time series itself is unaffected by these edge effects. Each signal (length: 1483 3-hourly observations) is padded symmetrically to produce signals of length 2000, which accounts for the white space at the edges of the graphs presented in Section 5. This process means that the series themselves begin at observation 258 and end at observation 1741.

The CWTs were run including scales (shown on the y-axes of the CWT graphs; Figure 4.4) from 1 to either 14 or 20. This is because a scale of 7 corresponds to frequency of 24h and is therefore the main scale of interest for investigating diurnal variation; a scale of 13 corresponds to oscillations at a frequency of 48h, while a scale of 19 corresponds to 72-hour frequencies. Variation at such two- and three-day frequencies is feasible, but the main focus of this project is therefore on the diurnal scale of 7.

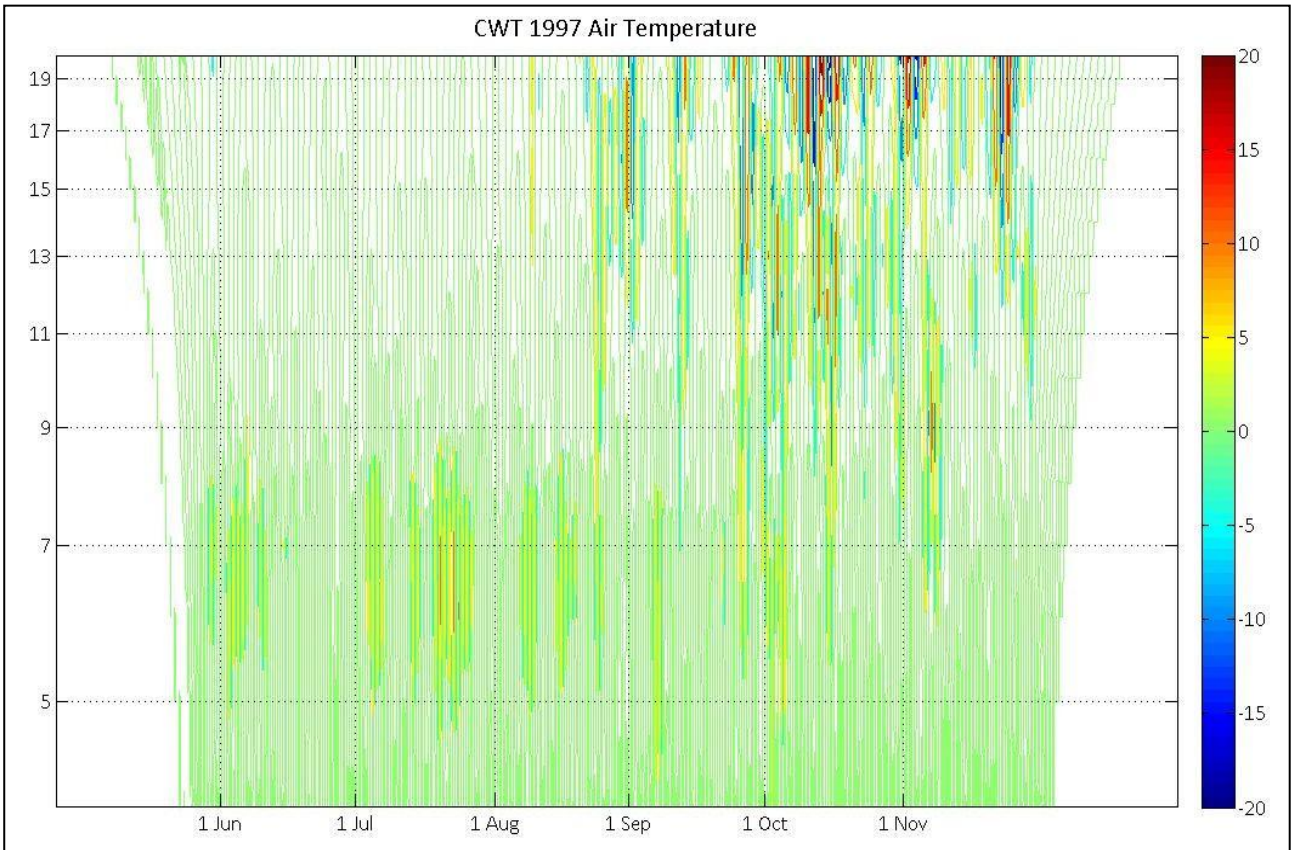

Figure 4.4: Example of the CWT plots used in this project. The x-axis shows time, the y-axis scales (corresponding to frequencies, with 7 corresponding to a 24h frequency) while the colour scale denotes the power of variability at a given time and scale.

Figure 4.4 shows an example CWT graph. These show the power of variation (colour scale) at a given frequency, or scale (y-axis) and at a given point in time (x-axis). “Power” here refers to what would be the amplitude in the time domain, i.e. how strong the variation in a time series is at a given time and scale. To illustrate this point, note that for each scale included in the transform, the CWT output consists of a sinusoid which rises in magnitude where variation at that scale has greater power. An example of such a sinusoid is given in Figure 4.5 – it corresponds to Figure 4.4 and shows variability at a scale of 7, i.e. the diurnal scale. The parts of Figure 4.5 with the greatest amplitude correspond perfectly to the high-power periods at scale 7 in Figure 4.4, illustrating how CWT graphs are composed of these individual sinusoids, one for each scale.

The CWT graph shown in Figure 4.4 is the two-dimensional representation of a three-dimensional matrix (Figure 4.6) which shows the oscillating nature of the CWT. This also explains why high (red) and apparently low (blue) power always occur together, even if this is not always visible in the two-dimensional representation.

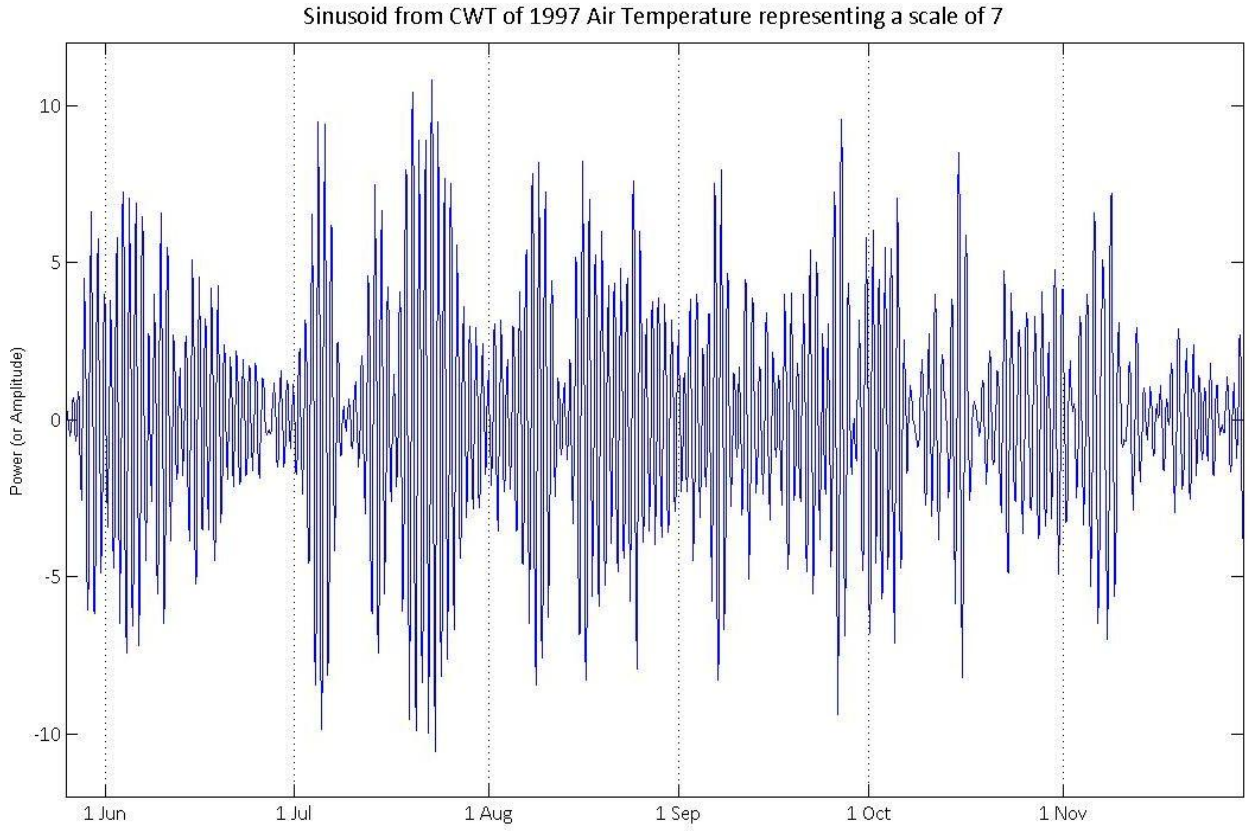

Figure 4.5: A single sinusoid representing one scale of a CWT; Figure 5.8 is made up of 20 of these (one for each of the 20 scales) along the y-axis.

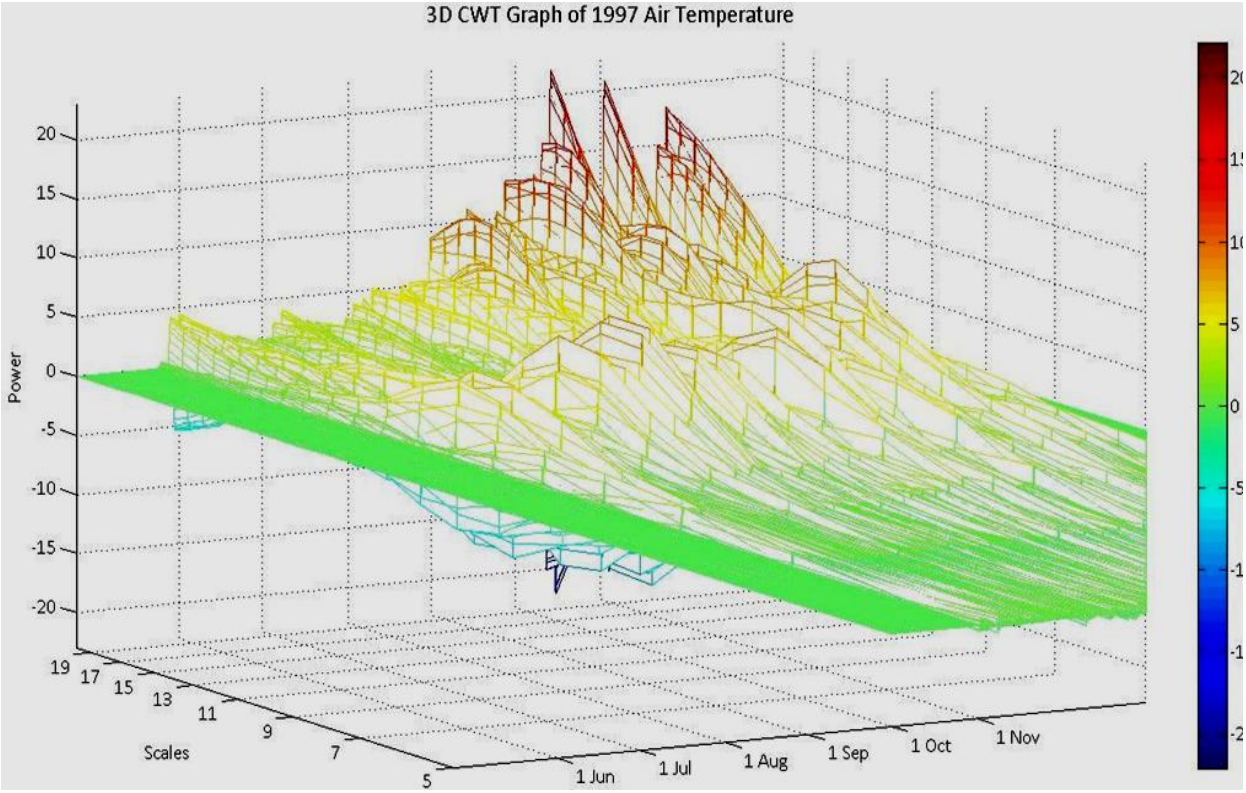

Figure 4.6: Three-dimensional representation of the 1997 air temperature CWT graph (Figure 4.4). Note the oscillating nature of the CWT, with a peak (yellow/red) followed by a trough (blue) of the same amplitude (or power).

4.3.2 Multivariate analysis using Wavelet Coherence

Above and beyond its application to univariate time series, the CWT is also used to analyse the covariance between two time series, including nonstationary ones whose mean and/or variance may change over time (Whitcher et al., 2000). Normal cross-correlation, given for two functions x(t) and y(t) by

$$R_{XY} = \frac{E[x(t)y(t)]}{E[x(t)^2]E[y(t)^2]} \qquad \text{where E stands for expected values} \qquad (13)$$

quantifies the degree of similarity between x and y and can be modified for a time lag or lead which, however, is constant for the duration of the signal (Labat, 2005). Cross-correlation is thus of very limited use if one or both of the signals are nonstationary. This is an entirely feasible prospect in this project as it is likely that seasonal data exhibit a trend, and quite possible that interannual data also follow a long-term trend.

The cross-wavelet transform (XWT) highlights areas of high common power in the two signals analysed, and can reveal information about the phase relationship between the two in the form of an angle, which might be expected to be largely consistent through time if there is a physical relationship between two variables (Grinsted et al., 2004).

Using the XWT, denoted W_{XY}, and the CWTs of series x and y, denoted W_X and W_Y respectively, wavelet coherence functions (WCO) are calculated. These highlight the local correlation between the two time series in question, in time-frequency space (rather than time-amplitude space). Wavelet coherence is useful as an indicator of local covariation between the two signals in time-frequency space, i.e. it shows areas of phase-locked behaviour. For two time series x and y, wavelet coherence ς requires a smoothing operator S and is given by

$$\varsigma_{xy} = \frac{S(W_{xy})}{\sqrt{S(|W_x|)^2 S(|W_y|)^2}} \qquad \text{(Aguiar-Conraria and Soares, 2011)} \qquad (15)$$

Wavelet coherence is between 0 and 1, where 0 represents no coherence and 1 represents perfect coherence.

Besides the WCO, phase differences between the series will be shown as well as the average wavelet coherence at each scale over the whole series. To illustrate, Figure 4.7 shows an example of the plots used in Section 5.3 to show the results of multivariate wavelet analysis. The top graph shows the wavelet coherence between the two signals analysed, with scales on the y-axis annotated with their corresponding frequencies and shown on a log scale to highlight diurnal-scale coherence.

The middle plot shows the phase difference on the y-axis. It is given in angles, i.e. over the interval (-π, π), where values >0 indicate that variable y is lagging variable x, while values <0 indicate that x is lagging y. 0 means that the two series are perfectly in phase, while π /-π means perfect antiphase with y/x lagging, respectively. (π/2)/(-π/2) mean that the series are completely out of phase with y/x lagging, respectively. That is, when phase difference >0, the series are in imperfect phase with x leading, and when it is <0 they are in imperfect

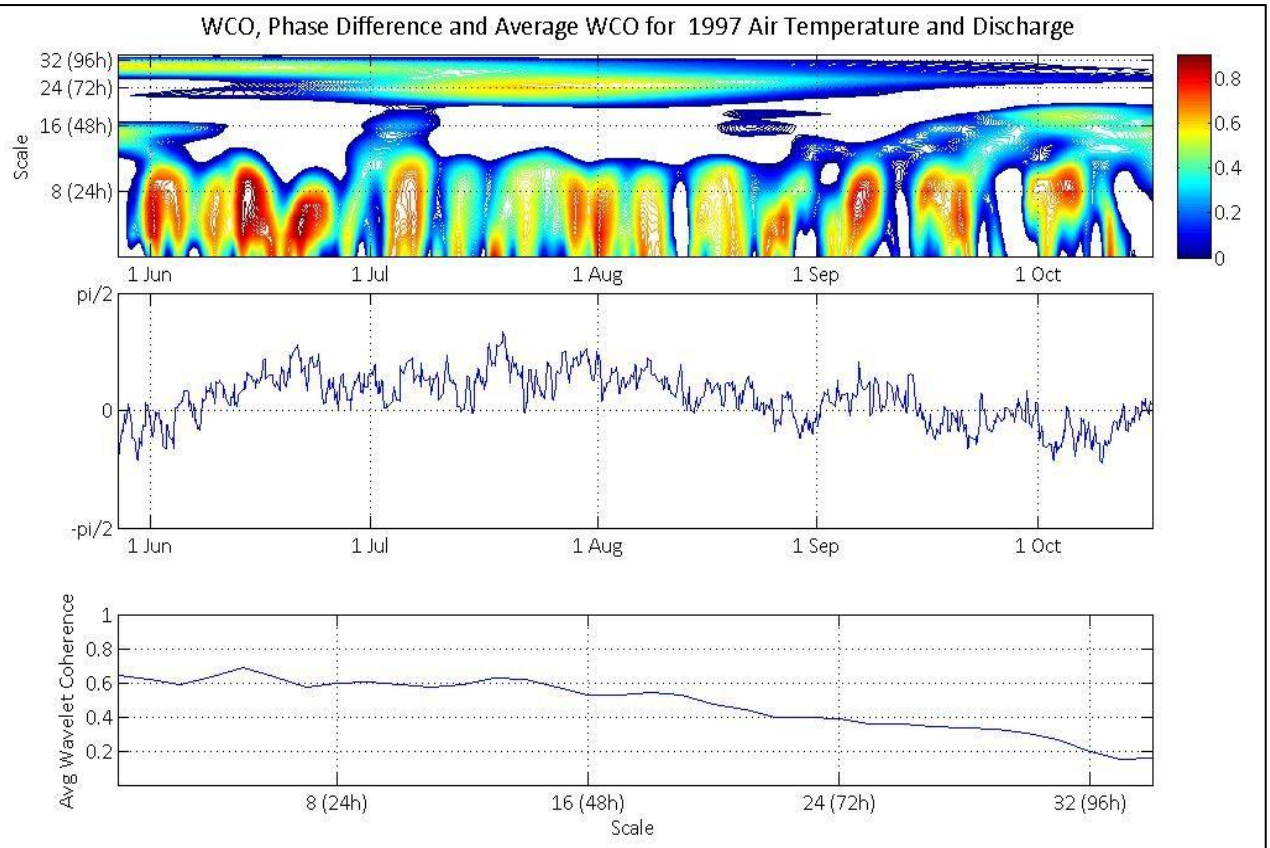

Figure 4.7: Example of the multivariate wavelet analysis plots used in this project. The top graph is the WCO, the middle graph shows the phase difference and the bottom graph shows the average wavelet coherence at each scale.

phase with y leading.

The bottom graph shows average wavelet coherence each scale over the whole series. Note that the x-axis now shows the scales rather than time, while the y-axis shows the average coherence levels at each scale.

5. Results and Analysis

In this section, results of wavelet analyses are reported. Section 5.1 provides a brief description of the data series used (air temperature (AT), net shortwave radiation (NR) and discharge (Q)). Section 5.2 details the results of the CWT applied to each of these variables for each year 1997-2005, while Section 5.3 reports the results of multivariate wavelet analysis including wavelet coherence and phase differences. The time series were truncated to run from 27th May (12:00) to 28th November (18:00) to capture as much of the melt season as possible while maintaining equal time series length throughout the years. For the purposes of this project, "summer" refers to June/July/August (JJA) and "autumn" refers to September/October/November (SON).

5.1 Data Description

5.1.1 Air Temperature

Generally, air temperature (AT) rises throughout June and July before gradually dropping off again in August, and more quickly from September onwards (Figure 5.1). Interannual variability decreases during early summer and is smallest in midsummer, in late July/early August. AT rises up to 5°C during this period before dropping below zero (on average) in mid-August.

There are several anomalous events apparent from the AT signals. In late July 2000, temperatures drop to -10°C, when the interannual average is above 0°C, and in early September 1999 temperatures of -15°C are recorded despite a 1997-2005 average for this time of year of close to 0°C. 1999 is very cold in general, with unusually cold periods throughout June, October and early November (Figure 5.1)

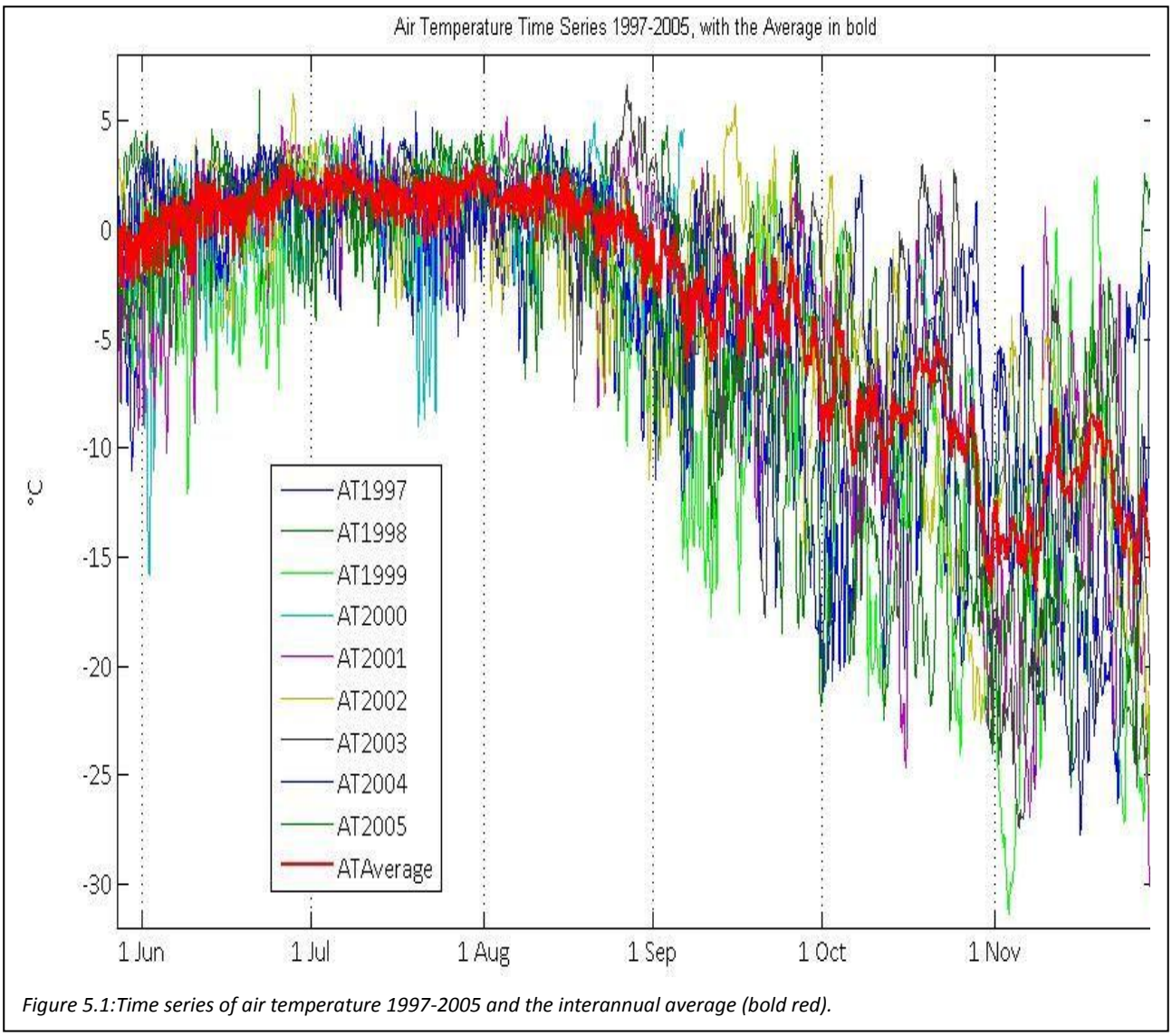

Figure 5.1:Time series of air temperature 1997-2005 and the interannual average (bold red).

Unusually warm periods occur in the second half of September 2002, when AT peaks at over 5°C; the interannual average is well under 0°C. 2001 and 2003 both see brief episodes of temperatures around 0°C in the second half of October, ~10°C above the average.

The seasonal change in AT variability is confirmed by the AT standard deviations for the summer and autumn months (Figure 5.2). Annual standard deviation (blue) is clearly driven by autumn standard deviations (green), while summer values are far lower. The range of summer AT is also lower between years at any given point in time than the range of autumn AT. While there is no clear trend apparent from the few observations available here, the autumn of 1999 with its numerous cold snaps exhibits the highest overall SD of all years. Its summer SD is also the highest, probably owing to the numerous cold episodes in June (Figure 5.1).

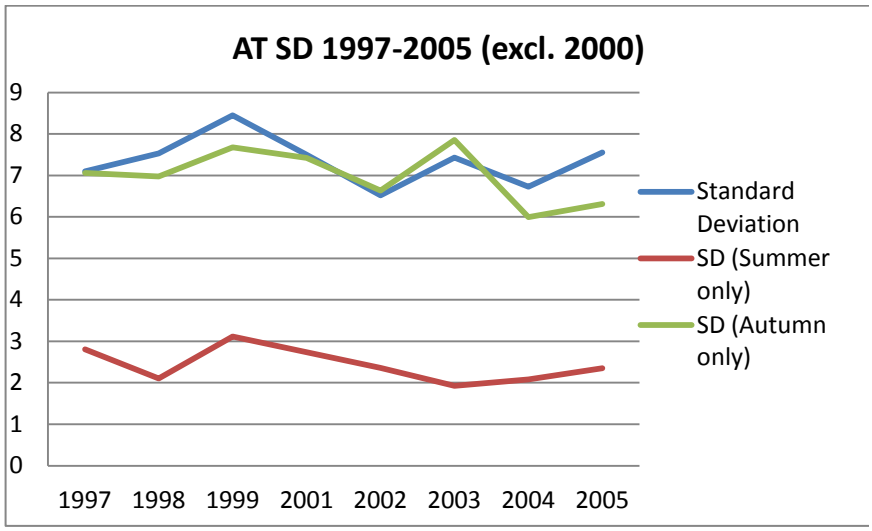

Figure 5.3: Standard deviations for air temperature, 1997-2005, and summer-only and autumn-only values; 2000 is excluded due to missing data which would cause a bias in autumn and overall values.

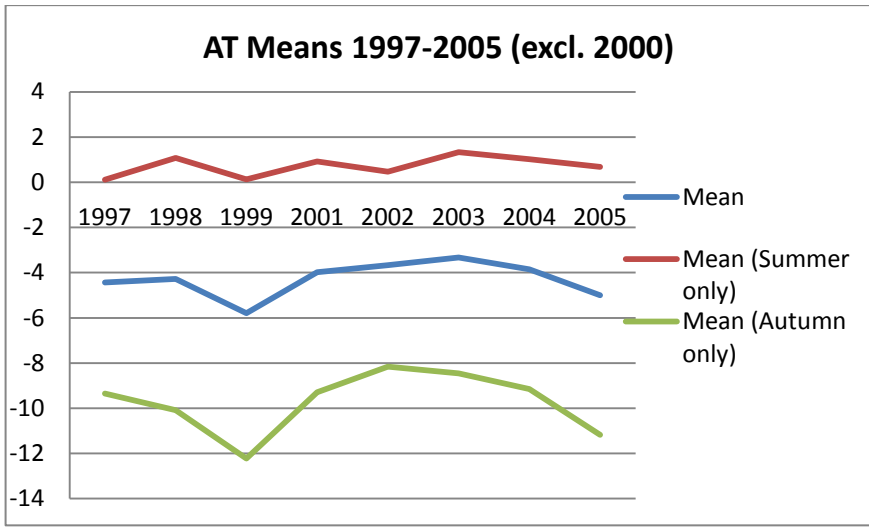

Figure 5.2: Means for air temperature, 1997-2005, and summer-only and autumn-only values; 2000 is excluded due to missing data which would cause a bias in autumn and overall values.

The annual means for AT over the years are fairly consistent (Figure 5.3), with no clear interannual trend discernible. It is possible that autumn AT in particular exhibits some cyclic behaviour, but this is unclear also due to the short observation period of 9 years. 1999 once again stands out as an unusually cold year in both summer and particularly autumn, while autumn averages are much higher in the subsequent 3 years. Summer averages seem to oscillate over the observation period, with 1998, 2001 and 2003 being slightly warmer than the remaining years.

5.1.2 Net Shortwave Radiation

NR exhibits a roughly similar trend to AT over the course of the melt season in that it peaks in late July/early August, with a drop back to consistently low levels in early autumn (Figure 5.4). There are exceptions to this pattern, however. In 1997, maximum NR is reached in late

June and there is a period of almost no NR in August. 2000 NR is low throughout the summer, with no significant peaks at all; autumn data for this year is missing. Conversely, 2004 is very variable through the observation period, and the highest NR levels observed 1997-2005 are observed in August of this year; several peaks close to this level occur in August and September, with a drop to average autumn levels only occurring in October. 2001 is the most "regular" year with respect to NR, with a steady increase towards a peak in early August followed by an equally gradual decline until September, when a sudden drop in NR occurs.

The relatively sudden drop to much lower NR levels in early autumn, which is observable in most years (with the exception of 1997, 1999 and 2005, when this decline occurs in mid-

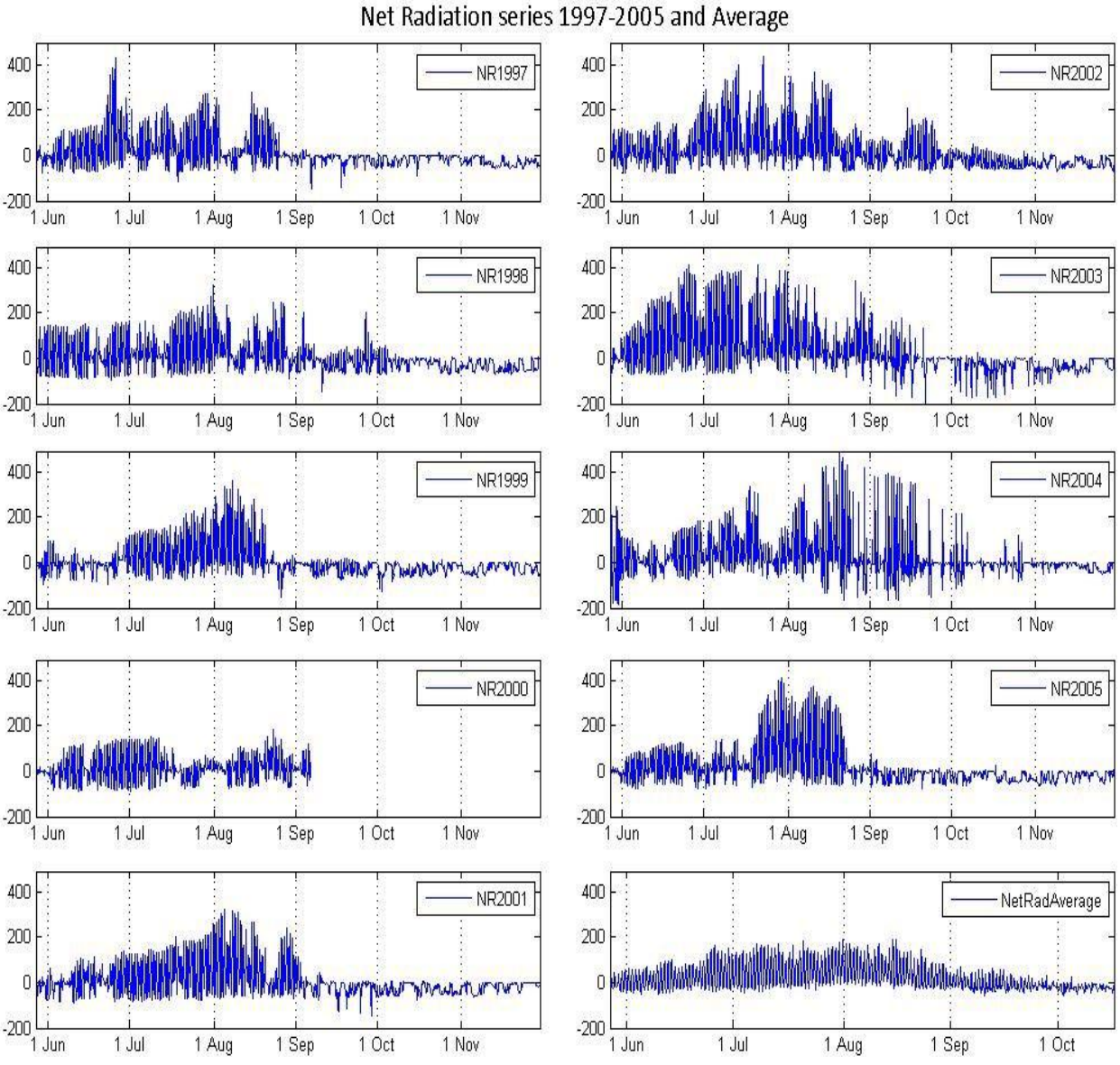

Figure 5.4:Time series of net shortwave 1997-2005 and the interannual average.

August) may be due to the changing angle of the sun, as the period of midnight sun draws to an end. However, this does not explain the continued high variability in 2004, or the three years when NR drops off earlier than usual. The average NR series (Figure 5.4) shows this decline from late August onwards more clearly, although this series is less variable and lower than the annual series due to the high variability between years.

The standard deviation of NR exhibits the opposite behaviour to AT (Figure 5.5). Summer SD exceeds autumn levels for NR and primarily drives annual SD. The NR peaks in September and October 2004 are apparent in the very high autumn SD for this year, while summer and overall SD is greatest in 2003. On the whole, NR annual SD follows summer values more closely than autumn ones while AT annual SD is driven mostly by autumn SD. This suggests that AT is governed by factors besides NR.

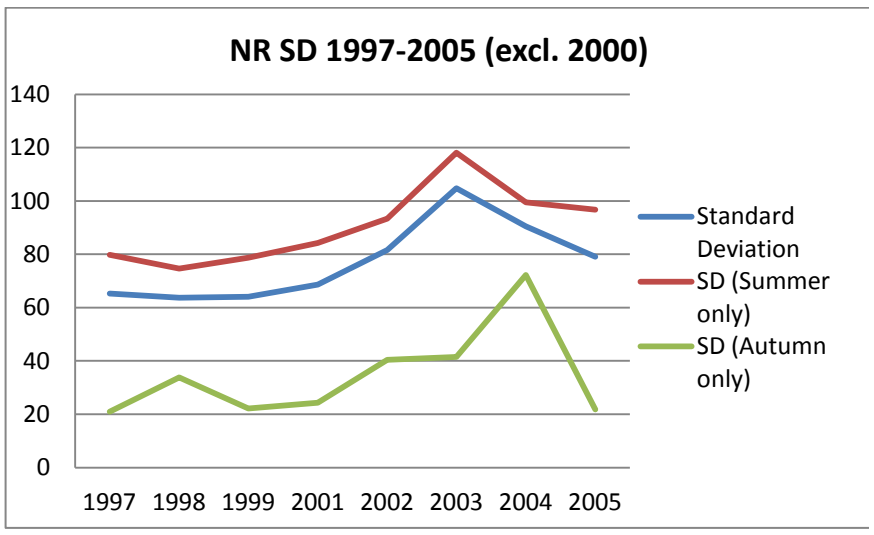

Figure 5.5: Standard deviations for net radiation, 1997-2005, and summer-only and autumn-only values; 2000 is excluded due to missing data which would cause a bias in autumn and overall values.

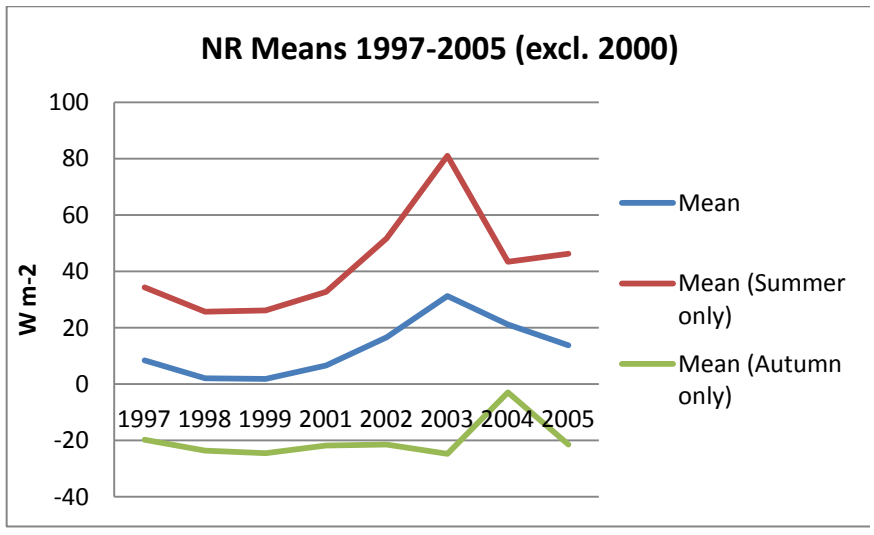

Figure 5.6: Means for net radiation, 1997-2005, and summer-only and autumn-only values; 2000 is excluded due to missing data which would cause a bias in autumn and overall values.

Annual NR means (Figure 5.6) exhibit a slight increasing trend, although 2003 is something of an outlier. The summer of 2003 exhibits a particularly long, consistent period of high NR which causes

summer and annual mean NR to be unusually high. This may also be due to some missing autumn data from 2003 which could have introduced a bias into autumn and annual standard deviations. Autumn NR is particularly high in 2004, so that year's overall mean may also be anomalous. Data series spanning more years would be required to assess whether this is an interannual or interdecadal trend towards increasing summer variance in NR or just a few unusual years – after all, 2005 mean NR is back at 2002 levels.

5.1.3 Discharge

Four years (1998, 2001, 2003, 2005) have large, anomalous peak Q levels which make plotting of all series on a single graph difficult. These four years are therefore referred to as "flood years" while the other years (1997, 1999, 2000, 2002, 2004) will be referred to as "non-flood years". These two groups are plotted separately in Figures 5.7 and 5.8, respectively, with the interannual average (of all years) shown on both graphs to illustrate the differences in magnitude.

For Q, more so than with AT or NR, there is a contrast between very low "winter" levels not shown here and higher "summer" levels. In most years, the onset of high discharge tends to occur within a 20-day window from late May to mid-June, except for 1999 when discharge remains low until the very end of June before rising rapidly to a first maximum.

The rise to the first local maximum occurs either through a sudden, sharp rise (as in 1997-2000, 2002, 2004) or more gradually (2001, 2003, 2005). The latter three are the years with the three largest discharge peaks of the entire observation period, although it is unclear whether early-summer discharge patterns and later large peaks are causally related. In most years, discharge levels begin to deviate from low, winter levels (near zero) in late May or the first week of June (with the exception of 1999 and 2001, when discharge only begins to rise in late and mid-June, respectively). This indicates that variability, as well as an extent of covariation with AT and/or NR should be present early on in the time series and this should be reflected in the wavelet analyses.

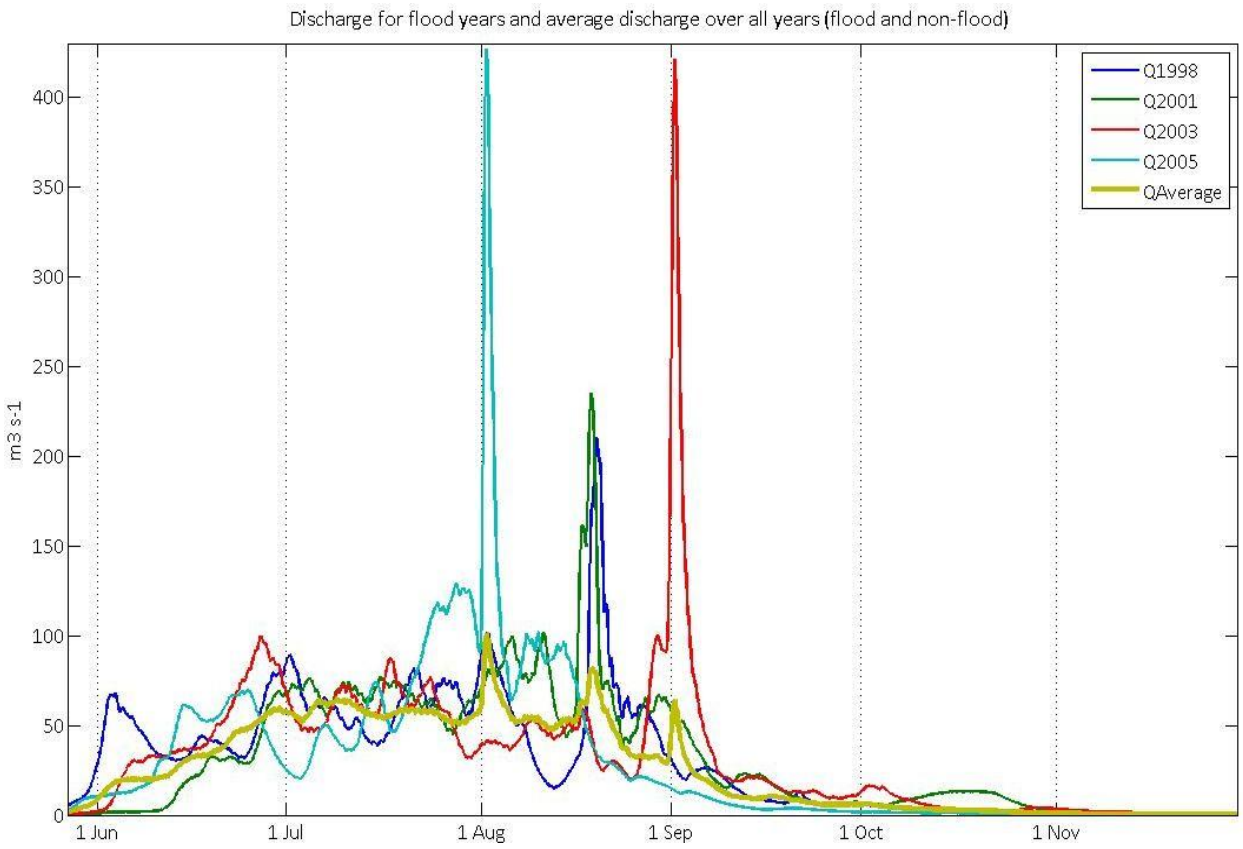

Figure 5.7: Time series of discharge in the "flood years" and the interannual average.

During the summer, variability is high in all years, with Q rarely approaching low (winter) levels. 1997, 1998 and 2000 do record brief periods of unusually low discharge during midsummer (Figures 5.7, 5.8). In 1998 this low occurs just before the flood peak of that year. This might indicate buildup of water in a lake or reservoir before an outburst event.

The interannual average hydrograph clearly shows the peaks from the “flood years”, highlighting the magnitude of these events and their effect even on decadal-scale averages. These events are most likely caused by jökulhlaups from subglacial or proglacial lakes which fill over several years (Dorthe Petersen, ASIAQ, 2010: pers. comm.).

Diurnal fluctuations are visible on the average hydrograph during July and August, suggesting that such fluctuations are present every year. These fluctuations are often difficult to distinguish as they are overlain by larger, often very sudden changes in Q.

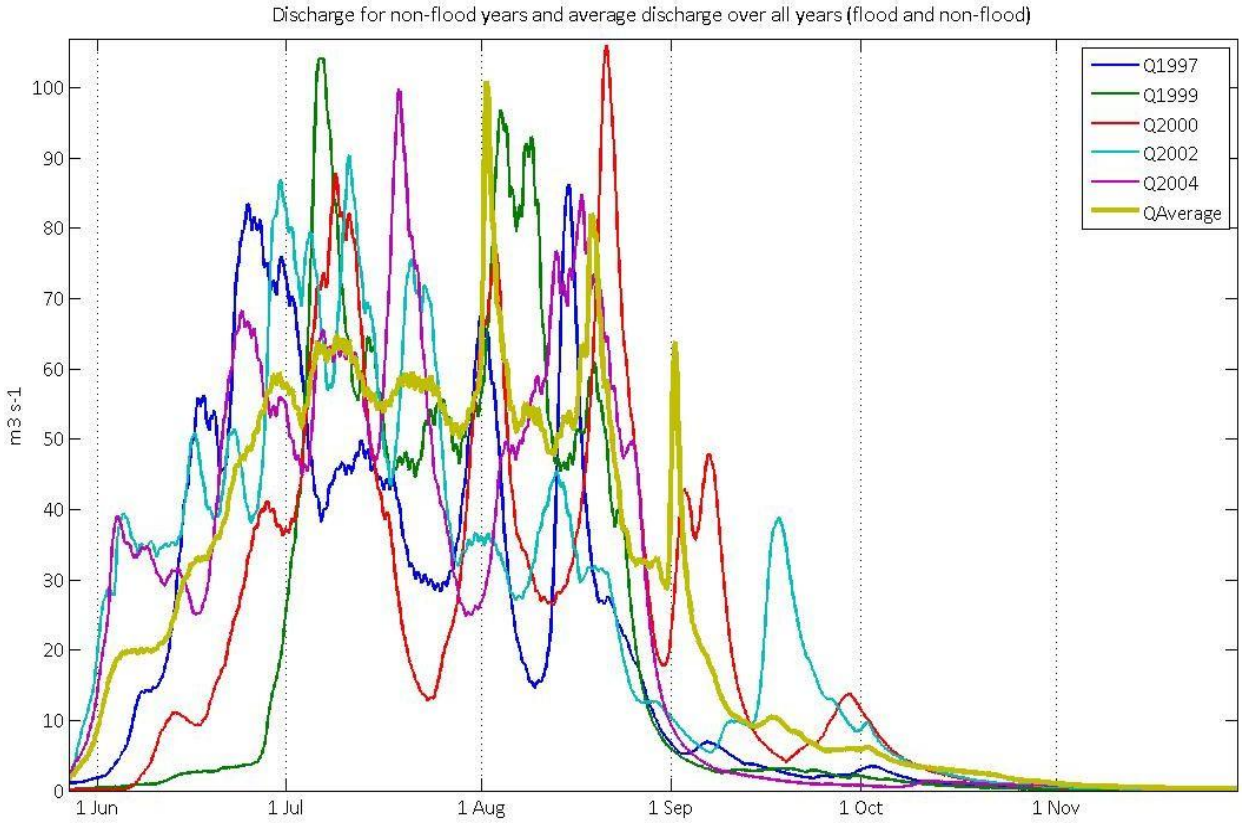

Figure 5.8: Time series of discharge in the "non-flood years" and the interannual average.

Q tends to return to low, winter levels by mid-October in each year, with the notable exception of 2001 when there is a local maximum in mid-October. Even September tends to see very little variation in Q – besides 2001, only 2000 and 2002 exhibit any deviation from a gradual decreasing trend in autumn.

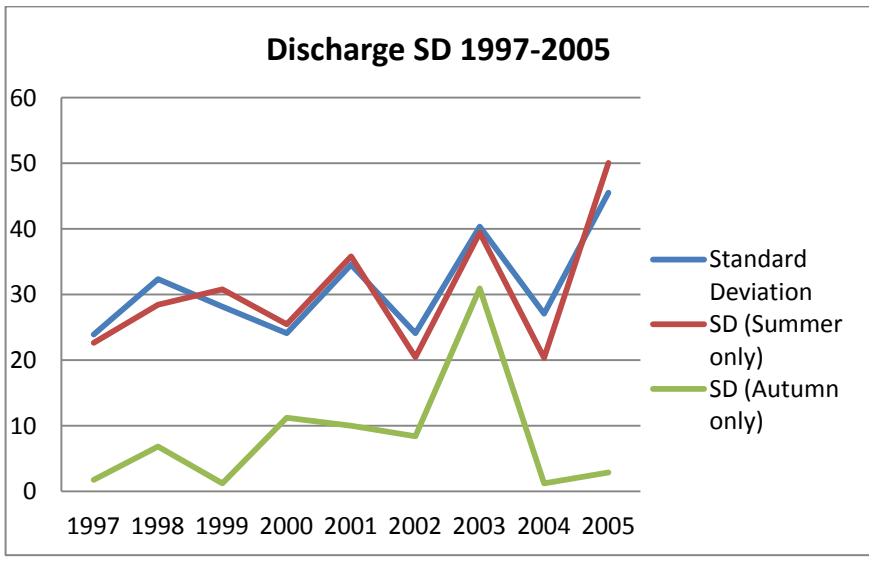

Figure 5.9: Standard deviations for discharge, 1997-2005, and summer-only and autumn-only values.

The standard deviation graphs for Q (Figure 5.9) show that the "flood years" of 2001/3/5 have higher summer variance than all other years, although 1998 does not. This may be because this year has the lowest peak among the flood years,

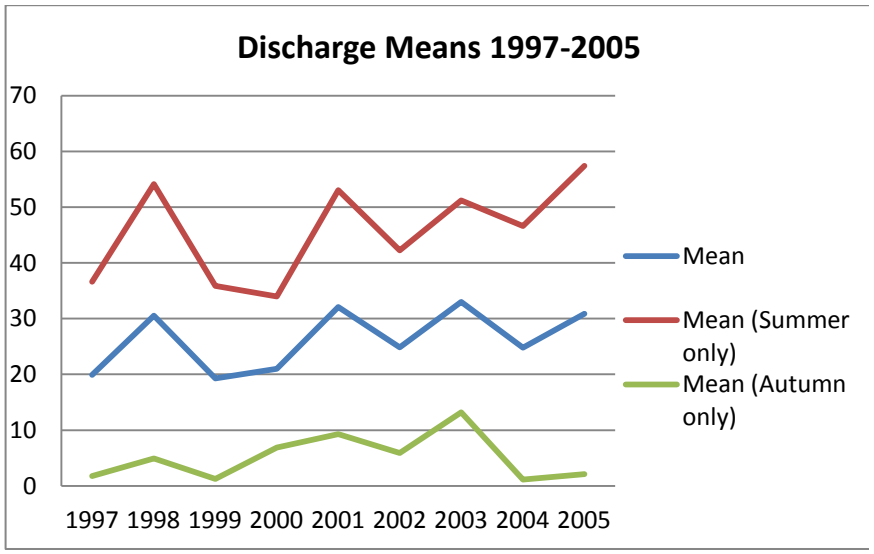

Figure 5.10: Means for net radiation, 1997-2005, and summer-only and autumn-only values.

but also because Q in the summer of 1998 is less variable generally. 2003 exhibits very high autumn variance as the flood peak in this year occurs at the start of September, putting it into the autumn period.

Plotting the means from each year (Figure 5.10) shows the "flood years" more clearly, with summer means in 1998, 2001 and 2005 unusually high and the autumn levels for 2003 being unusually high. Annual means exhibit a slight rising trend, although again the interannual timescale is too short to draw firm conclusions about its significance.

5.2 Continuous Wavelet Transforms

This section presents the continuous wavelet transforms of AT, NR and Q for the melt seasons of 1997-2005, including summer (end of May and JJA) and autumn (SON). Given the above conclusion that AT and NR have different relationships to discharge (Figures 5.3 and 5.4), both these variables are considered here.

For all CWT graphs, a scale of 7 corresponds to a daily (24h) frequency, a scale of 13 to a 2-day (48h) frequency and 19 to a 3-day (72h) frequency. The graphs are shown in the appendices in order to maintain the flow of text in the main body of the dissertation.

5.2.1 Air Temperature

The CWT graphs for the AT time series (Appendix 1) show that variability in AT exhibits a

recurring seasonal contrast between summer and autumn throughout most of the study period of 1997-2005, with summer variability far exceeding that in autumn. Diurnal-scale variability (at a scale of 7) dominates until mid-to-late August, at which point larger-scale (lower-frequency) variation becomes more dominant. This change is reflected in Figure 5.1 which shows that it is at the end of summer that daily maximum and minimum temperatures begin to drop again and both intra- and interannual fluctuations become greater. While the CWT is unrelated to the absolute magnitude of a time series or of individual observations, the AT CWT graphs thus highlight the possibility of using wavelets to discern seasonally shifting patterns.

Diurnal-scale fluctuations appear not to be consistent throughout the summers: the series' power at the daily scale waxes and wanes throughout the summers, as shown by a graph of all years' sinusoids corresponding to scale 7 (Figure 5.11). 2003 is an exception to the presence of summer diurnal-scale variability – in this year there is no visible high-power variation at the diurnal scale at any point during the year in the CWT plot, and Figure 5.11 confirms that the diurnal scale exhibits unusually consistently low power throughout the observation period in 2003.

It is worth noting that despite the apparently rising power of variation at a 48-hour frequency from September onwards (Appendix 1), high power in diurnal-scale variation does not disappear entirely from the signals until later in September – that is, daily and both 2- and 3-day cycles (scales of 13 and 19, respectively) can exhibit high power simultaneously in the AT signal. Most years (except for 2001 and 2003, with 2000 being an unknown due to lack of data from September onwards) exhibit such coexistence of diurnal and larger-scale variability throughout most of September. High-power diurnal variability exhibits a similarly irregular pattern as in summer, though. It is therefore likely that the increase in standard deviation in autumn observed in all time series (Figure 5.2) is due to the growing power of the signal at larger scales (i.e. lower frequencies).

Diurnal cycles are present at different times in different years (Figure 5.11) – while the

2001, 2003 and 2004 signals exhibit relatively low-power variation at this frequency throughout summer, high power in diurnal-scale variability is widespread in June in 1998, 1999, 2000, and to an extent in early June 2001 and in 2005. 1997 and 2002, meanwhile, exhibit much higher power at this scale throughout July and most of August.

The relationship between raw AT values and diurnal-scale variability is illustrated by the graphs in Appendix 2: for each year, the CWT sinusoid corresponding to a scale of 7 is plotted with the corresponding year's raw AT data. Note that while the AT signals are raw values, the CWT sinusoid amplitudes show the power of the variability of that same signal at that point in time (x-axis) at the diurnal scale. The sinusoids hold no information about the power of variation at other timescales, or of the AT signal's absolute magnitude.

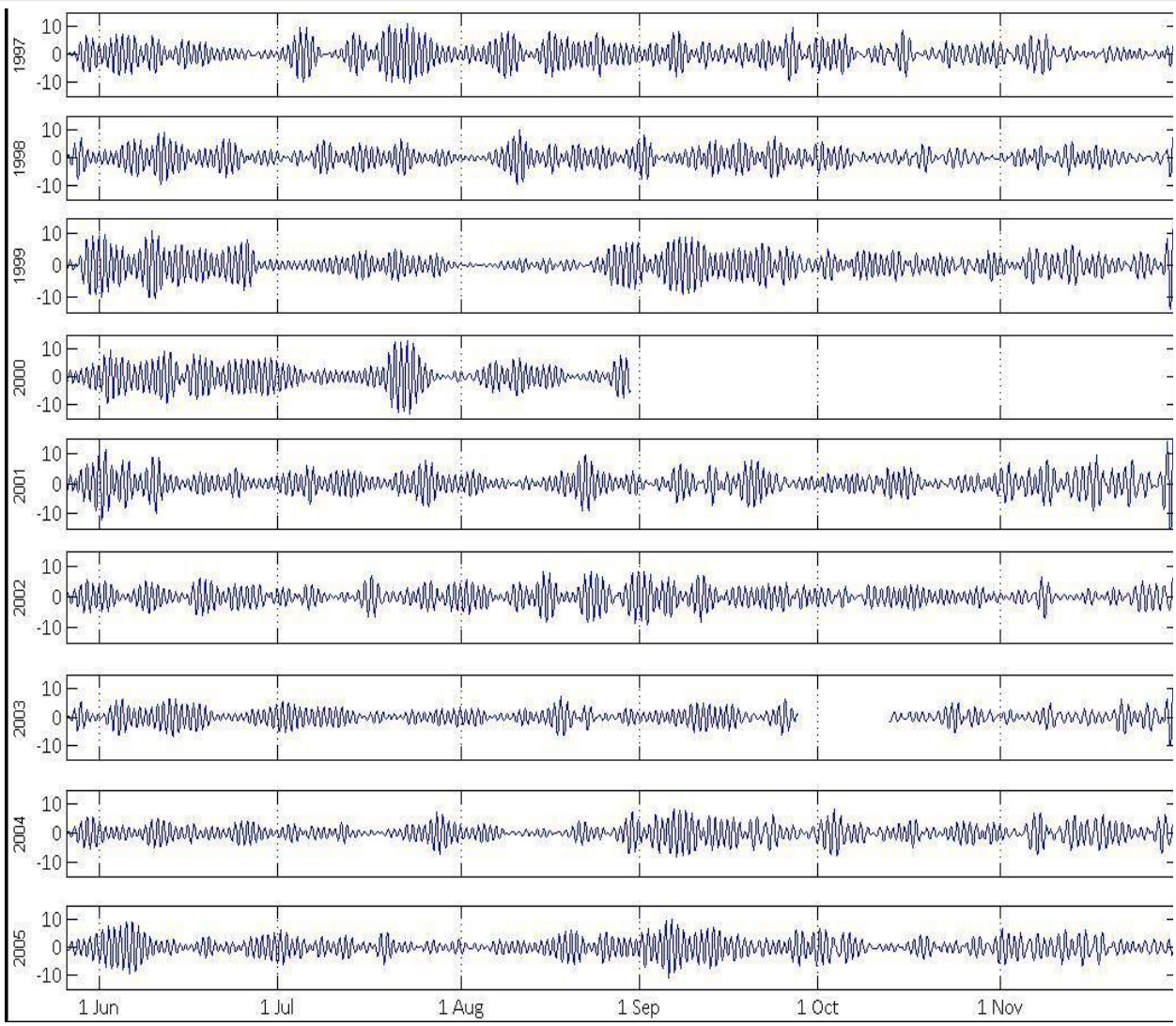

Figure 5.11: Sinusoids corresponding to scale 7 (24h) from every air temperature CWT 1997-2005.

From Appendix 2 it is apparent that across all years, periods of high-power diurnal-scale variability coincide with periods of unusually low temperatures, whether they occur for one day only or over a longer period. This is particularly well illustrated in the first half of October 1997, when both a longer (first week) and a very brief period (in mid-October) of cold temperatures are coincident with periods of high diurnal-scale variability. The high power at the diurnal scale is not due to the large absolute change in temperatures – the CWT sinusoid, as mentioned before, contains no measure of the absolute magnitude of the AT signal. Indeed, brief stints of anomalously high temperatures do not elicit the same response in daily-scale variability: early July and early August 1999 feature prime examples of unusually warm periods which correspond to periods of very low daily-scale power. Similarly, early June and mid-July 2000 contain periods of very high-power daily variability during cold periods, while the warmer period in late July/early August 2000 has far lower power on the 24h scale. The cool but very variable period in late September/early October 2005 further reinforces this observation, with the brief warm peak (~0°C) in the middle of the period coinciding with smaller amplitude in the sinusoid.

5.2.2 Net Shortwave Radiation

Appendix 3 shows the CWT graphs for NR in each year 1997-2005. The majority of years, with the exception of 1997, 2002 and 2004, exhibit prolonged periods of up to 6 weeks with relatively consistently high power, i.e. the “troughs” between power peaks (red on the CWT graphs in Appendix 3) still exhibit high power (yellow on the CWT graphs) rather than dropping to near-zero (green) levels. The three years that do not follow this pattern (1997, 2002, 2004) have stronger fluctuations in diurnal-scale power, which is also reflected in the high summer standard deviations of these years (particularly 2002; Figure 5.5).

The CWT graphs themselves indicate zero power for the autumn period almost without exception, but further detail is visible in the individual diurnal-scale (7) sinusoids (Figure 5.12) which are therefore a useful analytical tool when focussing on just one particular frequency. They show that the return to low, near-zero diurnal-scale power levels from

summer highs occurs in the second half of August in most years. 1998, 2002 and 2004 are anomalous in their high diurnal-scale power during September – while 1999 and 2005 sinusoids also showcase slight power fluctuations during September, these are minimal compared to summer levels. Similarly, 2003 exhibits increasing power before the period of data loss in September. Generally, however, the drop to very low diurnal-scale power relative to summer levels is in contrast to AT, where power does not exhibit a clear-cut difference between summer and autumn.

In summer, NR behaves similarly to AT in that it does not exhibit consistently high diurnal-scale power. In all years, several distinct power peaks are discernible in summer with high power on scales from just under 6 to just over 7, i.e. at 24-hour frequency. Another similarity with the AT data is that variability at scales greater than the diurnal scale is zero throughout all the summers of the observation period and only occurs in autumn. The only exceptions to this occur in 1997, 2002 and 2004 when there are brief occurrences of nonzero power at scales of 9 and higher, i.e. at frequencies >24h. These occurrences are brief, weak relative to diurnal-scale variability and limited to a 6-week time window between July and early August.

Another similarity to AT variability is that in autumn, the power of NR diurnal-scale variability drops to zero very suddenly in most years. The break between high- and low-power diurnal-scale variability occurs in late August/early September in most years. Only 1998, 2002 and 2004 see nonzero power at 24-hour frequencies in autumn, and of these three only 2004 exhibits powers comparable to summer levels (i.e. red on the colour scale).

Besides these similarities, there are also significant differences between the AT and NR signals which are highlighted by the CWT. While AT consistently exhibits high power at scales >7 in autumn in most years, NR has no such feature, with not a single year of high power at scales >7 in autumn. Only 2002 and 2004 exhibit any nonzero power at these scales at all throughout the whole melt season, and this is in summer rather than autumn. This fact is apparent from the standard deviations of AT and NR (Figures 5.2 and 5.5,

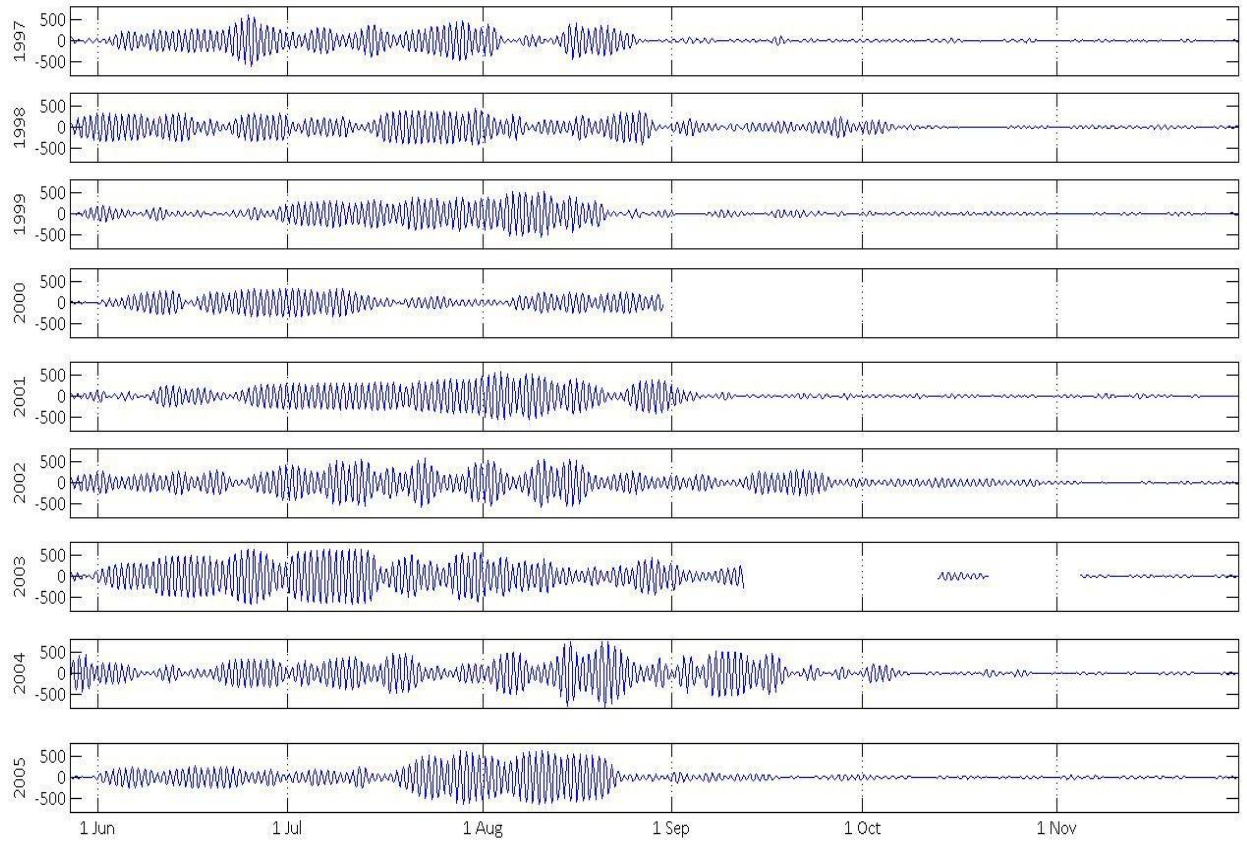

Figure 5.12: Sinusoids corresponding to scale 7 (24h) from every net radiation CWT 1997-2005.

respectively): while the standard deviation of all AT series is higher in autumn than in summer (and annually), the opposite is the case for NR. To a large extent, this is probably due to the absence of high power in variation at frequencies >24h.

The peaks in power at diurnal scales observed in NR during summer are longer in duration than those observed in AT and can last for several weeks (compared to no more than a week for AT). This is due to the close proximity of several peaks (red) and their separation by very short periods of only slightly lower power (yellow), e.g. mid-June to mid-July 2003, while AT tends to exhibit longer periods of at least several days of near-zero power (green) in between peaks. Generally, high power at diurnal scales relative to autumn levels is the norm for NR during summer while it is more unusual and less continuous for AT. This is highlighted by a graph of the sinusoids corresponding to scale 7 for each year (Figure 5.11 and 5.12, respectively).

5.2.3. Discharge

The discharge CWT graphs present some difficulty in that years with extreme maxima (1998, 2001, 2003, 2005; "flood years" from section 5.1) exhibit zero power at all scales and times other than when those maxima occur (Appendix 4) because these peaks represent such a large deviation from the rest of the signal (cf. Figures 5.7, 5.8). On the other hand, the extreme peaks observed in the "flood years" of 1998, 2001, 2003 and 2005 are so large that they produce high power in the CWT graphs at all timescales. This power, however, is an artefact rather than being representative of the actual power of the signal at that point in time as these brief events do not amount up to variation at all timescales – after all, the peaks only tend to last for a day. The "non-flood years" (1997, 1999, 2000, 2002, 2004) do not suffer from this shortcoming to the same extent so the two groups are considered separately.

At the time of the flood peaks, their 7-scale (24h) sinusoids exhibit power an order of magnitude greater than the power levels observed during "non-flood years" (Figure 5.13 – note the different y-axis scales for "flood years"). These extreme peaks therefore "drown out" variation at all scales at other times, which is therefore not represented by the CWT graph (Appendix 4). The "flood years" are not lost to useful analysis, though. They are first considered by themselves in the context of the extreme maxima (using their sinusoids as plotted in Figures 5.13). They are then plotted again with their sinusoids from scale 7 on the same y-axis (-5 to 5) as those from "non-flood years" (Figure 5.15) to describe diurnal-scale variability for all years throughout the observation period.

5.2.3.1 Flood Years

In 1998 and 2001, the peaks in power occur at the same time, are of a similar magnitude and take a similar amount of time to revert to near-zero power. The 2003 and 2005 peaks in power are both greater than in 1998 and 2001, but one takes longer (2005) and the other less time (2003) to revert to near-zero levels (Figure 5.14). This means that the length of time taken after a flood peak to return to near-zero power in diurnal-scale variability is

unrelated to the timing of the occurrence of the peak. Note that Figure 5.14 indicates nothing about the absolute magnitude of the discharge peaks, but shows the peaks in the power (amplitude) or variation at the diurnal scale (frequency). Figure 5.7 shows that the absolute discharge peaks in 2003 and 2005, and in 1998 and 2001 (respectively) are similar in magnitude – but while 1998 and 2001 result in similar power peaks, 2005 peaks at nearly twice the power of 2003 (Figure 5.13). Figure 5.7 suggests that this may be because 2003 discharge levels drop off to zero very quickly after the peak, while 2005 sees nonzero discharge for a few weeks following the main peak.

Figure 5.14 also shows a gradual increase in power at the diurnal scale before the main peak, particularly in 2005. Since discharge measurements originate from the confluence of the whole Paakitsoq region's runoff in a single lake, this gradual increase in power need not arise from local changes at the specific location where the lake drainage occurred.

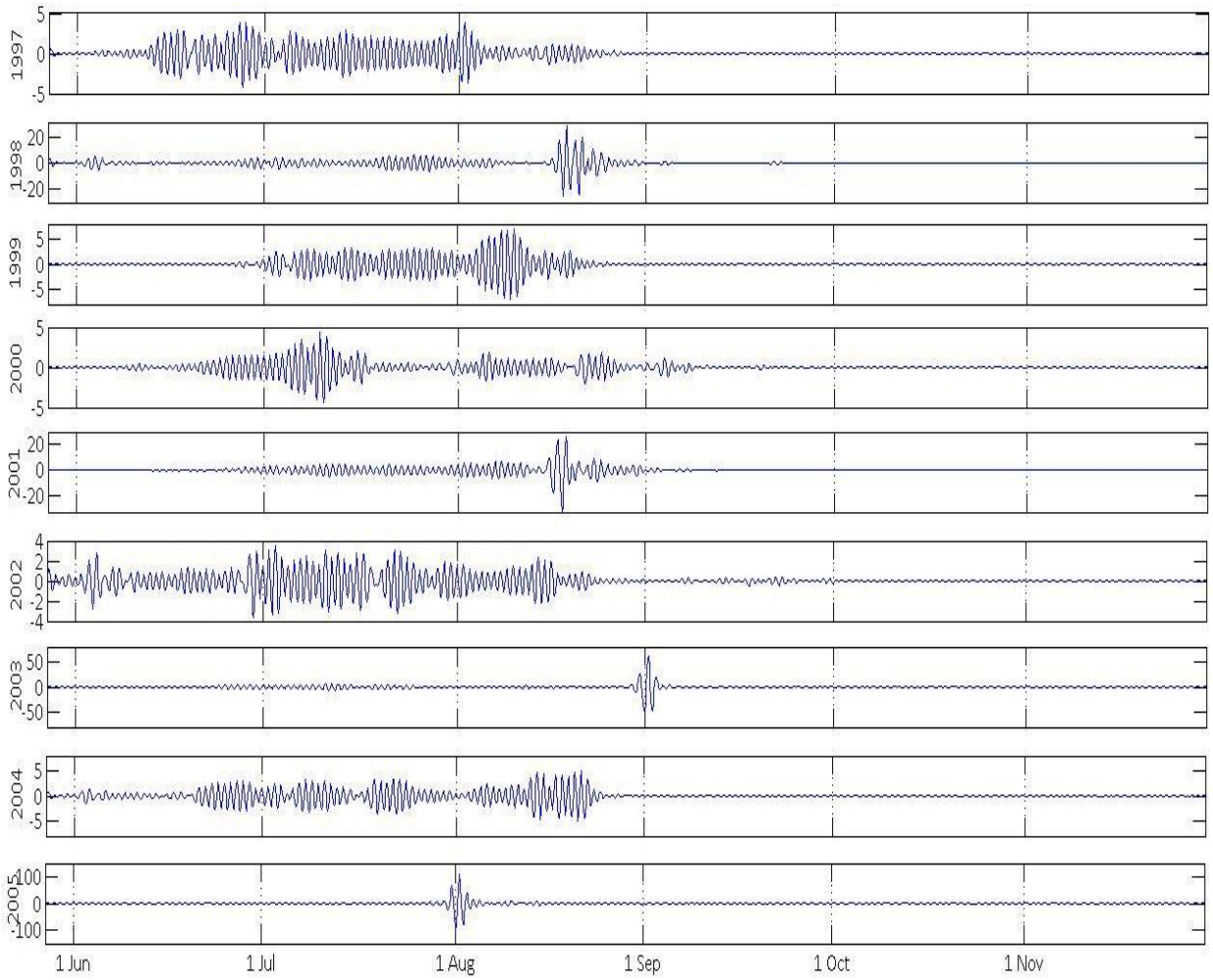

Figure 5.13: Sinusoids corresponding to scale 7 (24h) from every discharge CWT 1997-2005. Note the different y-axis scales for "flood years" (1998, 2001, 2003, 2005).

Overall, while the flood peaks observed in 1998, 2001, 2003 and 2005 have a significant impact on the evolution of drainage over time, they cannot explain all the variation in diurnal-scale power so that these years need to be considered in the context of the "non-flood years" as well.

5.2.3.2 All years

Figure 5.15 shows the same sinusoids as Figure 5.13, but they are all plotted on y-axes covering the same range (-5 to 5). The sinusoids from "flood years" therefore exceed their y-axis maxima/minima where the flood peaks occur (mid-Aug. 1998/2001; late Aug.-early Sep. 2003; early Aug. 2005), but diurnal-scale power variations at all other times are better represented and can be compared between "flood" and "non-flood years".

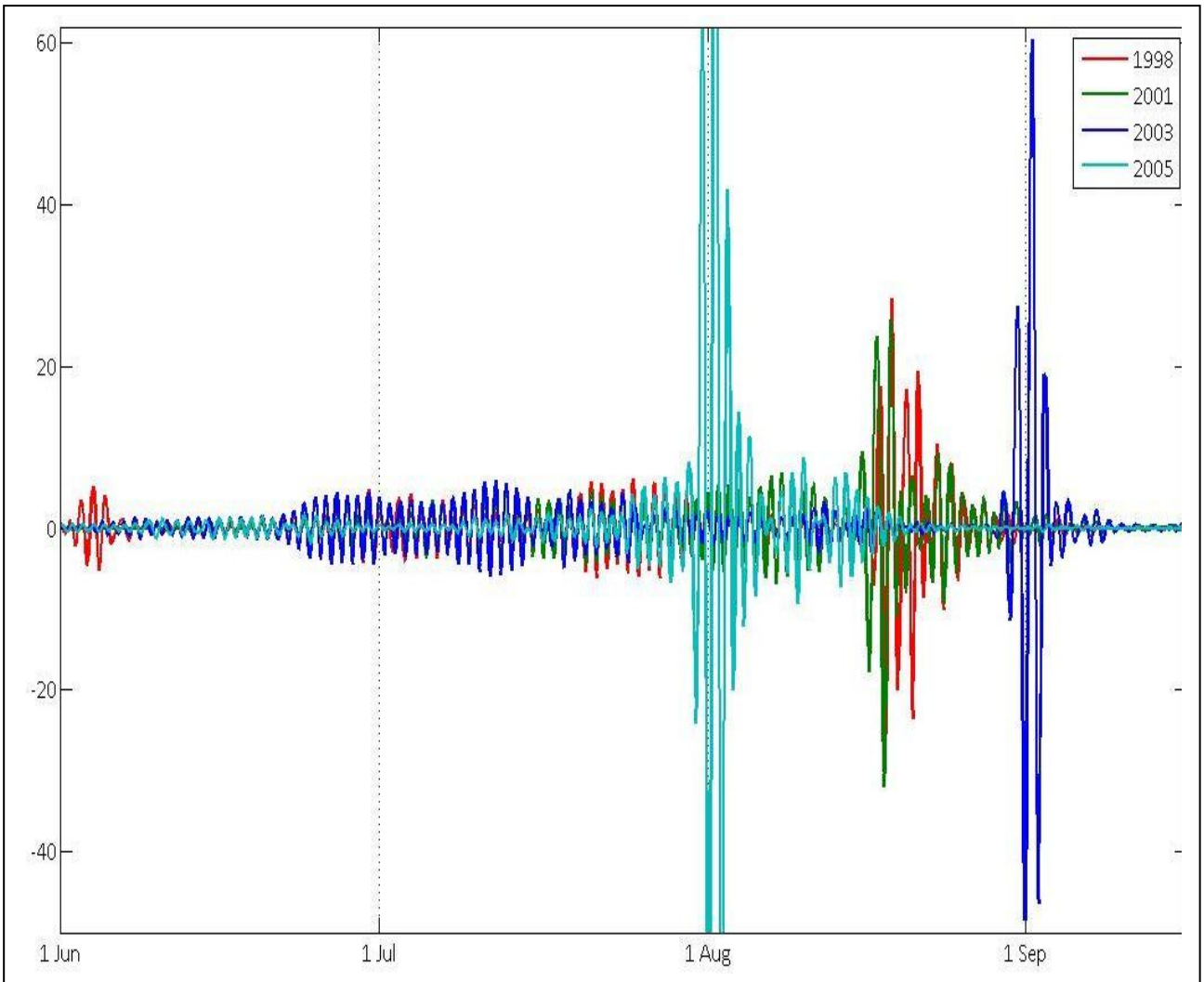

Figure 5.14: Discharge CWT Sinusoids corresponding to scale 7 (24h) for the „flood years" (1998, 2001, 2003, 2005). The 2005 curve overruns the y-axis which has been curtailed for better overall visibility.

Generally, “non-flood years” exhibit lower power in diurnal variability over the course of the melt season than “flood years”, a phenomenon which is not limited to the brief period when the peaks occur in the “flood years” (Figure 5.15). There is less sudden variation in “non-flood years”, and most changes in diurnal-scale power are gradual and small. 1999 is an exception in this respect, as this year exhibits more sustained higher power levels at the diurnal (and larger) scales than the other “non-flood years”. On the whole, however, “non-flood years” exhibit muted power fluctuations at the diurnal scale compared to “flood years”. This is exemplified by the 2004 signal, where four distinct periods of higher-power diurnal variability (but still low compared to most other years) can be distinguished, separated by brief interludes of near-zero power.

Figure 5.15 also shows that with the exception of 2005, all “flood years” have sustained periods of relatively high-power diurnal variability before the peak occurs. 1998, 2001 and 2003 all have several local maxima before their extreme maxima which may represent smaller and/or more gradual lake drainage events affecting only small parts of the catchment, or may be caused by co-variation with AT or NR (Section 5.3). While all years exhibit such local maxima, average power during “flood years”, even excluding the extreme maxima, is higher than the average power during “non-flood years”.

Overall, the period of high-power diurnal variation, defined here as power levels exceeding +/-1, varies from year to year and lasts between 9 and 12 weeks. 1999 is an exception with a very short high-power period: while power increases gradually over the course of June in most other years, diurnal variation only begins to exhibit nonzero power in July 1999, and does so for only 7 weeks.

It is also worth noting larger-scale variability (<7) up to scales corresponding to frequencies of 48h, which in “non-flood years” tend to exhibit high power at the same time as diurnal-scale variability does. Given the gradual changes in diurnal-scale power observed during “non-flood years”, it is unlikely that this is simply due to a sudden change in absolute discharge values such as the ones observed in “flood years” (which, as noted above,

produce high power across the entire spectrum). A shift in weather may cause a rise in the power of larger-scale variation if it brings about a sustained change in discharge.

This analysis of discharge CWT highlights that the melt season at Paakitsoq is by no means homogenous within or between years. While it is difficult to draw firm conclusions as to the exact causes of certain peaks in diurnal power due to the combination of discharge from several proglacial sources, it is clear that overall discharge variability is not consistent over the years, in part due to the complex interplay of meteorological and glaciological/hydrological factors.

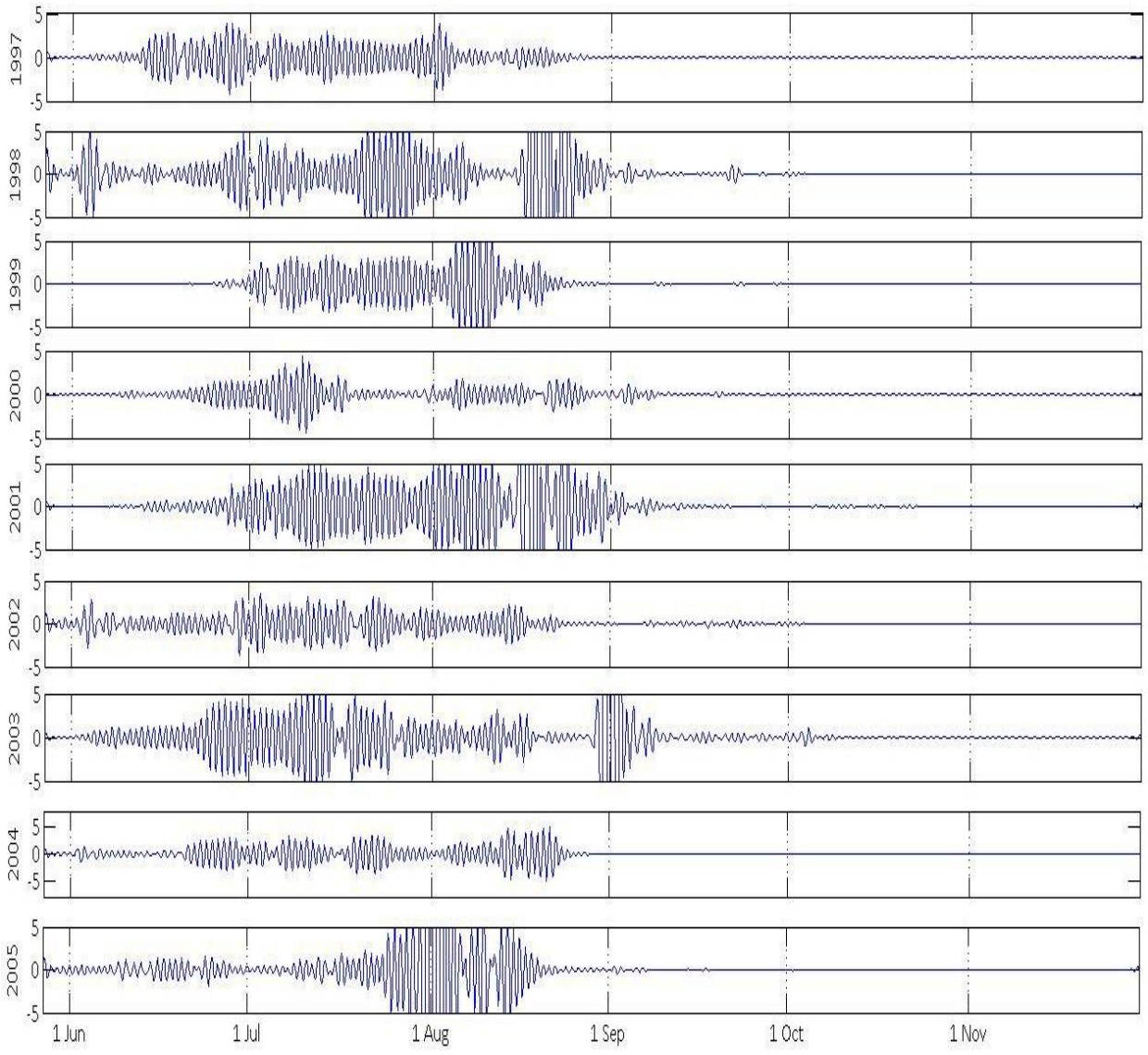

Figure 5.15: Sinusoids corresponding to scale 7 (24h) from every discharge CWT 1997-2005. All y-axes are identical for comparison of power levels throughout the melt season between "non-flood" and "flood years".

5.2.4 Interpretation of CWT Results

Midnight sun occurs in the Paakitsoq area from mid-May to late July, with midnight twilight for 2-3 weeks both before and after that period (Figure 5.16; measured at Ilulissat, 69.21°N 51.11°W). The diurnal fluctuations in both AT and NR which arise from the day-night cycle in lower latitudes are therefore expected to be dampened during most of summer. However, despite the occurrence of midnight sun, high-power diurnal-scale variability is present in both AT and NR throughout summer and is particularly prevalent in NR. The angle of incident radiation changes even when the sun does not set for several weeks, and net shortwave radiation is linearly related to the cosine of the solar zenith angle (Cess et al., 1992). Incoming solar radiation therefore still varies considerably over the course of 24h, producing diurnal variability in NR. Average monthly irradiation (in kWh m^{-2} day^{-1}; source: http://www.gaisma.com) for Ilulissat peaks in June and July at 5.72 and 5.42, respectively. It then drops to 3.65 in August and 2.07 in September, implying that the differential between daytime and nighttime NR will also decline, lowering the power of diurnal-scale variability.

High-power variation on timescales of 2-3 days, which corresponds to brief changes in weather patterns, is almost completely absent in summer for both AT and NR. This is

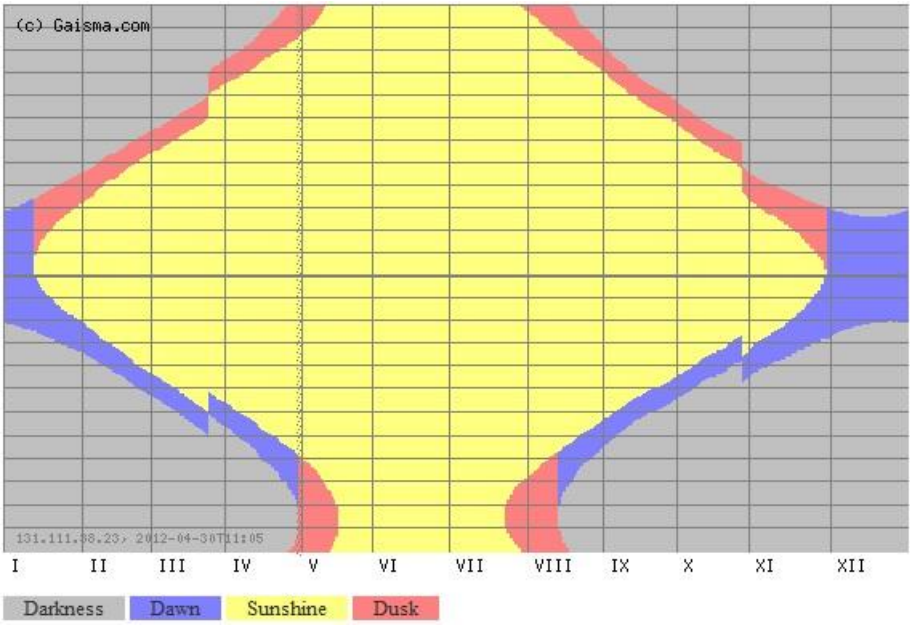

Figure 5.16: Times of midnight sun in Ilulissat: yellow represents sunshine, with hours of the day on the y-axis and months on the x-axis. Source: http://www.gaisma.com/en/location/ilulissat.html

probably largely due to relatively consistent summer weather patterns over the GrIS, with increasing variability in weather explaining the rise in the power of larger-scale (>7) variability in autumn.

The presence or absence of a layer of snow at the JAR1 AWS may also affect NR values. Since the albedo of ice is significantly lower than that of snow (e.g. Cuffey and Paterson, 2010), observed NR patterns may change once the snowline retreats past JAR1. This might helps explain the sudden onset and cessation of high-power diurnal-scale variability in NR – while a snowpack is present much more incoming radiation will be reflected, lowering the diurnal contrast between nighttime and daytime NR.

Diurnal-scale variability in discharge exhibits interesting patterns, including the fact that power at this scale tends to be higher for longer time periods during “flood years”. High diurnal-scale variation means a return to lower levels during nighttime, in which case the subglacial drainage system would have longer time every night to contract and become less efficient again before the next day’s meltwater input. This would allow diurnal fluctuations to remain high until meltwater inputs become great enough to bring about the shift to an efficient drainage system. Indeed, diurnal-scale power following the peaks in “flood years” tends to be far lower than before the peaks. This suggests a subglacial drainage event which might overstep a threshold meltwater quantity required to produce a channelized system, rather than a proglacial jökulhlaup which would not affect the subglacial system.

Discharge data are collected from the confluence of all the proglacial streams running off west from the Paakitsoq area (upglacier areas, at altitudes greater than Swiss Camp at ~1150m, drain south towards Jakobshavn Isbrae; Mottram et al., 2009). This means that spatial resolution is lost and it is unclear whether the meltwater inputs producing variability are localised or originate from across the catchment. However, Dorthe Petersen, of ASIAQ (2010; personal communication) notes that the outlet of Lake 326, one of the two lakes feeding Lake 187 where the discharge monitoring station is situated (Figure 4.2), has changed position as the outlet glacier feeding it has retreated. A significant water level

lowering was reported subsequently, with water draining into Lake 187 under the ice. The discharge peaks in the "flood years" might be due to jökulhlaups produced by this new drainage pathway, and may highlight some regularity in the filling and drainage of Lake 187: the flood peaks occur every other year, with exception of 2001 when three years have passed since the last peak (1998). This may be due to low discharge in both 1999 and 2000 (Figure 5.10), which means that the lake filled over a longer time period.

The univariate analysis of meteorological and discharge time series with the CWT highlights the changes in the power of the signals' variability over both time and scale, providing a useful insight into the evolution of these variables. Indeed, while diurnal-scale fluctuations do occur over the course of a melt season in AT, NR and Q, the patterns of these fluctuations vary both within and between the time series.

5.3 Multivariate Wavelet Analysis

While the CWT of individual meteorological and discharge signals are instructive as to the timings of the power of variability at different scales, the real value of wavelet analysis to the understanding of the relationship between AT/NR and discharge lies in the possibility of examining them jointly. To this end, Appendix 5 shows the graphs for wavelet coherence, phase difference and average wavelet coherence per scale for AT and Q, one graph for each year 1997-2005. Appendix 6 shows the same for NR and Q.

A different toolbox was used to perform the multivariate wavelet analyses. Here, a scale of 8 corresponds to 24h frequencies, with 16 corresponding to 48h, 24 to 72h and 32 to 96h frequencies. For clarity these values are included on the relevant axes. Wavelet coherence takes on a value between 0 (no coherence) and 1 (perfect coherence), but all colours shown indicate statistically significant coherence at the 95% significance level; insignificant values are shown in white.

On all graphs, the x-axis (representing time) extends from 27th May, 09:00, to 16th October,

21:00 as times beyond these limits exhibit negligible variation in discharge. This improves the focus on times where more relevant variation in both time series occurs.

The variable x here always refers to AT/NR while y is always discharge.

5.3.1 Discharge and Air Temperature

5.3.1.1 Wavelet Coherence

Wavelet coherence between AT and Q (Appendix 5) exhibits different patterns on different scales. Daily scales (8) are dominated by short "bursts" of very high coherence (red) which tend to last between a few days and a week. They coincide with high coherence at shorter scales, suggesting that the two series change together on these scales and at these times. 2001 is an exception to this pattern as very high coherence occurs at the diurnal scale consistently from late June to early August. Conversely, 2005 has only a very short episode of high coherence at the diurnal scale which lasts just a few days at the end of July/beginning of August. The rest of the 2005 summer has no statistically significant coherence between AT and Q, in stark contrast to all other years.

Statistically significant wavelet coherence on the 2-day scale (16) is rare and tends to be near zero (blue) when it does occur. 2000 is one exception to this, with high levels of coherence at the two-day scale (and just above) in the first half of July and during the third week of August. It is worth noting that the 2000 signal contains no data for AT from September onwards, which causes the blocky artefacts in the WCO plot for that year. 2002 and 2005 also have brief periods (<1 week) of high coherence at the 2-day scale, both in early October. This is a time when melt is unlikely to still be widespread on the ice sheet, so it may be related to discharge from meltwater reservoirs not previously accessed, or due to precipitation events.

Most years in the observation period exhibit a degree of statistically significant wavelet

coherence on the 3- and 4-day scales. In 1997 coherence is strong on the 4-day scale from late May until late June, at which point a switch occurs to high coherence on the 3-day scale; this continues until mid-August. The rest of the 1997 melt season sees low but significant coherence at both these scales. Conversely, 1998, 2000, 2002 and 2004 have high coherence spanning all the 3- and 4-day scales for a prolonged time period from late May to mid-September (slightly shorter for 1998). 2000 in particular exhibits extremely high coherence (near 1) at these scales throughout the summer, although data beyond September is meaningless due to the lack of AT data for this year. Finally, 1999, 2003 and 2005 have strong coherence at the 4-day scale only and predominantly in summer rather than autumn. 2001, meanwhile, only has weak significant wavelet coherence at these longer timescales.

5.3.1.2 Phase Difference

There are several trends apparent in the phase difference diagrams from the entire observation period. Generally, the phase difference increases from zero (i.e. moves out of perfect phase, with x leading) over the first half of summer until early to mid-July. Brief episodes of 1-3 days of the series moving back into phase do occur during this period, however, such as in late June/early July 1999 and mid-July 2002. Generally, phase differences then tend to stay positive until mid- to late August, indicating that discharge lags AT during midsummer, although brief episodes (no longer than two days) of zero or slightly negative phase difference do occur in all years.

In autumn, the phase difference tends to move towards zero in all years and vary between small positive and negative values. Since a negative phase difference implies that AT and Q are out of phase with AT lagging behind Q, this can only be interpreted as a breakdown of a causal link that may exist between the two variables. Indeed, this drop in the phase difference generally coincides with the timing of discharge returning to near-zero winter levels.

2001 is an unusual year in terms of its phase difference pattern as it is consistently positive from late June until mid-August, without any of the brief episodes of zero/negative phase difference mentioned above. This period of a clear, consistent lag of discharge behind AT coincides with the period of very high diurnal-scale wavelet coherence mentioned in Section 5.4.1.1– indeed, as coherence drops from the high levels sustained for 6 weeks the phase difference also drops back towards zero.

2004 exhibits similarly consistently positive phase difference from late June to the end of August, however in this year diurnal-scale wavelet coherence is not consistently high during this period. Unlike 2001, however, this year does have high levels of coherence throughout the summer on the 3- and 4-day scales, suggesting that even coherence at these large scales can contribute to a steady phase difference with AT leading.

Conversely, 2005 is the only year in which negative phase difference values dominate throughout most of summer. Apart from about two weeks in June and one week in July and August each, phase differences are negative in this summer apart from brief (<1 day) spikes of near-zero difference suggesting perfectly in-phase AT and Q.

5.3.1.3 Average Wavelet Coherence

Average wavelet coherence is a measure of wavelet coherence at one given scale but over the entire signal. That is, it represents the overall level of coherence at that given scale. For AT and Q it exhibits a repetitive pattern throughout most years of the observation period. With the exception of 2000, the highest average wavelet coherence occurs at the scale of 5, corresponding to a frequency of 15 hours. This is in accordance with the WCO graphs as the short peaks of high coherence (red) on the diurnal scale (8) and below are by far the most frequent occurrences of high coherence in every year except 2000. These short peaks are generally widest at the scale of 5. Average wavelet coherence tends to be between 0.6 and 0.8 (1.0 being the maximum possible value) at the scale of 5, and then drops off towards both larger and smaller scales.

In most years, average wavelet coherence decreases from its maximum at the scale of 5 very gradually to a minimum at or near the highest scales (34, corresponding to 102 hours). However, brief instances of higher average coherence do occur, such as in 1998, when high WCO levels at the 2-day scale in September and October produce high average coherence at this level.

2000 is the major exception to the pattern of gradually decreasing average wavelet coherence with increasing scale. In this year, average coherence reaches a minimum at a scale of 10 (30 hours) before increasing again to maximum at scales 30-32 (90-96 hours). This is in line with the WCO plot, which for this year shows very high wavelet coherence levels across the entire observation period for these scales. However, the lack of data from September onwards means that the average wavelet coherence graph may not be accurate in this year.

5.3.2 Discharge and Net Shortwave Radiation

5.3.2.1 Wavelet Coherence

The wavelet coherence between NR and Q (Appendix 6) exhibits a number of similarities as well as major differences to those between AT and Q. On diurnal and smaller scales (<8), WCO between NR and Q has “bursts” of higher coherence lasting between around two days and a week. These bursts, however, exhibit very high (red) coherence levels only rarely, such as in mid-August 1998, late August 1999 and early September 2002. In most cases coherence levels on the diurnal scale are of medium magnitude (yellow). As with the AT/Q WCO, diurnal-scale coherence between NR and Q also exhibits a much more consistently high level in 2001 from mid-June to mid-August; this is followed by a brief period of no significant coherence at this scale.

The diurnal-scale “bursts” of high coherence are only absent in 2003 and 2005, when the

WCO is almost never statistically significant at the diurnal scale for NR and Q. These two years have only a few episodes of low coherence throughout most of summer, while a few bursts of high coherence (similar to those observed at the diurnal scale in other years) occur in autumn (and late August for 2003).

The very high peaks in discharge in the "flood years" (1998, 2001, 2003, 2005), which produce artificially high power at all scales in their CWT graphs and "drown out" all other variation throughout the rest of the ablation seasons (Setion 5.2.3) do not have the same impact on the WCO graphs. In fact, these peaks produce no unusual features in the WCO graphs at all. The 1998 peak produces a short period of high coherence up to the diurnal scale for both AT/Q and NR/Q coherence, but this peak is no different from many others occurring during that year and is therefore unlikely to be caused by the large peak in discharge. The peaks in the other years do not even produce such high levels of coherence (red); 2005 is slightly unusual in that the flood peak produces a brief period of statistically significant diurnal-scale coherence between NR and Q, while coherence between these two variables at that scale in that year is mostly insignificant. This is unsurprising as these extreme peaks are unlikely to be caused by peaks of similar magnitude in AT or NR; their cause is internal – most likely a jökulhlaup from a marginal or subglacial lake.

On the 2-day scale, WCO between NR and Q is rarely statistically significant and if so, it is usually low (blue). Medium coherence (green/yellow) occurs at this scale in mid-August 1999 and late August 2005, and in several years (1997, 2000, 2004, 2005) at scales between two and three days (17-23).

It is on the longer timescales of >3 days (>24) that the main difference between AT and NR with respect to their wavelet coherence with discharge becomes apparent. WCO between NR and Q is overwhelmingly very strong (red) throughout summer and autumn in all years, although 2001 has a "gap" of no significant coherence at scales between 27 and 31, with coherence only becoming high at scales greater than 31.

5.3.2.2 Phase Difference

The phase difference between NR and Q is generally closer to zero than that between AT and Q, although longer-term trends are still discernible. In most years, the phase difference is already above zero (i.e. NR leading) at the beginning of the observation period, or increases soon after.

In about half the years of the observation period (1998, 2000-2003), the phase difference between NR and Q remains positive throughout most of the summer, with only occasional dips back to zero and into negative numbers (which imply that NR lags Q). In these years, phase difference reverts to zero values only in late September, with Q therefore lagging behind NR for some time into autumn when discharge values are already beginning to drop towards winter levels.

Conversely, the remaining years (1997, 1999, 2004, 2005) have a far less consistently positive phase difference between NR and Q. 1999, in fact, exhibits oscillating phase difference which rises and reverts to zero (and just below) roughly every four weeks throughout summer and early autumn. In 2005, phase difference is almost consistently negative between NR and Q, suggesting that causal links may be absent in this year (since Q leading NR makes no sense from a meteorological viewpoint). Phase difference also reverts to zero or negative values significantly earlier than in the other years, generally during August rather than September.

On the whole, a general pattern of Q lagging NR persists for early and midsummer in most years and tends to break down in late summer or early autumn. It is also worth noting that sharp negative peaks in phase difference often coincide with brief phases of no statistically significant wavelet coherence between NR and Q (e.g. early June 2004), although this is not always the case (e.g. late June 2001) so may be coincidental.

5.3.2.3 Average Wavelet Coherence

The patterns of average wavelet coherence between AT/NR and Q arise mostly from the patterns observed in the WCO plots and the phase differences. As for AT and Q, average wavelet coherence between NR and Q has a local maximum at a scale of 5 (15h) and drops slightly towards the diurnal scale (8).

The high levels of NR/Q coherence observed in Section 5.4.2.1 for timescales of 72h and greater (>24) mean that average wavelet coherence between NR and Q peaks at these high scales. Average coherence tends to reach a minimum either on scales 12-14 (36-42h; in 2000, 2002 and 2004), on scales 18-21 (54-63h; in 1999 and 2005) or a dual minimum in both these ranges (in 1997, 1998, 2001 and 2003).

The global maximum, then, is reached around the top end of scales, between 32 and 34 (96-102h). Some years, however, exhibit a drop in average coherence at the 4-day scale (32), in particular 1998 and 2001.

2003 is an unusual year in terms of its average coherence in that its global maximum is at the scale of 5 (15h), and in that coherence remains relatively high on all scales; fluctuations are small and average coherence levels at the 1-, 2-, 3- and 4-day scales are all between 0.45 and 0.6. This is unexpected as 2003 is also one of the years with relatively long periods of no statistically significant coherence at most levels.

Average wavelet coherence between NR and Q is slightly less variable than between AT and Q more generally, with levels below 0.4 only achieved rarely (particularly in 1999 and 2000).

5.3.3 Interpretation

The consistent presence of diurnal-scale coherence between AT and Q as well as NR and Q,

along with the concentration of this coherence at smaller scales (higher, subdaily frequencies) suggests that AT and NR both have a significant impact on discharge on a daily and subdaily basis. This connection between rising/falling AT and NR and corresponding increases/decreases in Q at frequencies up to 24h throughout most of summer is expected from numerous previous observations.

The diurnal-scale relationship between AT/NR and Q is not unchanging, however: there are gaps of up to several days between periods ("bursts") of high coherence in all years. This is probably due to changes in factors not actively considered in this study which affect the relationship between AT/NR and Q:

1. The supraglacial and subglacial routing of water can change over time, producing temporal runoff patterns different to the surface meltwater input patterns caused by variations in AT/NR. This includes the gradual thinning and migration upglacier of the snowpack which acts as a meltwater reservoir and slows its movement towards the ice-sheet margin (and facilitates the formation of superimposed ice, which further complicates runoff patterns; Wang et al., 2007). Another important factor is the gradual evolution of the drainage system from an inefficient, cavity-based system to a hydraulically efficient, channelized systems (Schoof, 2010; Sundal et al., 2011). Both these processes are spatially and temporally heterogenous and generally occur later the greater the distance from the margin, meaning that AT/NR patterns are not reflected exactly in Q patterns at lake 187. While some consistency is given by the fact that some moulins and englacial drainage features do persist over several years, and even some surface lakes re-form year after year in the same location, but this applies to only a minority of drainage features (Catania and Neumann, 2010).
2. Over the course of the summer, the area in which melt occurs also changes, gradually increasing upglacier (Wang et al., 2007). All other factors assumed equal this means a longer lag time between the occurrence of melt (driven by AT/NR) and its registration as discharge at the gauging station.

3. Other components of the surface energy balance, besides shortwave radiation, may change on short timescales. Precipitation contributes (minimally) to the surface energy balance, as do turbulent sensible and latent heat fluxes which are not considered here.

These three factors combined can make for significant variability in discharge above and beyond that produced by diurnal fluctuations in AT/NR, explaining why WCO between these two is not high consistently throughout the ablation season.

Larger-scale coherence levels may reflect trends which occur over 2-4 days rather than throughout the entire ablation season. This may reflect changes in weather patterns which can occur over the course of a few days. Generally, coherence at these large scales tends to be higher in summer than in autumn, suggesting that summer fluctuations in AT or NR at these timescales are well reflected by discharge patterns. The greater consistency of coherence at these scales suggests that the small-scale inconsistencies between AT/NR and Q which are caused by subglacial routing and melt area changes (see above) may be smoothed over. It is empirically possible that this consistency in WCO levels improves on even larger scales which were not considered in order to retain fine resolution of the smaller scales.

Despite more consistent WCO levels at larger scales (<16, or <2 days) even these relationships between AT/NR and Q do change over time. While short-term coherence can change very suddenly, though, larger-scale WCO levels tend to change more gradually. This suggests that sudden disturbances such as lake drainage events or outburst floods are unlikely to cause these changes and that they are driven by similarly gradual changes in AT/NR. There is also a possible hydrological explanation. As has been noted, the drainage system evolves over time and cavity-based systems develop into channelized ones. There is therefore a possibility of meltwater undergoing temporary local subglacial storage as parts of the drainage system are temporarily "cut off" from the remaining system, gradually changing the relationship between AT/NR and Q. This is likely to be a local effect

so that the impact on total discharge from the Paakitsoq area, as measured at Lake 187, is small, but noticeable.

The phase differences exhibited by the AT/Q and NR/Q relationships highlight the gradual evolution of these relationships over the course of the melt season. Positive and zero values are worth considering while negative values are taken to be an artefact of the method applied: these values imply that AT/NR lags behind discharge, which is not a meteorologically or glaciologically realistic scenario.

The evolution phase difference between AT and Q over the course of the melt season generally involves an increase in early summer, coinciding with a period when melt is likely to occur in the lowest regions of the GrIS, close to the margin and the monitoring station. This means that phase differences will be increasing from near zero make sense as the water has to cover small distances which gradually increase as average temperatures increase. Furthermore, as areas further upglacier begin to melt there will be increases in snowpack thickness and persistence as average temperatures drop. Since snow acts as a reservoir and slows down drainage until it reaches saturation, this will contribute to increasing lag times.

The increase in melt area and distance from the ice-sheet margin may also contribute to the lack of consistency in the phase difference once melting approaches its maximum extent: both external (meteorological) and internal (drainage system evolution, fracture propagation) factors as well as snowpack thickness vary spatially so that meltwater produced at a certain point in time at different points in the catchment may be registered by the monitoring station at different times.

It is also worth noting that during the midsummer period when phase differences are very variable, large peaks in the phase difference between AT and Q tend to coincide fairly well with “bursts” of high WCO at the diurnal scale. This may be the case when days with particularly high ablation rates occur but efficient drainage is not yet established so that lag

times peak as the high pressure produced by large meltwater quantities is not conducive to fast meltwater throughput through an inefficient cavity-based system (Bingham et al., 2005).

The decreasing trend in phase difference towards zero towards late summer (mid-August onwards) may be a product of the gradually disappearing snowpack and resulting shorter residence time of meltwater in/on the ice sheet. Furthermore, increasing parts of the subglacial drainage system become efficient and channelized. This means that both supraglacial and subglacial routing of water become more efficient, contributing to shorter lags between AT and Q in particular, but also NR and Q.

6. Summary and Conclusions

6.1 Summary

Wavelet methods are applied to metorological and discharge data from the Paakitsoq area of west Greenland to explore the changing relationship between AT/NR and Q continuously through both time and frequency. To the author's knowledge this is the first application of these methods to data from the GrIS. Originally developed in signal processing, wavelets have been used in a variety of hydrological applications including the hydrology of valley glaciers (Lafrenière and Sharp, 2003). This method has proven effective for the location of irregularly distributed features on a variety of scales throughout a time series (Smith et al., 1998).

The analysis of the time series is undertaken both individually, using the continuous wavelet transform (CWT), and jointly on AT and Q, and NR and Q using the complex wavelet coherence (WCO); phase difference and average wavelet coherence are additional outputs of the WCO calculation. These analyses show the power of variability continuously in both time and frequency, producing a three-dimensional analysis of variability within and co-variation between AT, NR and Q over the course of nine melt seasons (late May to late November 1997-2005 for univariate analysis, and late May to mid-October for multivariate analysis). This is a major advantage of wavelet analysis over conventional time series analysis, where data has to be divided up arbitrarily to study individual periods.

The results obtained in Section 5 show that the seasonal and interannual evolution of AT, NR and Q, as well as the evolution of the relationship between these variables, are clearly discernible from the uni- and multivariate analyses. The main findings are as follows:

- While diurnal fluctuations are evident from visual inspection of the signals for AT, NR and Q for part of the ablation season, the CWT plots show that variability at this

scale is not persistent throughout these series. High power diurnal-scale variability in NR tends to be more persistent than in AT during summer, while AT experiences greater variability than NR at larger scales during autumn. Diurnal-scale variability in meteorological variables is most likely due to changes in weather, including cloudiness, prevailing winds and precipitation. It is also controlled to a significant extent by the presence of midnight sun from late May until mid-August.

- Diurnal-scale variability in Q tends to be stronger in „flood years“ than in „non-flood years“. The lakes producing the floods may begin to drain slowly before the main peak, gradually releasing water into the drainage system This slow drainage would fluctuate diurnally in line with meltwater inputs into the system, possibly being forced by these inputs.
- Wavelet coherence highlights periods of statistically significant coherence between AT/NR and Q, distinguishing clearly between high and low coherence. On daily and subdaily timescales, coherence between AT/NR and Q tends to be high in „bursts“, i.e. over short time periods separated by periods of low or no significant coherence. This sudden change in coherence levels is due to factors not treated in this project, particularly weather patterns affecting components of the surface energy balance. Overall, diurnal-scale coherence is higher between AT/Q than between NR/Q.
- On longer timescales (2-4 days), WCO changes more gradually, probably reflecting the evolution of more gradually changing factors controlling discharge. This includes the changing area affected by melt, snowpack thickness and the supra-/en-/subglacial drainage system.
- Phase differences between AT/NR and Q show clear rising and falling trends at the beginning and end of summer, respectively. This is likely driven by the same factors as those affecting larger-scale (2-4 days) changes in WCO (above).

6.2 Limitations

Several factors influencing discharge (as measured at a proglacial gauging station) are not covered directly in this project. These include factors other than AT/NR in the surface

energy balance which affect surface meltwater generation, and factors which can modify the relationship between meltwater generation and its output at the ice margin (e.g. melt area and snowpack evolution, jökulhlaups from sub- or proglacial lakes or drainage system evolution). It is likely that some of the variability in the relationships between the variables studied here arises from changes in these parameters. This does not, however, diminish the finding that the relationship between AT and Q, and between NR and Q, develops and changes consistently throughout the ablation season. Furthermore, AT and NR are effective proxies for the surface energy balance and are useful in explaining part of the variation occurring in discharge. It unknown whether a time series of the entire surface energy balance would exhibit a different relationship with discharge and how this would be reflected in the multivariate wavelet analyses.

The positioning of the discharge gauging station at the confluence of meltwater from the entire Paakitsoq region made it impossible to provide intra-catchment spatial detail for the analysis as variations in discharge could have different spatial as well as causal (and, to an extent, temporal, as water melted at the same time in different areas would flow past the gauging station with different lag times) origins. This means that causes for certain unusual features in the time series, such as the peaks observed in the „flood years“ (1998, 2001, 2003, 2005) cannot be identified accurately.

An important shortcoming of the CWT are the artefacts produced on the plots by the extreme peaks in discharge which occur during the "flood years" (Section 5.2.3). These mean that these years are effectively lost to analysis because the high power levels on all scales shown at the time of the peak are an artefact and also mean that the actual variation at other times and scales is not displayed. However, the possibility of studying individual sinusoids corresponding to one scale alleviated this issue and meant that useful analysis could be drawn from the discharge CWT plots. The peaks occurring during the „flood years“ had no such effect on multivariate analysis (WCO), possibly because the change in discharge is so brief and extreme that it is not indicative of coherence with either AT or NR at any scale.

6.3 Conclusions

This project shows that wavelet methods are useful for the analysis of discharge from a glacial or ice-sheet setting due to their high resolution in both time and frequency space. The representation of time series in the frequency domain produces information that would not be available using conventional time-series analysis. Air temperature and net shortwave radiation both have an important influence on proglacial discharge, although numerous other factors which could not be covered here also play a role. As such, this project leaves plentiful scope for future research into glacial hydrology, and glacial processes more generally, using wavelet methods. This might include an analysis of the remaining components of the surface energy balance as drivers of melt and discharge, and a wavelet-based analysis of flow velocity itself.

References

Bibliography

Aguiar-Conraria, L. and Soares, J. (2011a) The continuous wavelet transform: A primer. Part of the ASToolbox, downloaded from http://sites.google.com/site/aguiarconraria/joanasoares-wavelets/ . Last accessed 29/05/2012.

Aguiar-Conraria, L. and Soares, J. (2011b) The continuous wavelet transform: moving beyond uni- and bivariate analysis. http://www3.eeg.uminho.pt/economia/nipe/docs/Actividades_Seminarios/2011/2011-11-16_LAConraria.pdf - last accessed 29/05/2012.

Ahlstrom, A. P. (2007), Previous glaciological activities related to hydropower at Paakitsoq, Ilulissat, West Greenland, *Tech. Rep. 25*, Geological Survey of Denmark and Greenland.

Ambaum, M.H.P., Hoskins, B.J., Stephenson, D.B. (2001) Arctic Oscillation or North Atlantic Oscillation?. *J. Climate*, **14**, 3495–3507.

Bamber, J.L., Alley, R.B., Joughin, I. (2007) Rapid response of modern day ice sheets to external forcing. Earth Plan. Sci. Lett., 257, 1-13.

Bartholomaus, T.C., Anderson, R.S., Anderson, S.P. (2008) Response of glacier basal motion to transient water storage. Nature Geoscience, 1, 33-37.

Bartholomew, I.D., Nienow, P., Mair, D., Hubbard, A., King, M.A., Sole, A. (2010) Seasonal evolution of subglacial drainage and acceleration in a Greenland outlet glacier. Nature Geoscience, 3, 408-411.

Bartholomew, I., P. Nienow, A. Sole, D. Mair, T. Cowton, S. Palmer, and J. Wadham (2011), Supraglacial forcing of subglacial drainage in the ablation zone of the Greenland ice sheet, Geophys. Res. Lett., 38, L08502, DOI:10.1029/2011GL047063.

Bartholomew, I.D., Nienow, P., Sole, A., Mair, D., Cowton, T., King, M.A., Palmer, S. (2011) Seasonal variations in Greenland Ice Sheet motion: Inland extent and behaviour at higher elevations. Earth and Planetary Science Letters, 307, 271-278.

Benn, D.I., Gulley, J., Luckman, A., Adamek, A., Glowacki, P.S. (2009) Englacial drainage systems formed by hydrologically driven crevasse propagation. J. Glaciol., 55 (191), 513-523.

Bingham, R.G., Nienow, P.W., Sharp, M.J. (2003) Intra-annual and intra-seasonal flow dynamics of a High Arctic polythermal valley glacier. Annals of Glaciology, 37 (1), 181-188.

Bingham, R.G., Nienow, P.W., Sharp, M.J., Boon, S. (2005) Subglacial drainage processes at a High Arctic polythermal valley glacier. Journal of Glaciology, 51 (172), 15-24.

Boon, S., and Sharp, M. (2003) The role of hydrologically-driven ice fracture in drainage system evolution on an Arctic glacier. Geophys. Res. Lett., 30(18), 1916, doi:10.1029/2003GL018034

Box, J.E. and Ski, K. (2007) Remote sounding of Greenland supraglacial melt lakes: implications for subglacial hydraulics. J. Glac., 53 (181), 257-265.

Box, J.E., and 8 others (2006) Greenland Ice Sheet Surface Mass Balance Variability (1988-2004) from Calibrated Polar MM5 Output. J. Climate, 19, 2873-2800.

Carmona, R., Hwang, W.-L., Torresani, B. (1998) Practical Time-Frequency Analysis: Gabor and Wavelet Transforms with an Implementation in S. Wavelet Analysis and its Applications, Volume 9. Elsevier.

Catania, G.A. and Neumann, T.A. (2010) Persistent englacial drainage features in the Greenland Ice Sheet. Geophys. Res. Lett., 37, L02501, DOI:10.1029/2009GL041108.

Cazelles, B., and 6 others (2008) Wavelet Analysis of Ecological Time Series. Oecologia, 156 (2), 287-304.

Christoffersen, P., Hambrey, M.J. (2006) Is the Greenland Ice Sheet in a state of collapse? Geology Today, 22 (3), 98-103.

Cuffey, K.M. and Paterson, W.S.B. (2010) The Physics of Glaciers. Elsevier.

Das, S.B., Joughin, I., Behn, M.D., Howat, I.M., King, M.A., Lizzaralde, D., Bhatia, M.P. (2008) Fracture Propagation to the Base of the Greenland Ice Sheet during Supraglacial Lake Drainage. Science, 320 (5877), 778-781.

Daubechies, I. (1994) Wavelets and other phase space localization methods. In: Proc. Int. Congress of Mathematicians (Zurich, 1994), Basel (SUI), 56-74.

Foufoula-Georgiou, E. and Kumar, P. (1994) Wavelet Analysis in Geophysics: An Introduction. In: Foufoula-Georgiou, E. and Kumar, P., Wavelets in Geophysics, Academic Press, London, 1-44.

Gregory, J.M., Huybrechts, P., Raper, S.C.B. (2004) Climatology: Threatened Loss of the Greenland Ice Sheet. Nature, 428, 616. doi:10.1038/428616a

Greuell, W. and Konzelmann, T. (1994) Numerical modelling of the energy balance and the englacial temperature of the Greenland Ice Sheet. Calculations for the ETH-Camp location (West Greenland, 1155 m a.s.l.). Global and Planetary Change, 9 (1-2), 91-114.

Grinsted, A., Moore, J.C., Jevrejeva, S. (2004) Application of the cross wavelet transform and wavelet coherence to geophysical time series. Nonlinear Processes in Geophysics, 11, 561-566.

Grossman, A. and Morlet, J. (1984) Decomposition of Hardy functions into square-integrable wavelets of constant shape. SIAM J. Math. Anal., 15, 723-736.

Gurnell, J.M., and Clark, M.J. (1992) Analysis and interpretation of patterns within and between hydroclimatological time series in an alpine glacier basin. Earth Surface Processes and Landforms, 17 (8), 821-839.

Hanna, E., Huybrechts, P. and 7 others (2008) Increased Runoff from Melt from the Greenland Ice Sheet: A Response to Global Warming. J. Climate, 21, 331-341.

Hanna, E., and 12 others (2011), Greenland Ice Sheet surface mass balance 1870 to 2010 based on Twentieth Century Reanalysis, and links with global climate forcing, J. Geophys. Res., 116, D24121, doi:10.1029/2011JD016387.

Hock, R. 2005. Glacier melt: a review of processes and their modelling. *Progress in Physical Geography,* 29**,** 362-391.

Hodgkins, R. (2001) Seasonal evolution of meltwater generation, storage and discharge at a non-temperatre glacier in Svalbard.

Hodson, A.J., Gurnell, A.M., Washington, R., Tranter, M., Clark, M.J., Hagen, J.O. (1998) Meteorological and runoff time-series characteristics in a small, high-Arctic glaciated basin, Svalbard. Hydrol. Proc., 12 (3), 509-526.

Hoffman, M.J., Catania, G.A., Neumann, T.A., Andrews, L.C., Rumrill, J.A. (in press) Links between acceleration, melting and supraglacial lake drainage of the western Greenland Ice Sheet. J. Geophys. Res.

Holland, D.M., Thomas, R.H., de Young, B., Ribergaard, M.H., Lyberth, B. (2008) ***A***cceleration of Jakobshavn Isbræ by warm subsurface ocean waters. Nature Geoscience, 1, 659-664.

Howat, I.M., Joughin, I., Scambos, T.A. (2007) Rapid Changes in Ice Discharge from Greenland Outler Glaciers. Science, 315, 1559-1561. DOI: 10.1126/science.1138478

Hudgins, L., Friehe, C.A., Mayer, M.E. (1993) Wavelet transforms and atmospheric turbulence. Physical Review Letters, 71 (20), 3279-3282.

Huybrechts, P., Gregory, J., Janssens, I., Wild, M. (2004) Modelling Antarctic and Greenland volume changes during the 20th and 21st centuries forced by GCM time slice integrations. Global and Planetary Change, 42, 83-105.

Janssens, I., and Huybrechts, P. (2000) The treatment of meltwater retention in mass-balance parameterizations of the Greenland ice sheet. *Annals of Glaciology, Vol 31, 2000,* 31**,** 133-140.

Jobard, S. and Dzikowski, M. (2006) Evolution of glacial flow and drainage during the ablation season. Journal of Hydrology, 330 (3-4), 663-671.

Joughin, I., Das, S.B., King, M.A., Smith, B.E., Howat, I.M., Moon, T. (2008) Seasonal Speedup Along the Western Flank of the Greenland Ice Sheet. Science, 320, 781-783.

Joughin, I., Smith, B.E., Howat, I.M., Scambos, T., Moon, T. (2010) Greenland flow variability from ice-sheet-wide velocity mapping. J. Glac., 56 (197), 415-430.

Kern-Hansen, C. (1988) Hydrological Background of a Glacier-Influenced Hydropower Station in Greenland. Nordic Hydrology, 19 (4), 269–280.

Kingsbury, N.G., Selesnick, I.W., Baraniuk, R.G. (2005) The Dual-Tree Complex Wavelet Transform. A coherent framework for multiscale signal and image processing. IEEE Signal Processing Magazine, November 2005, 123-151.

Krabill, W., and 12 others (2004), Greenland Ice Sheet: Increased coastal thinning, Geophys. Res. Lett., 31, L24402, doi:10.1029/2004GL021533.

Labat, D., Ababou, R., Mangin, A. (2000) Rainfall-runoff relations for karstic springs. Part I: Convolution and Spectral Analyses. J. Hydrol., 238 (3-4) 123-148.

Labat, D. (2005) Recent Advances in Wavelet Analysis. Part I: A Review of Concepts. Journal of Hydrology, 314, 275-288.

Lafreniere, M., and Sharp, M. (2003) Wavelet analysis of inter-annual variability in the runoff regimes of glacial and nival stream catchments, Bow Lake, Alberta. *Hydrological Processes,* 17**,** 1093-1118.

Lang, W.C. And Forinash, K. (1998) Time-frequency analysis with the continuous wavelet transform. Am. J. Phys., 66 (9), 794-797.

Lau, K.M. and Weng, H. (1995) Climate Signal Detection using Wavelet Transform: How to make a time series sing. Bull. Amer. Met. Soc., 76 (12), 2391-2402.

Lenz, O.K., Wilde, V., Riegel, W. (2011) Short-term fluctuations in vegetation and phytoplankton during the middle Eocene greenhouse climate: a 640-kyr record from the Messel oil shale (Germany). Int. J. Earth Sci., 100, 1851-1874. DOI:10.1007/s00531-010-0609-z

Little, S.A. (1994) Wavelet Analysis of Seafloor Bathymetry: An Example. In: Foufoula-Georgiou, E. and Kumar, P., Wavelets in Geophysics, Academic Press, London, 167-182.

Luthcke, S.B., Zwally, H.J. and 7 others (2006) Recent Greenland Ice Mass Loss by Drainage System from Satellite Gravity Observations. Science, 314, 1286-1290.

McMillan, M., Nienow, P., Shepherd, A., Benham, T., Sole, A. (2007) Seasonal evolution of supra-glacial lakes on the Greenland Ice Sheet. Earth and Planetary Science Letters, 262 (3-4). 484-492. DOI:10.1016/j.epsl.2007.08.002

Melesse, A., Abtew, W., Dessalegne, T., Wang, X. (2009) Low and high flow analyses and wavelet application for characterization of the Blue Nile River system. Hydrological Processes, 24, 241-252.

Mohlenkamp, M.J. and Pereyra, M.C. (2008) Wavelets, Their Friends, and What They Can Do for You. European Mathematical Society, ETH Zurich.

Moore, R.D., and Demuth, M.N. (2001) Mass balance and streamflow variability at Place Glacier, Canada, in relation to recent climate fluctuations. Hydrol. Proc., 15 (18), 3473-3486.

Mottram, R., and 7 others (2009) A new regional high-resolution map of basal and surface topography for the Greenland ice-sheet margin at Paakitsoq, West Greenland. Annals of Glaciology, 50 (51), 105-111.

Motyka, R.J., Fahnestock, M., Truffer, J., Mortensen, J., Rysgaard, S. (2011) Submarine melting of the Jakobshavn Isberae Floating Tongue and the Triggering of the Current Retreat. J. Geophys. Res. 116, F01007.

Nason, G.P. (2006) Wavelet Methods in Statistics with R. Springer, New York, NY.

Ogden, R.T. (1997) Essential Wavelets for Statistical Applications and Data Analysis. Birkhauser, Boston, MA.

Palmer, S., Shepherd, A., Nienow, P., Joughin, I. (2011) Seasonal speedup of the Greenland Ice Sheet linked to routing of surface water. Earth and Planetary Science Letters, 304, 3-4, 423-428.

Parizek, B.R. and Alley, R.B. (2004) Implications of increased Greenland surface melt under global-warming scenarios: ice-sheet simulations. Quat. Sci. Rev., 23, 1013-1027.

Pimentel, S., and Flowers, G.E. (2010) A numerical study of hydrologically driven glacier dynamics and subglacial flooding. Proc. R. Soc. A*, 467 (2126),* 537-558. DOI: 10.1098/rspa.2010.0211

Price, S.F., Payne, A.J., Catania, G.A., Neumann, T.A. (2008) Seasonal acceleration of inland ice via longitudinal coupling to marginal ice. J. Glac., 54 (185), 213-219.

Richards, K.S., Sharp, M., Arnold, N.S., and 7 others (1996) An integrated approach to modelling hydrology and water quality in glacierized catchments. Hydrol. Process., 10, 475-660.

Rignot, E. and Kanagaratnam, P. (2006) Changes in the Velocity Structure of the Greenland Ice Sheet. Science, 311, 986-991.

Rignot, E., I. Velicogna, M. R. van den Broeke, A. Monaghan, J. Lenaerts (2011) Acceleration of the contribution of the Greenland and Antarctic ice sheets to sea level rise, Geophys. Res. Lett., 38, L05503, DOI:10.1029/2011GL046583.

Robinson, A., Calov, R., Ganopolski, A. (2012) Multistability and critical thresholds of the Greenland ice sheet. Nature Climate Change, 2, 429-432. DOI: 10.1038/nclimate1449

Schoene, B.R. and Fiebig, J. (2009) Seasonality in the North Sea during the Allerod and Late Medieval Climate Optimum using bivalve sclerochronology. Int. J. Earth Sci., 98 (1), 83-98. DOI:10.1007/s00531-008-0363-7

Schoof, C. (2010) Ice-sheet acceleration driven by melt supply variability. Nature, 468, 803-806.

Schoof, C., and Hewitt, I. (2011) Ice speed-up patterns near subglacial channels. American Geophysical Union, Fall Meeting 2011.

Schuenemann, K.C., Cassano, J.J. (2010) Changes in synoptic weather patterns and Greenland precipitation in the 20th and 21st centuries: 2. Analysis of 21st century atmospheric changes using self-organizing maps. J. Geophys. Res., 115, D05108, DOI:10.1029/2009JD011706.

Selmes, N., Murray, T., James, T.D. (2011) Fast draining lakes on the Greenland Ice Sheet.

Geophys. Res. Lett., 38, L15501, DOI:10.1029/2011GL047872.

Serreze, M.C., Holland, M.M., Stroeve, J. (2007) Perspectives on the Arctic's shrinking Sea-ice cover. Science, 315, 1533-1536.

Shepherd, A. and Wingham, D., 2007. Recent sea-level contributions of the Antarctic and Greenland ice sheets. Science, 315, 1529– 1532.

Shepherd, A., Hubbard, A., Nienow, P., King, M., McMillan, M, Joughin, I. (2009) Greenland ice sheet motion coupled with daily melting in late summer. Geophys. Res. Lett., 36, L01501, DOI:10.1029/2008GL035758.

Smith, L.C., Turcotte, D.L., Isacks, B.L. (1998) Stream flow characterization and feature detection using a discrete wavelet transform. Hydrological Processes, 12, 233-249.

Sole, A., Payne, T., Bamber, J., Nienow, P, Krabill, W. (2008) Testing hypotheses of the cause of peripheral thinning of the Greenland Ice Sheet: is land-terminating ice thinning at anomalously high rates? The Cryosphere, 2, 205-218.

Sorensen, L.S. and 7 others (2011) Mass balance of the Greenland ice sheet (2003-2008) from ICESat data – the impact of interpolation, sampling and firn density. The Cryosphere, 5, 173-186, DOI:10.5194/tc-5-173-2011.

Steffen, K., J. E. Box, and W. Abdalati, 1996 "Greenland Climate Network: GC-Net", in Colbeck, S. C. Ed.CRREL 96-27 Special Report on Glaciers, Ice Sheets and Volcanoes, trib. to M. Meier, pp. 98-103.

Stein, M. (2005) Climate Conditions around Greenland – 2004. Northwest Atlantic Fisheries Organisation, Scientific Council Meeting (June 2005),

Stern, N. (2006) The Economics of Climate Change: The Stern Review. Cambridge University Press.

Sundal, A.V., Shepherd, A., Nienow, P., Hanna, E., Palmer, S., Huybrechts, P. (2011) Melt-induced speed-up of Greenland ice sheet offset by efficient subglacial drainage. Nature, 469, 521-524.

Thomsen, H., Thorning, L., Braithwaite, R. (1988) Glacier-hydrological conditions on the Inland Ice Northeast of Jakobshavn/Ilulissat, West Greenland. Grønlands Geologiske Undersøgelse. Rapport 138.

Torrence, C. and Compo, G.P. (1998) A Practical Guide to Wavelet Analysis. Bull. Amer. Meteor. Soc., 79, 61-78.

Truffer, M., Harrison, W.D., March, R.S. (2005) Record negative glacier balances and low velocities during the 2004 heatwave in Alaska, USA: implications for the interpretation of observations by Zwally and others in Greenland. J. Glac., 51 (175), 663-664.

van de Wal, R.S.W. and 6 others (2008) Large and Rapid Melt-Induced Velocity Changes in the Ablation Zone of the Greenland Ice Sheet. Science, 321, 111-114.

van der Ween, C.J. (1998) Fracture mechanics approach to penetration of surface crevasses on

glaciers. Cold Regions Science and Technology, 27, 31-47.

Walder, J.S. (1986) Hydraulics of Subglacial Cavities. J. Glac., 32 (112), 439-445.

Wang, L., Sharp, M., Rivard, B., Steffen, K. (2007), Melt season duration and ice layer formation on the Greenland ice sheet, 2000–2004, J. Geophys. Res., 112, F04013, doi:10.1029/2007JF000760.

Whitcher, B., Guttorp, P., Percival, D.B. (2000) Wavelet analysis of covariance with application to atmospheric time series. J. Geophys. Res.

Willis, I.C., Arnold, N.S., Brock, B.W. (2002) Effect of snowpack removal on energy balance, melt and runoff in a small supraglacial catchment. Hydrol. Proc., 16 (14), 2721-2749.

Zwally, H.J. and 5 others (2002) Surface Melt-Induced Acceleration of Greenland Ice-Sheet Flow. Science, 297, 218-223.

Online Sources

http://sites.google.com/site/aguiarconraria/joanasoares-wavelets/
http://users.rowan.edu/~polikar/WAVELETS/WTtutorial.html
http://www.gaisma.com/en/location/ilulissat.html

Software

Adobe Reader
Eviews 7.0
Google Earth
Matlab R2010b, 2011b
Microsoft Word & Excel 2003
Microsoft Word & Excel 2007

Appendices

Appendix 1: CWT Graphs for Air Temperature, 1997-2005

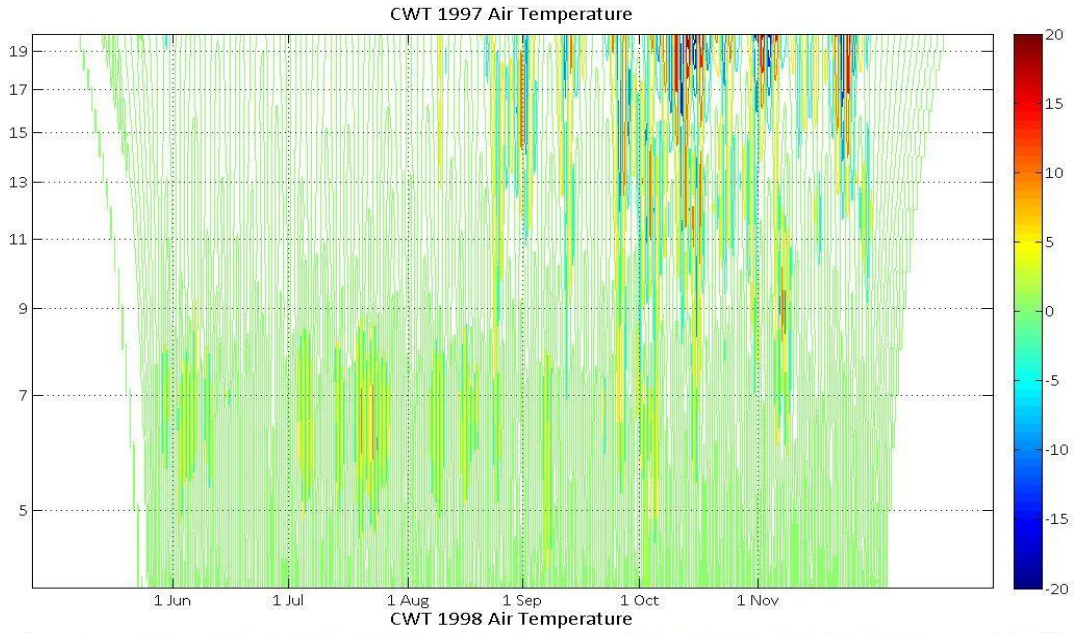

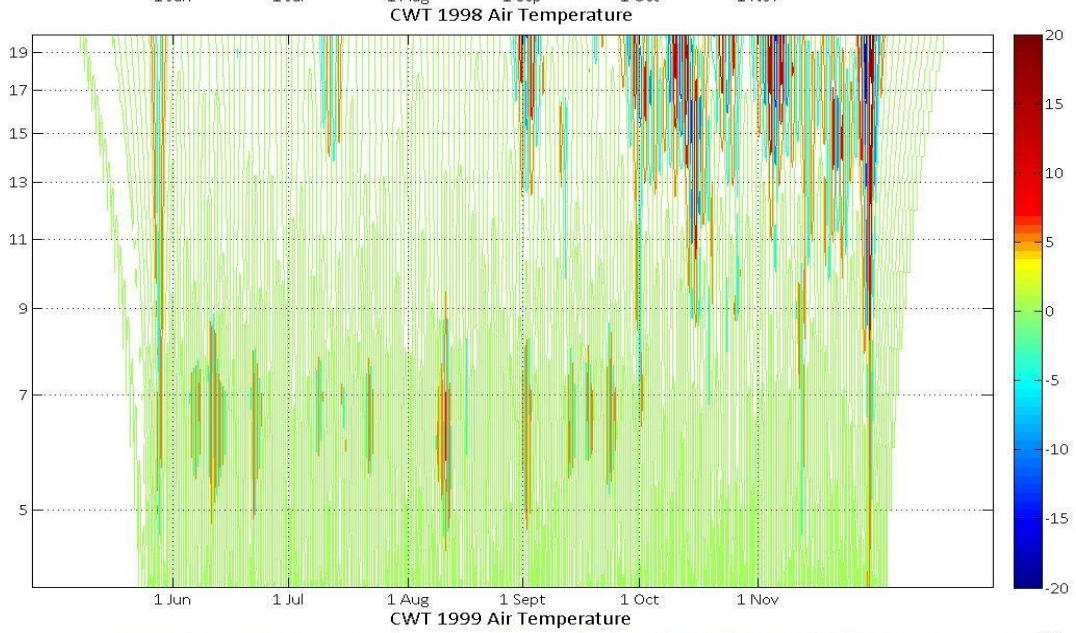

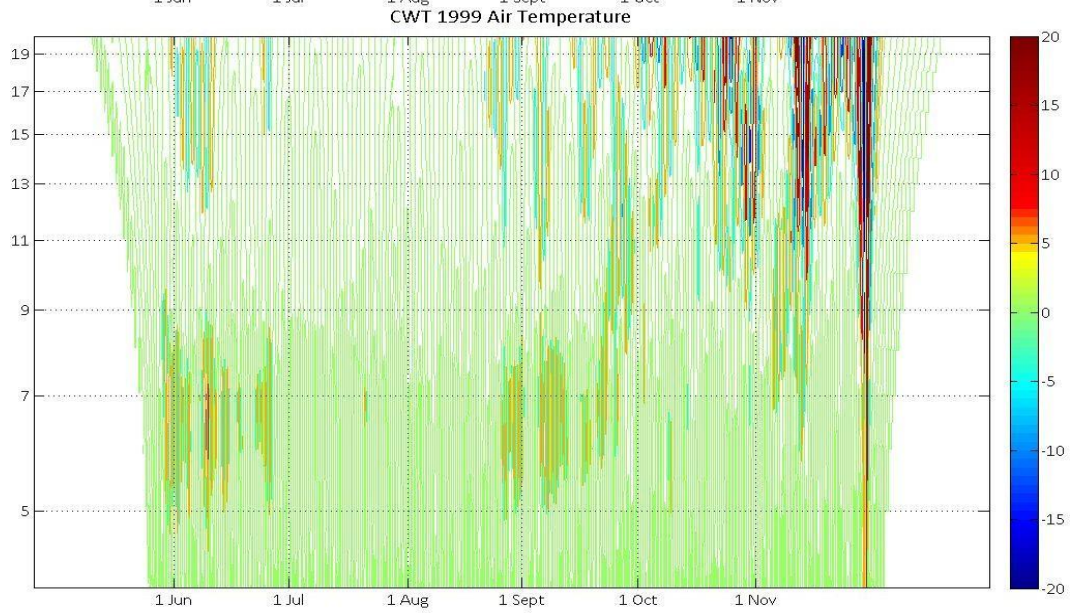

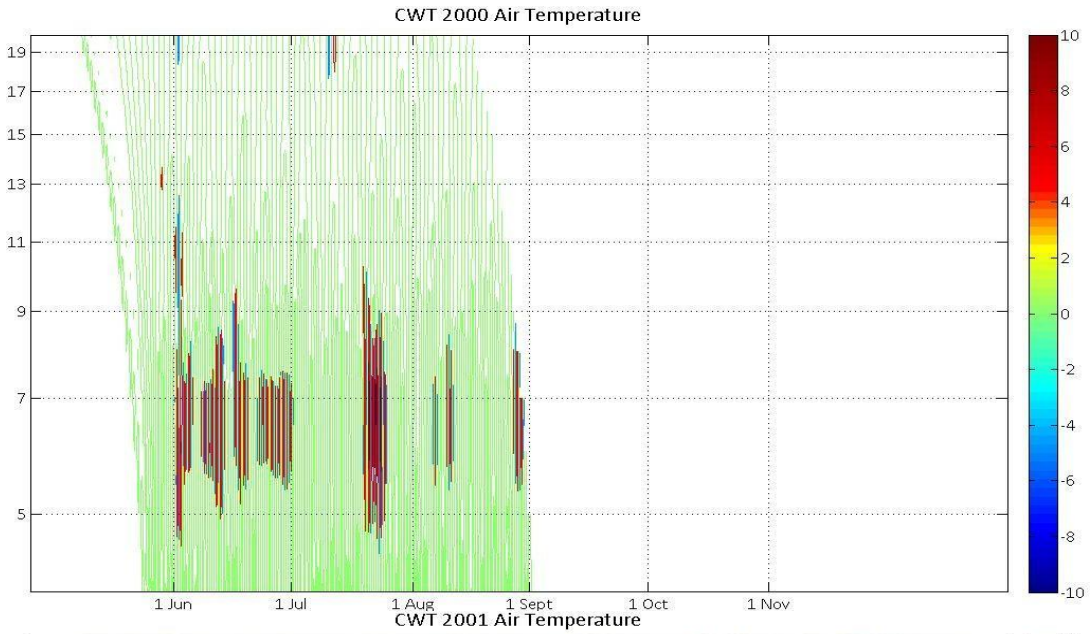
CWT 2000 Air Temperature
19
17
15
13
11
9
7
5
1 Jun
1 Jul
1 Aug
1 Sept
1 Oct
1 Nov
10
8
6
4
2
0
-2
-4
-6
-8
-10

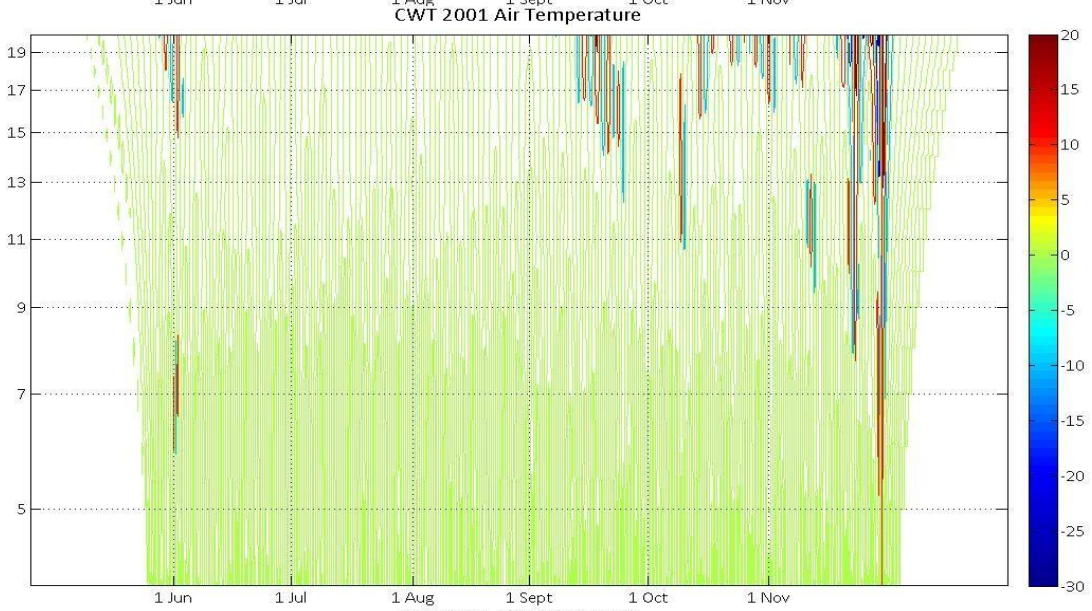
CWT 2001 Air Temperature
19
17
15
13
11
9
7
5
1 Jun
1 Jul
1 Aug
1 Sept
1 Oct
1 Nov
20
15
10
5
0
-5
-10
-15
-20
-25
-30

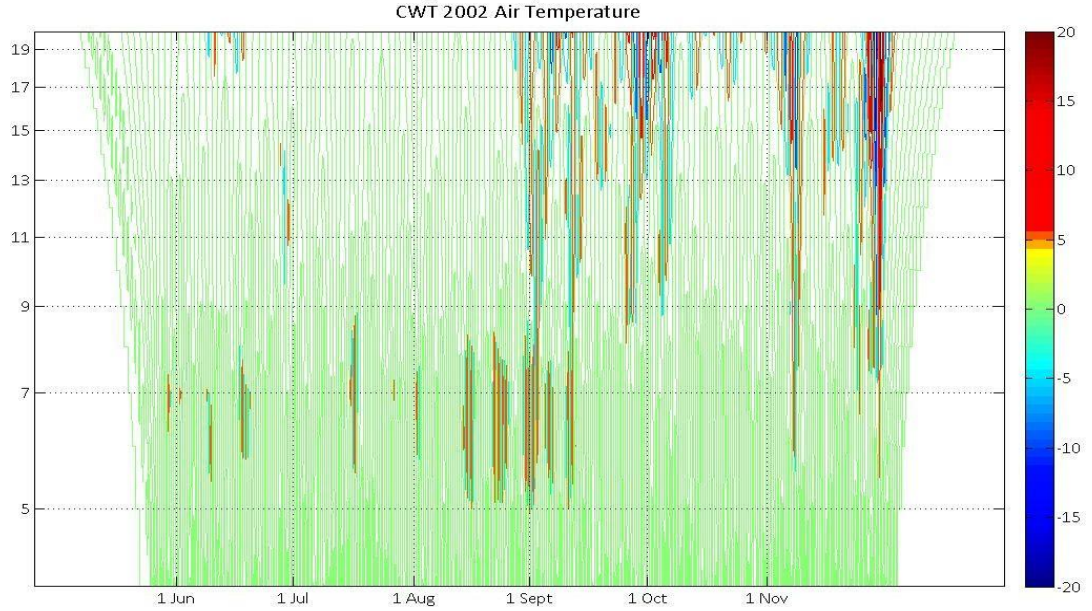
CWT 2002 Air Temperature
19
17
15
13
11
9
7
5
1 Jun
1 Jul
1 Aug
1 Sept
1 Oct
1 Nov
20
15
10
5
0
-5
-10
-15
-20

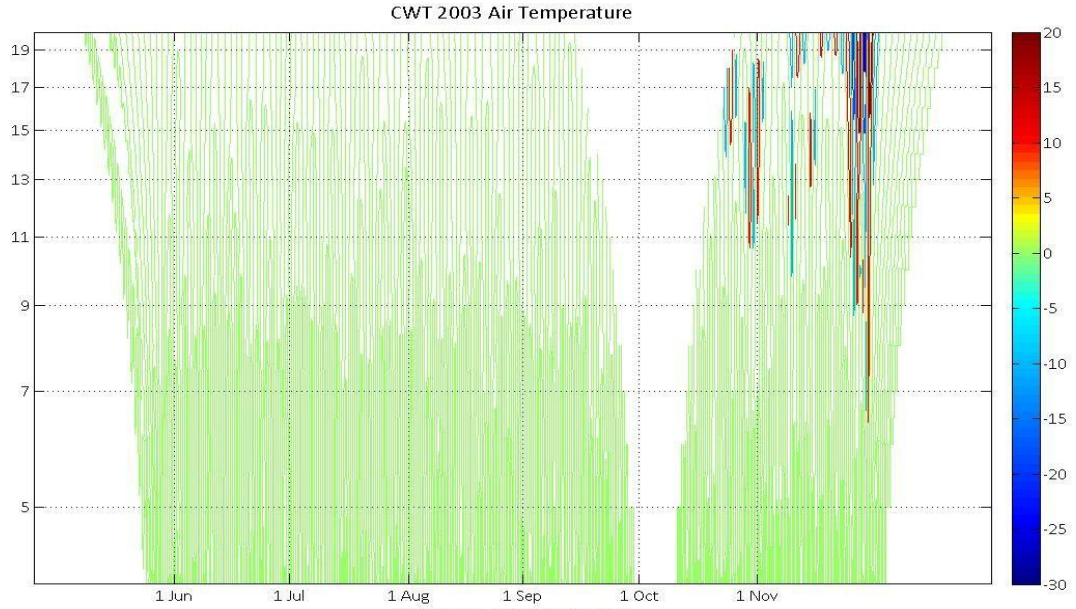
CWT 2003 Air Temperature
19
17
15
13
11
9
7
5
1 Jun
1 Jul
1 Aug
1 Sep
1 Oct
1 Nov
20
15
10
5
0
-5
-10
-15
-20
-25
-30

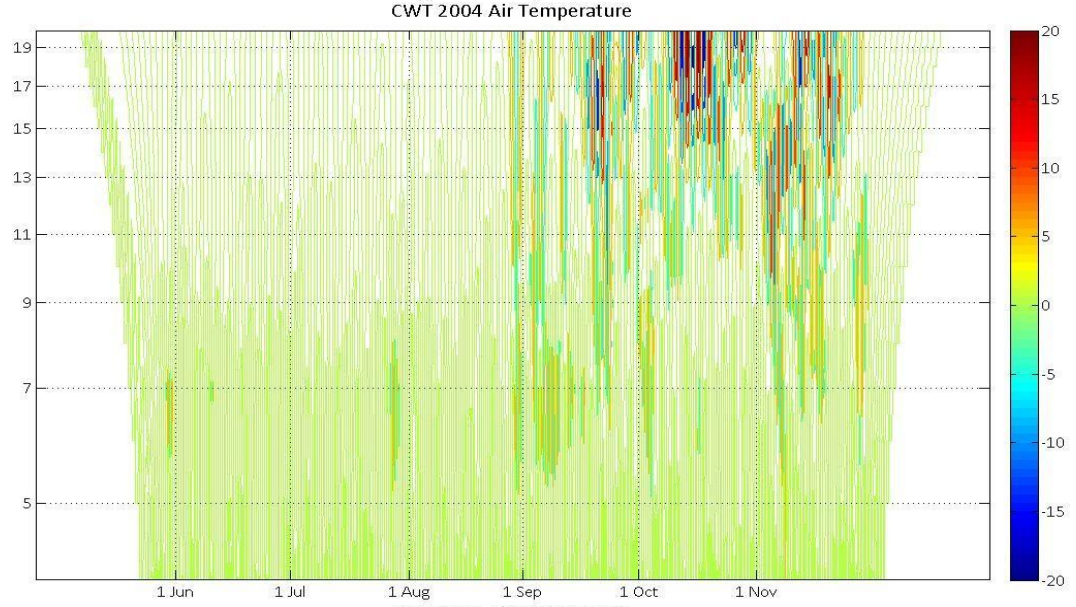
CWT 2004 Air Temperature
19
17
15
13
11
9
7
5
1 Jun
1 Jul
1 Aug
1 Sep
1 Oct
1 Nov
20
15
10
5
0
-5
-10
-15
-20

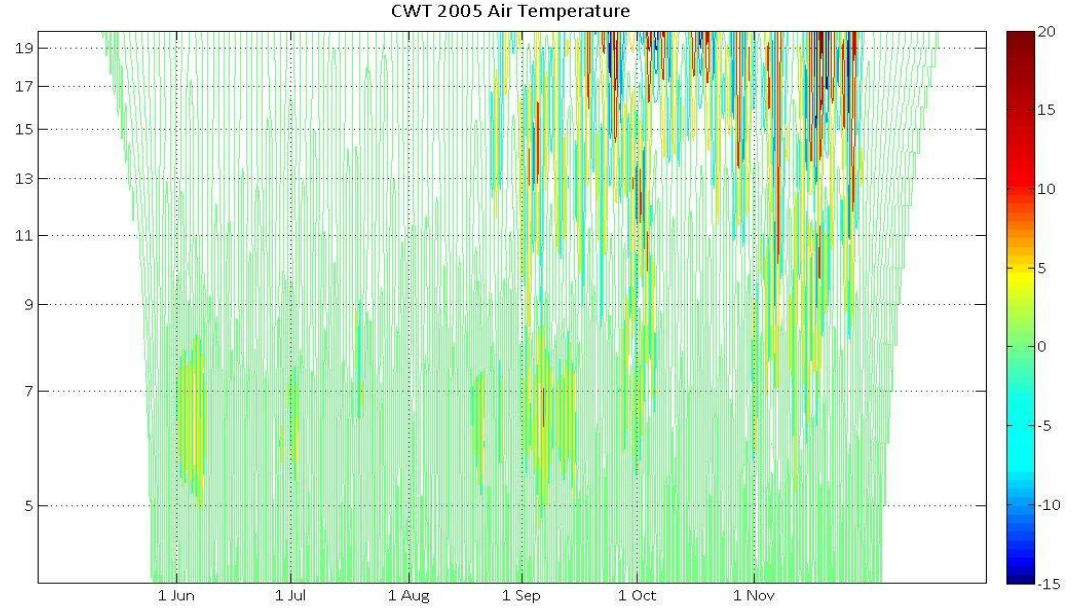
CWT 2005 Air Temperature
19
17
15
13
11
9
7
5
1 Jun
1 Jul
1 Aug
1 Sep
1 Oct
1 Nov
20
15
10
5
0
-5
-10
-15

Appendix 2: Air Temperature Series and Corresponding Diurnal-Scale CWT Sinusoids

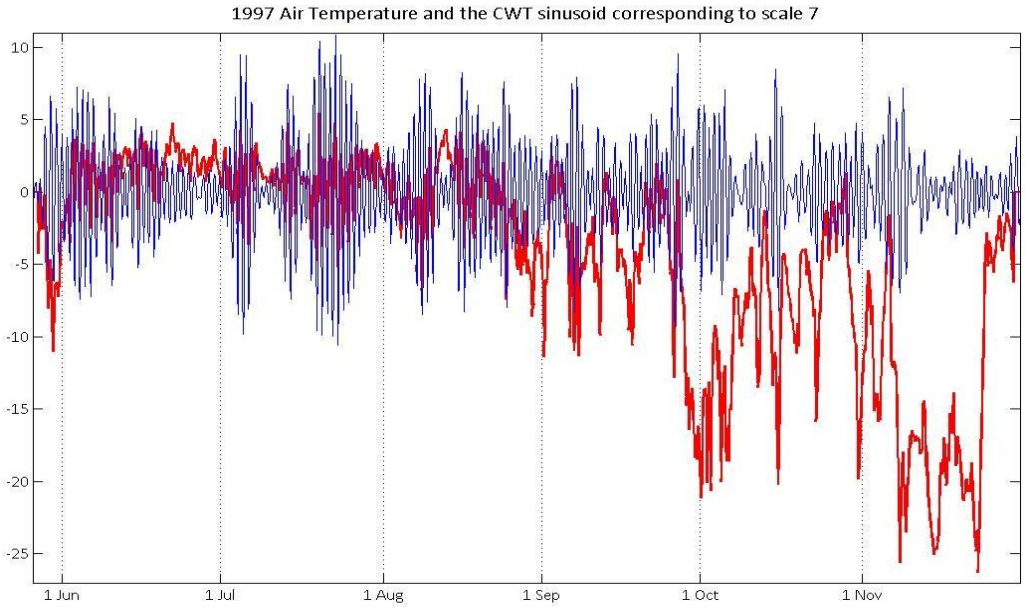

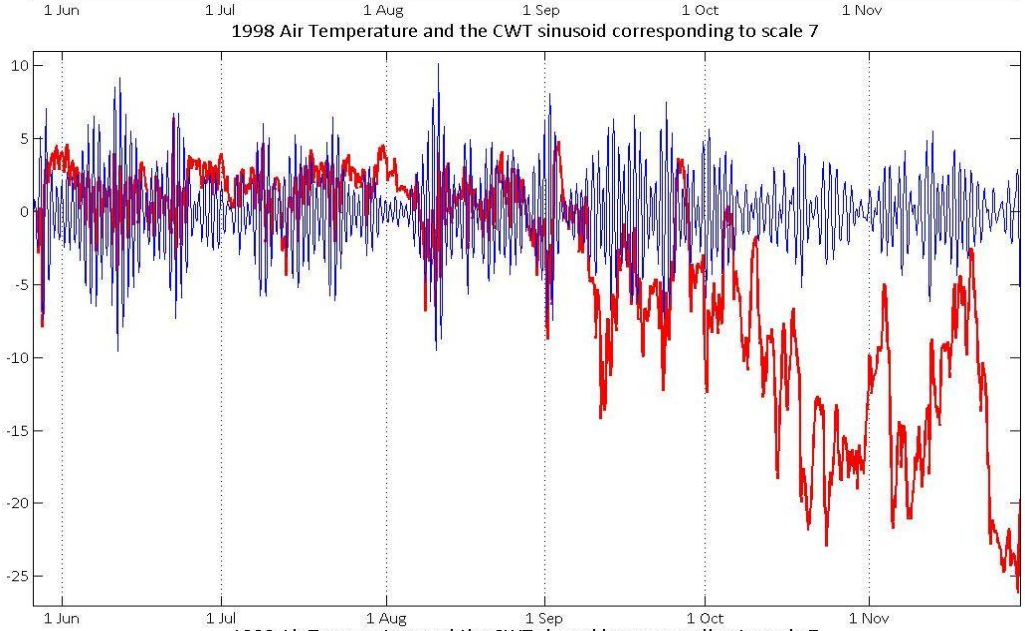

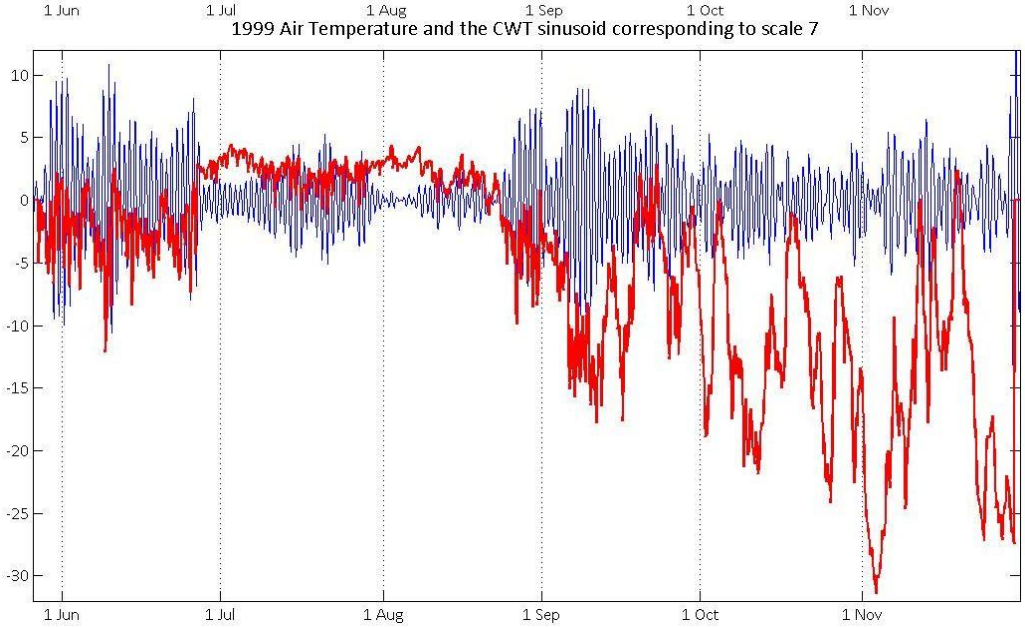

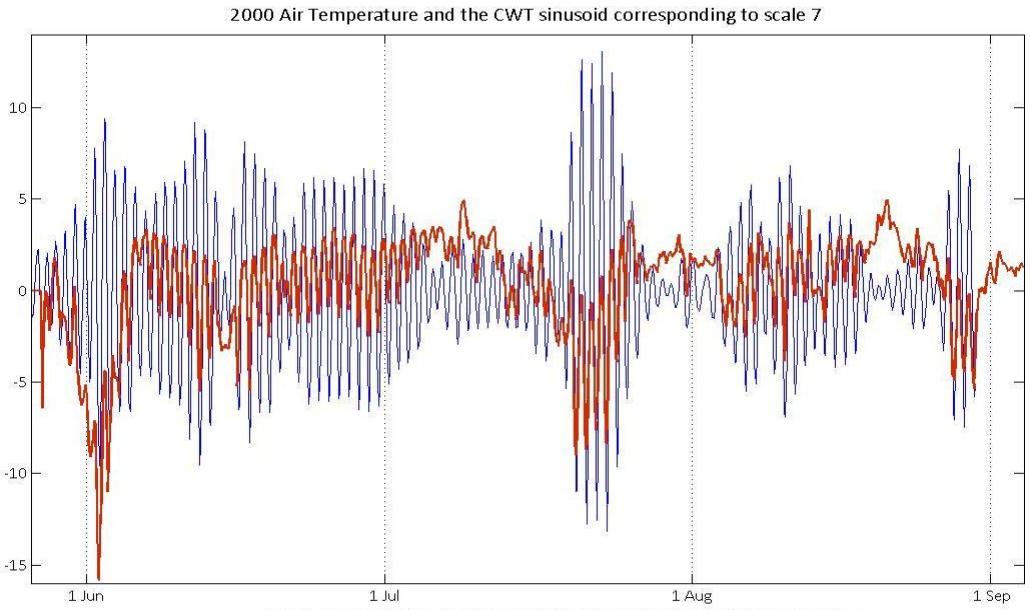
2000 Air Temperature and the CWT sinusoid corresponding to scale 7
10
5
0
-5
-10
-15
1 Jun
1 Jul
1 Aug
1 Sep

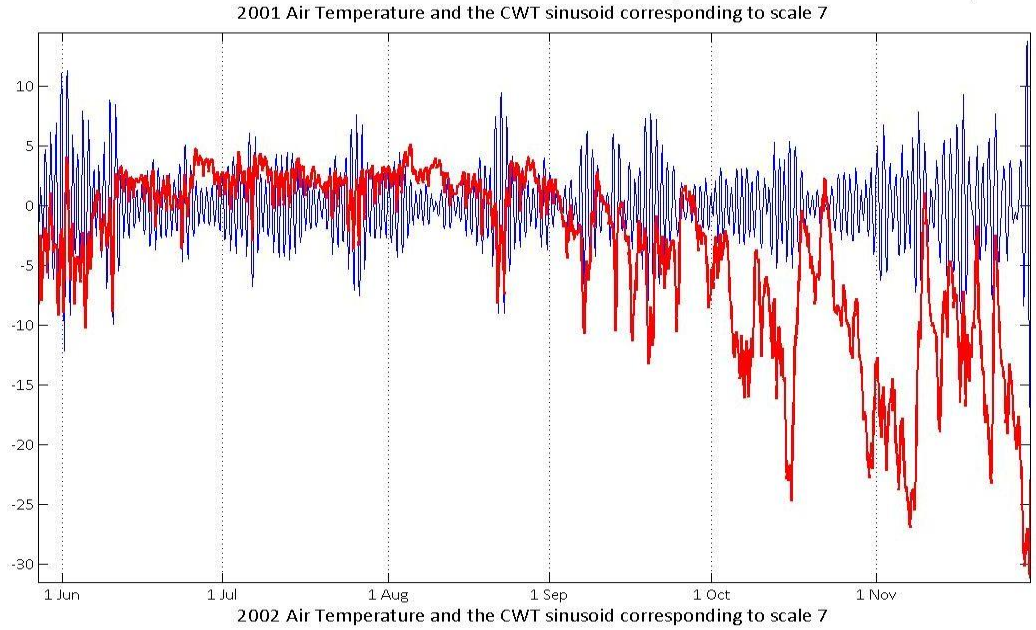
2001 Air Temperature and the CWT sinusoid corresponding to scale 7
10
5
0
-5
-10
-15
-20
-25
-30
1 Jun
1 Jul
1 Aug
1 Sep
1 Oct
1 Nov

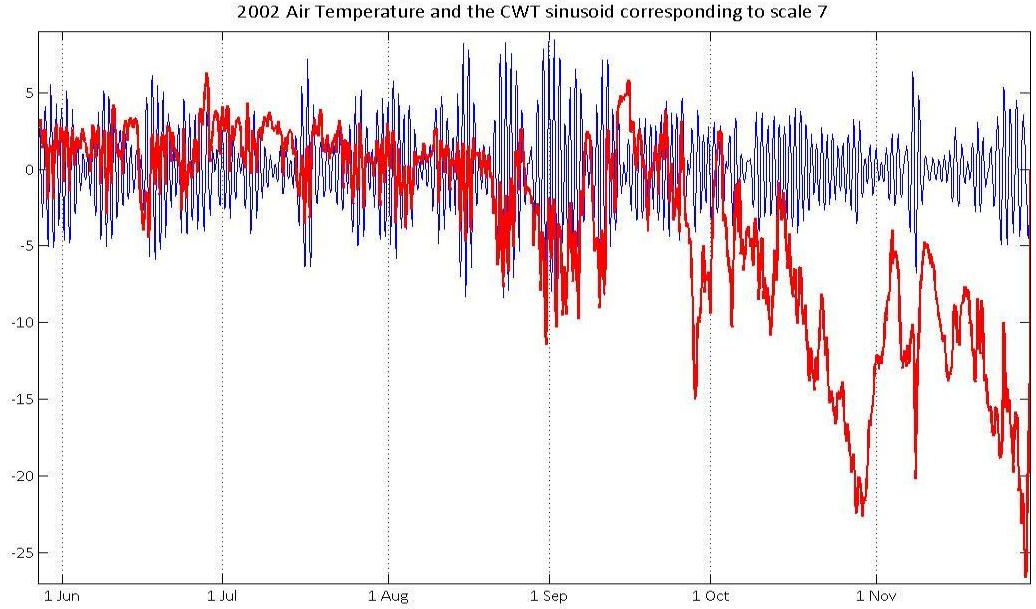
2002 Air Temperature and the CWT sinusoid corresponding to scale 7
5
0
-5
-10
-15
-20
-25
1 Jun
1 Jul
1 Aug
1 Sep
1 Oct
1 Nov

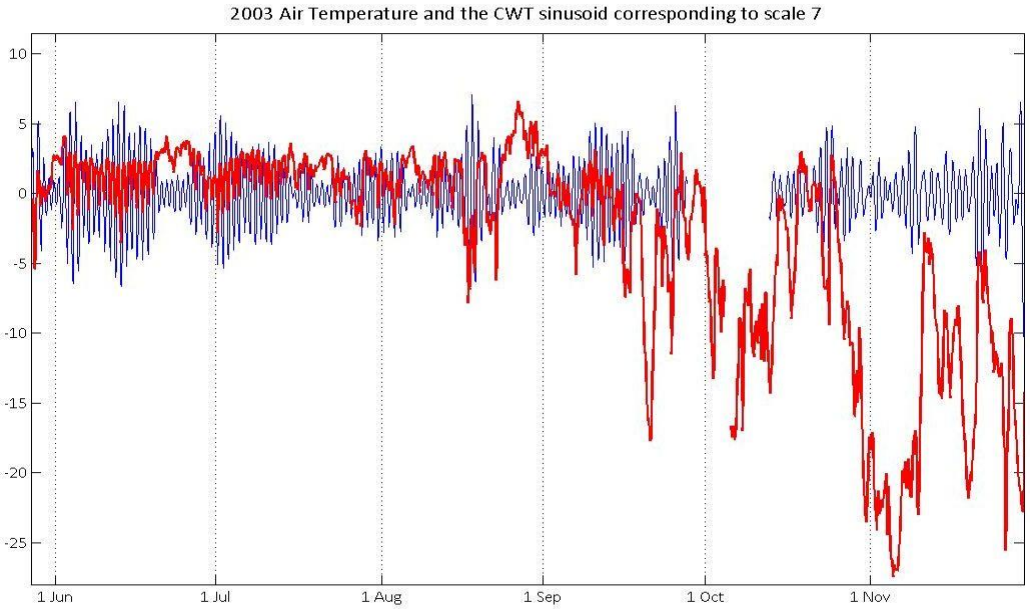
2003 Air Temperature and the CWT sinusoid corresponding to scale 7
10
5
0
-5
-10
-15
-20
-25
1 Jun
1 Jul
1 Aug
1 Sep
1 Oct
1 Nov

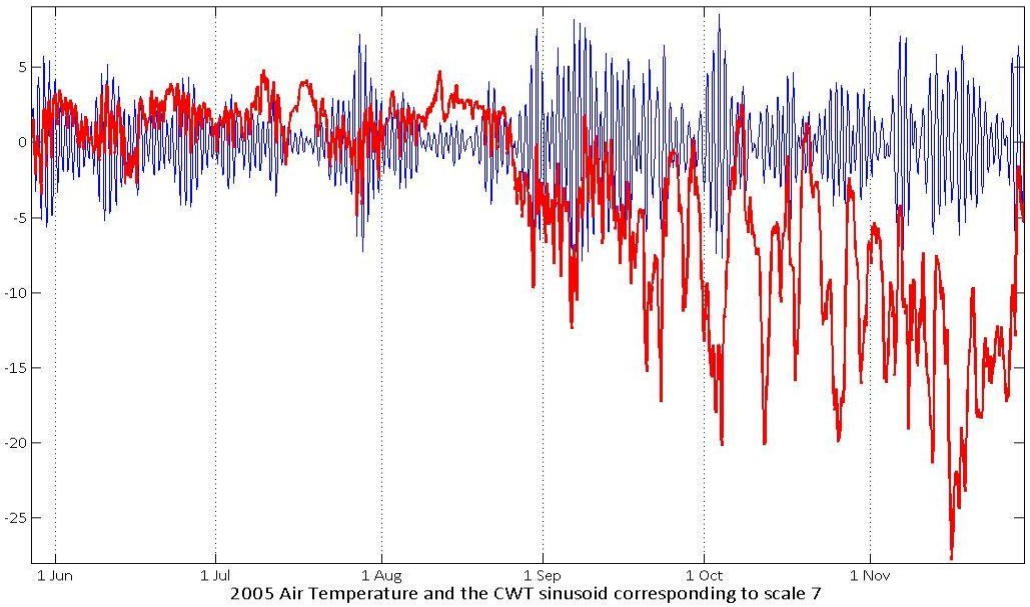
2004 Air Temperature and the CWT sinusoid corresponding to scale 7
5
0
-5
-10
-15
-20
-25
1 Jun
1 Jul
1 Aug
1 Sep
1 Oct
1 Nov

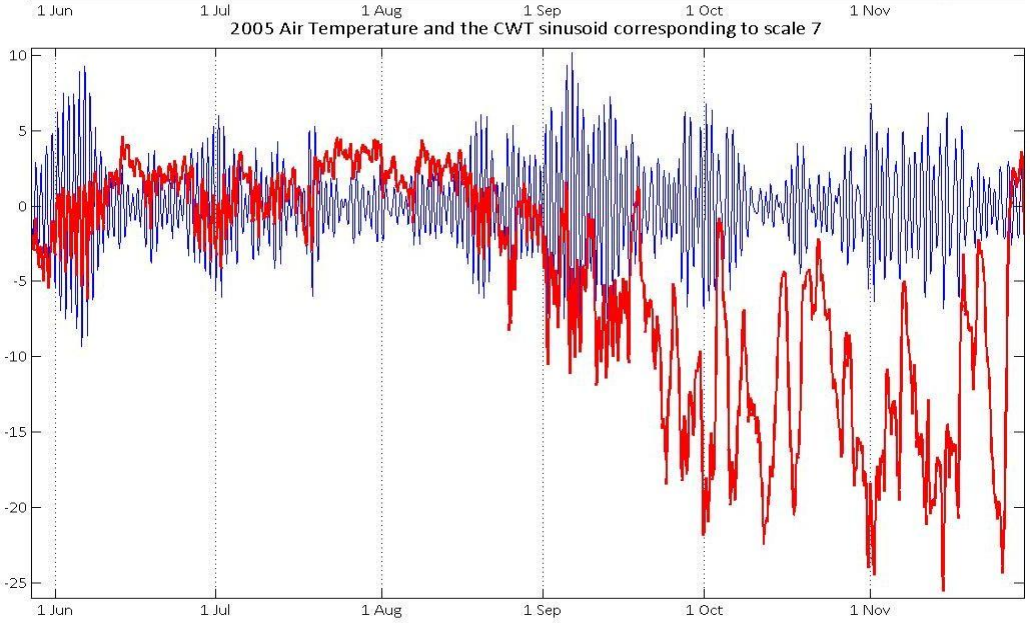
2005 Air Temperature and the CWT sinusoid corresponding to scale 7
10
5
0
-5
-10
-15
-20
-25
1 Jun
1 Jul
1 Aug
1 Sep
1 Oct
1 Nov

Appendix 3: CWT Graphs for Net Shortwave Radiation, 1997-2005

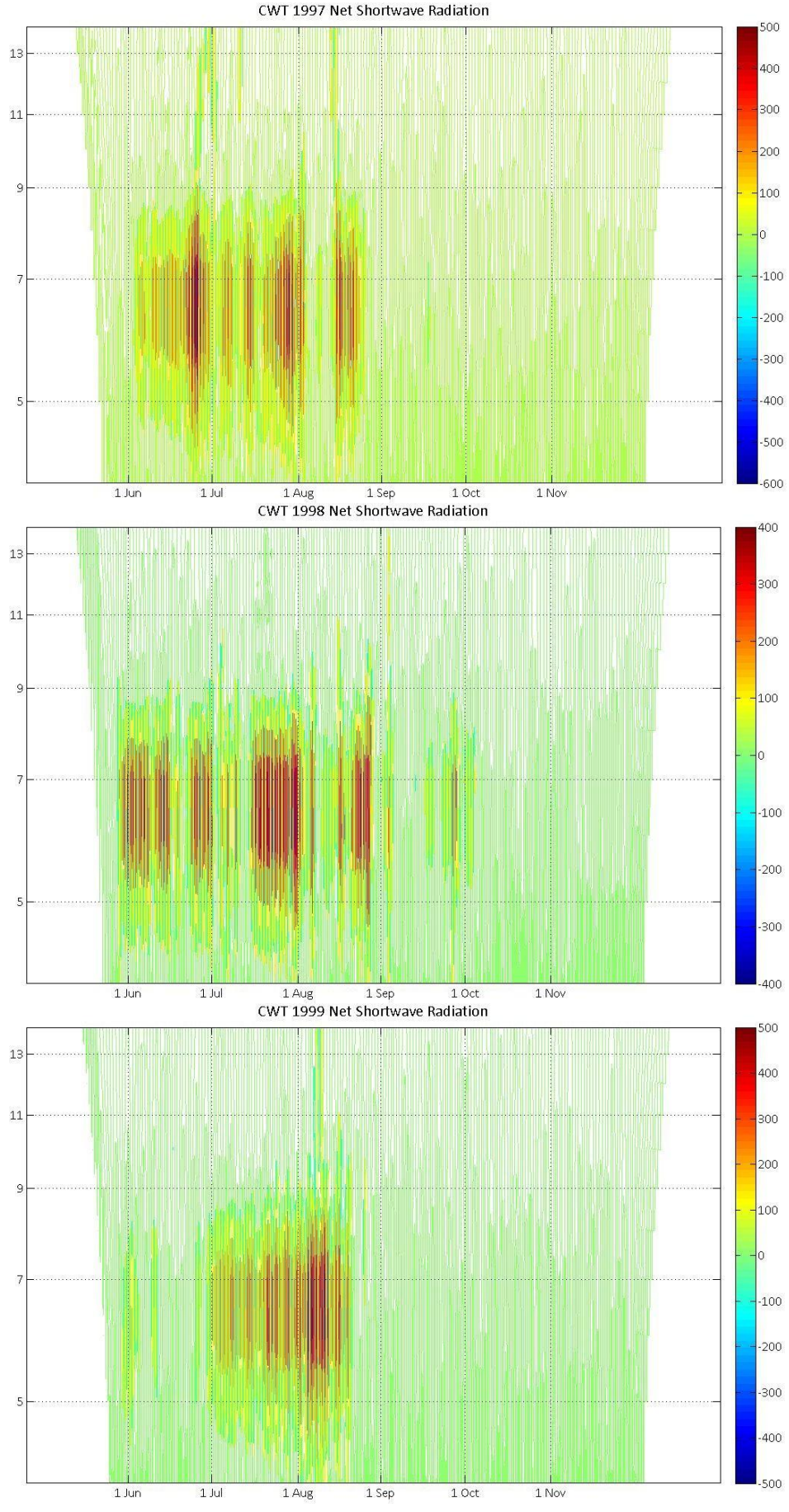

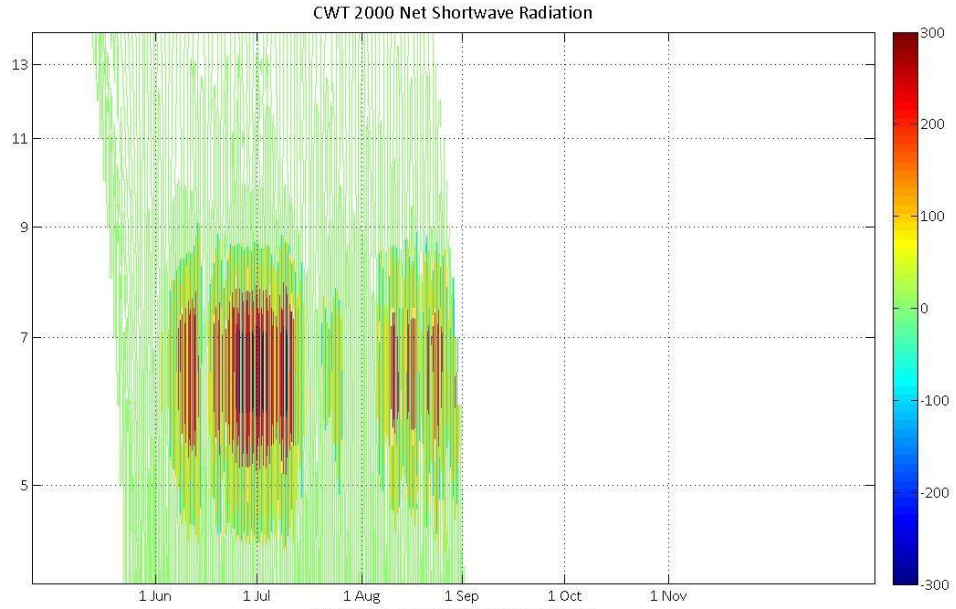
CWT 2000 Net Shortwave Radiation
13
11
9
7
5
1 Jun
1 Jul
1 Aug
1 Sep
1 Oct
1 Nov
300
200
100
0
-100
-200
-300

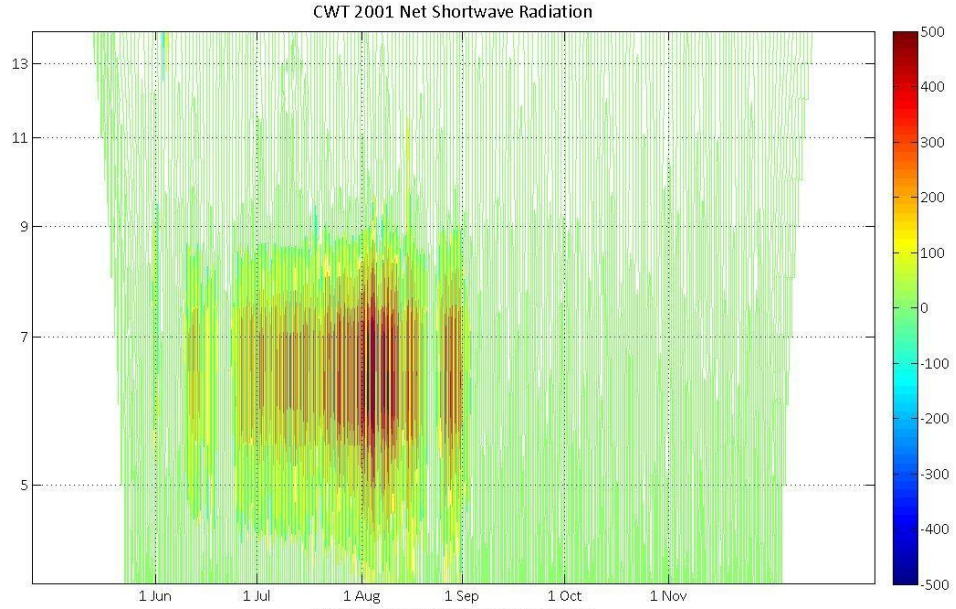
CWT 2001 Net Shortwave Radiation
13
11
9
7
5
1 Jun
1 Jul
1 Aug
1 Sep
1 Oct
1 Nov
500
400
300
200
100
0
-100
-200
-300
-400
-500

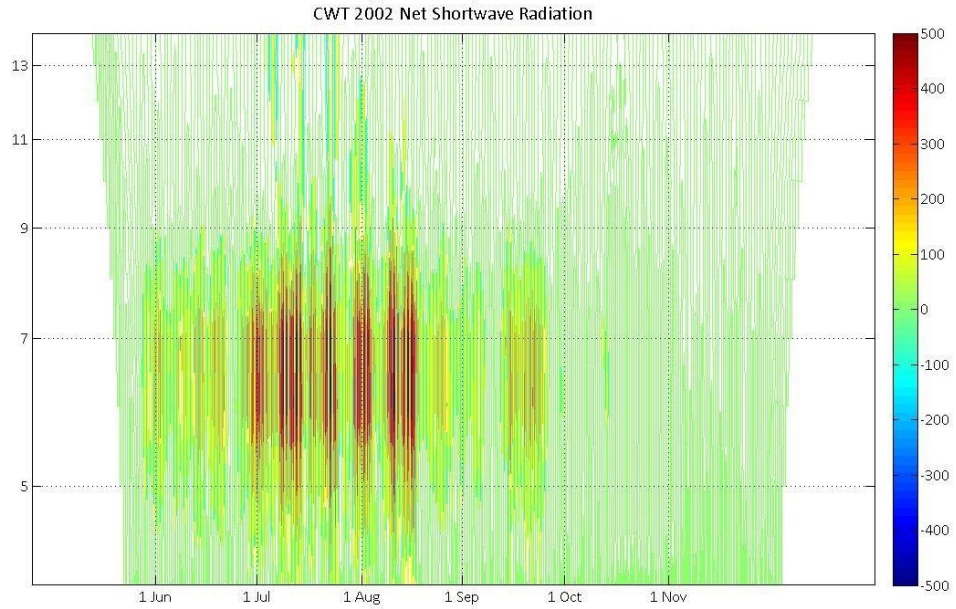
CWT 2002 Net Shortwave Radiation
13
11
9
7
5
1 Jun
1 Jul
1 Aug
1 Sep
1 Oct
1 Nov
500
400
300
200
100
0
-100
-200
-300
-400
-500

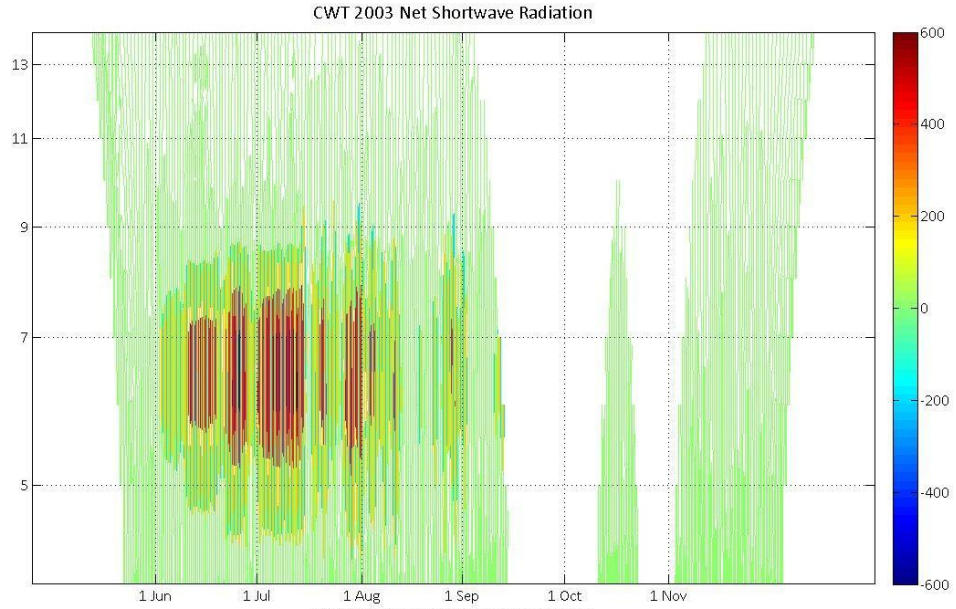
CWT 2003 Net Shortwave Radiation
13
11
9
7
5
1 Jun
1 Jul
1 Aug
1 Sep
1 Oct
1 Nov
600
400
200
0
-200
-400
-600

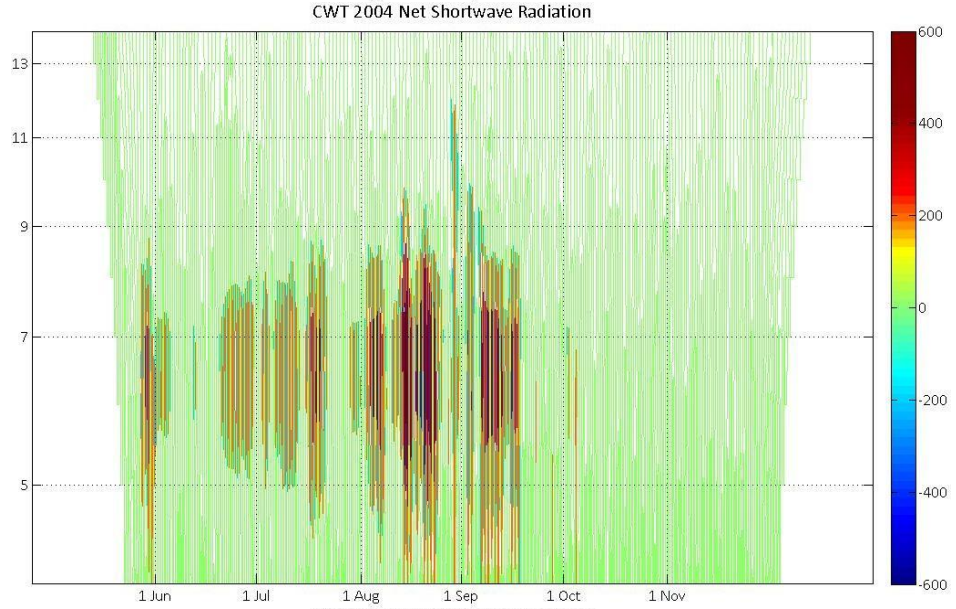
CWT 2004 Net Shortwave Radiation
13
11
9
7
5
1 Jun
1 Jul
1 Aug
1 Sep
1 Oct
1 Nov
600
400
200
0
-200
-400
-600

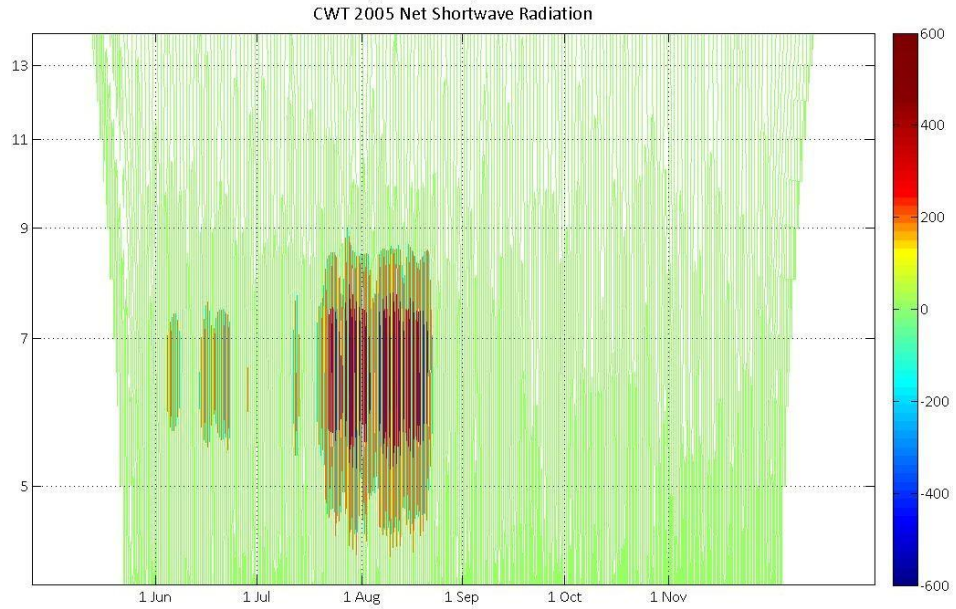
CWT 2005 Net Shortwave Radiation
13
11
9
7
5
1 Jun
1 Jul
1 Aug
1 Sep
1 Oct
1 Nov
600
400
200
0
-200
-400
-600

Appendix 4: CWT Graphs for Discharge, 1997-2005

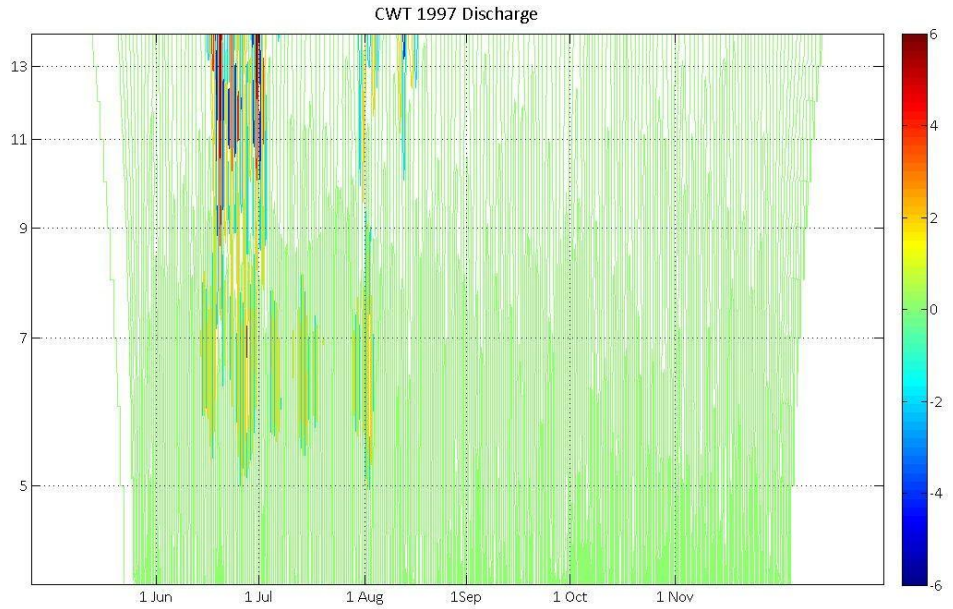

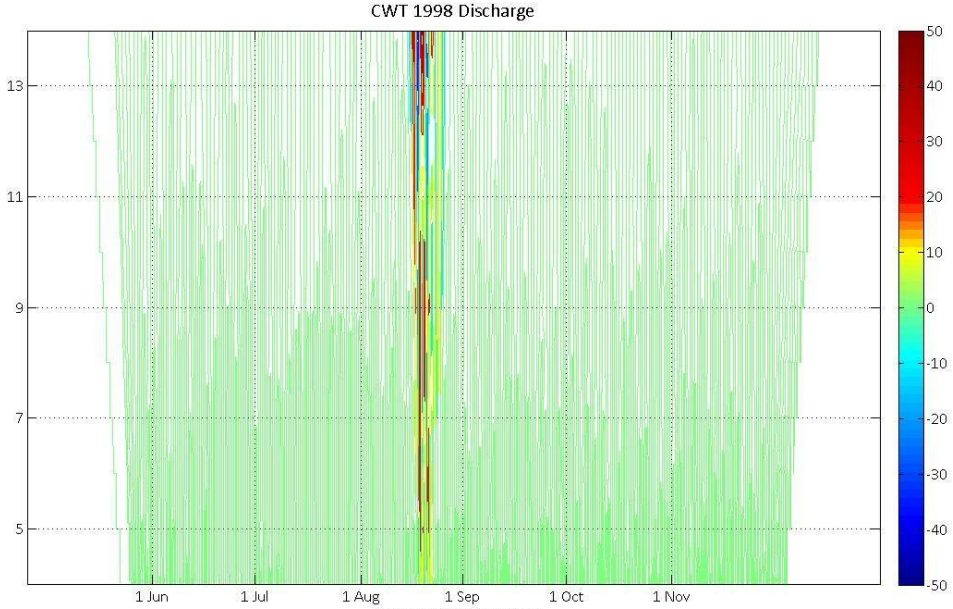

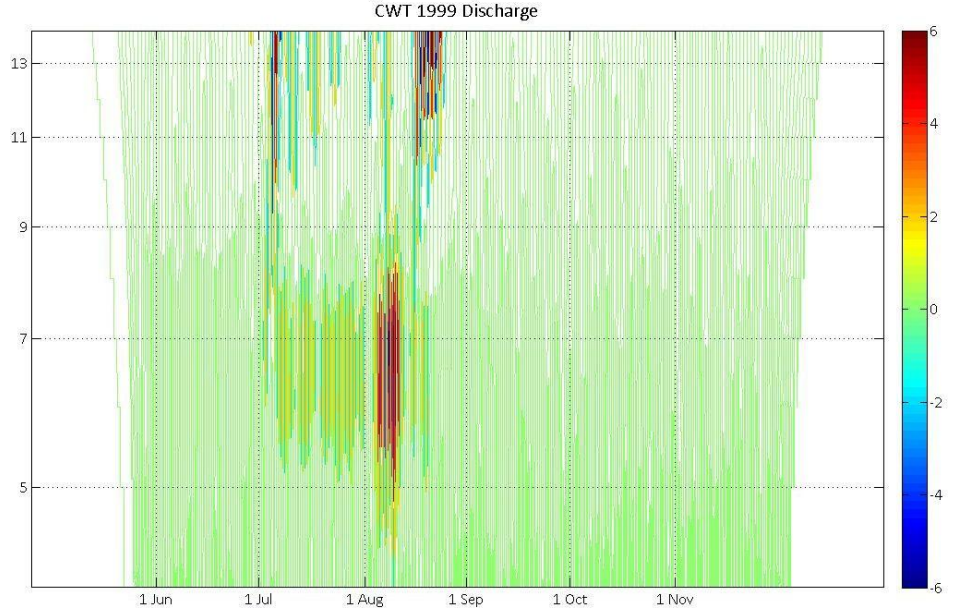

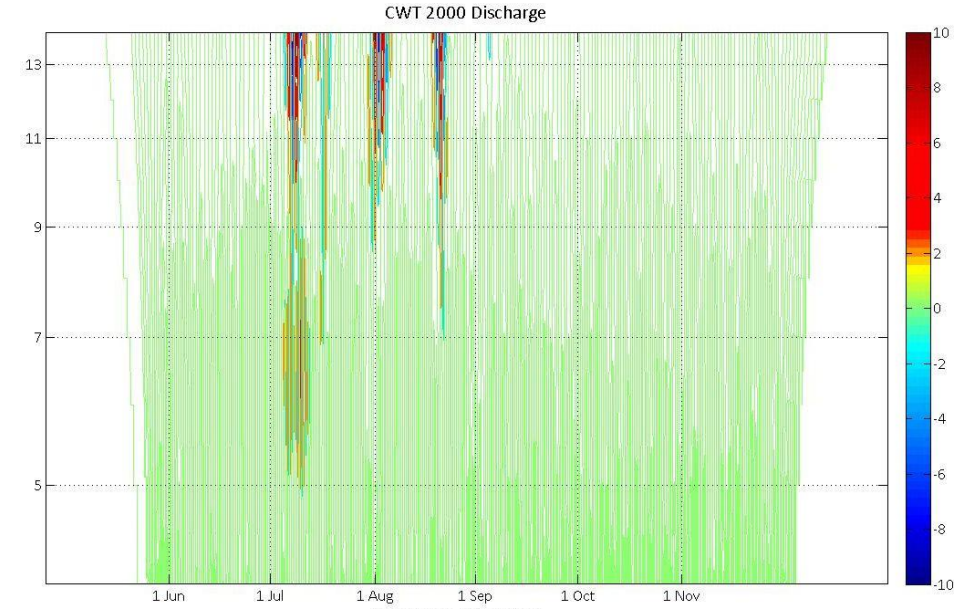
CWT 2000 Discharge
13
11
9
7
5
1 Jun
1 Jul
1 Aug
1 Sep
1 Oct
1 Nov
10
8
6
4
2
0
-2
-4
-6
-8
-10

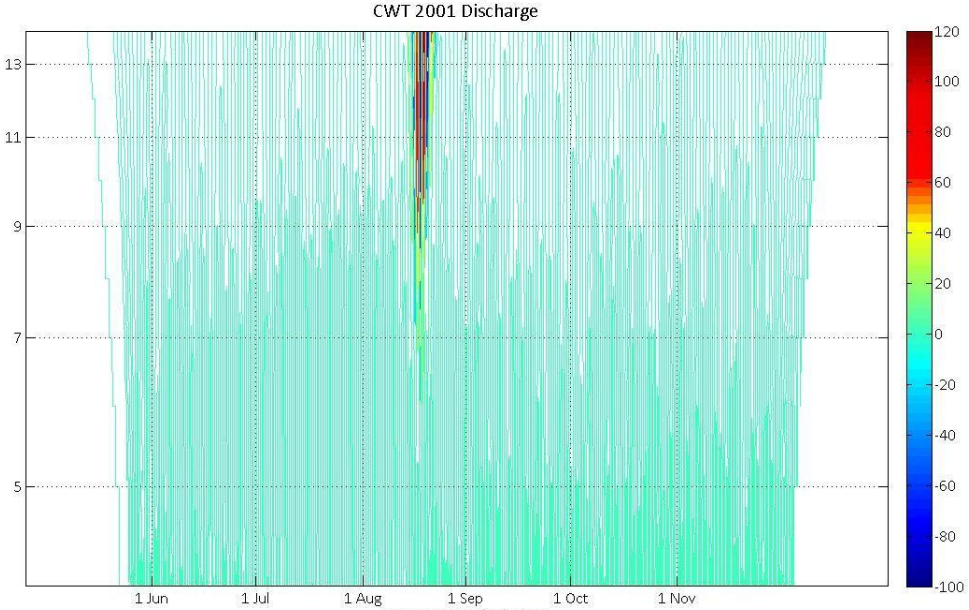
CWT 2001 Discharge
13
11
9
7
5
1 Jun
1 Jul
1 Aug
1 Sep
1 Oct
1 Nov
120
100
80
60
40
20
0
-20
-40
-60
-80
-100

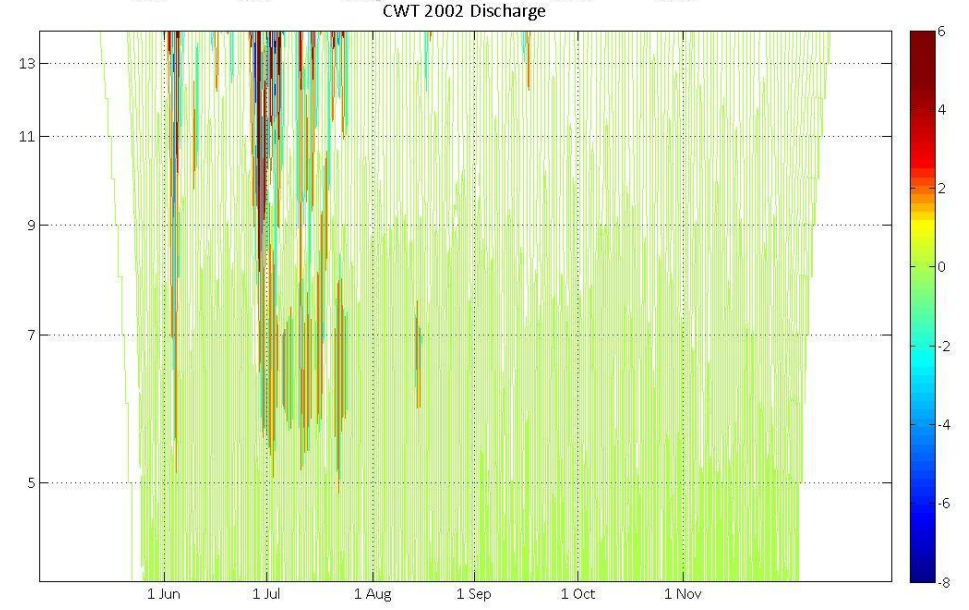
CWT 2002 Discharge
13
11
9
7
5
1 Jun
1 Jul
1 Aug
1 Sep
1 Oct
1 Nov
6
4
2
0
-2
-4
-6
-8

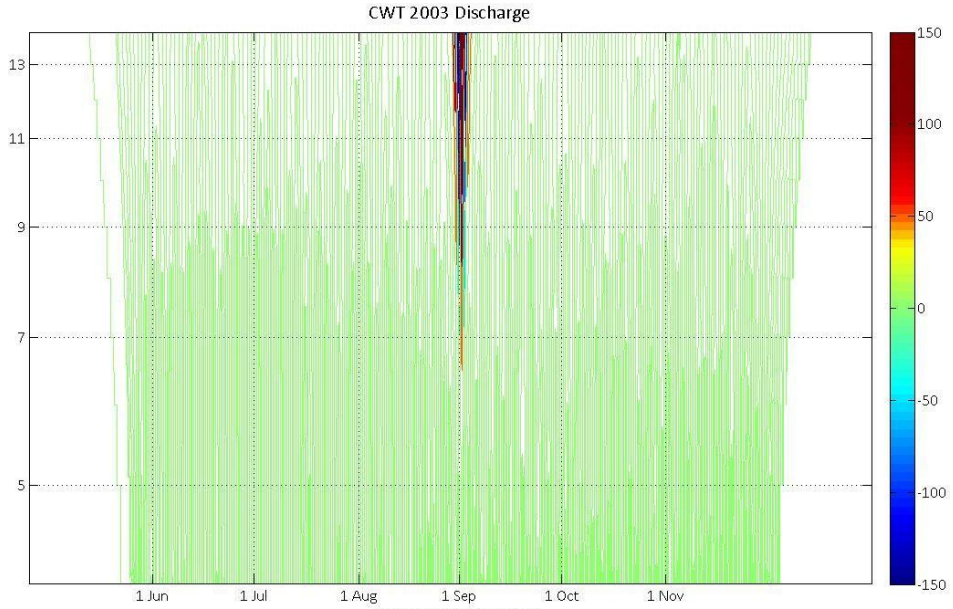
CWT 2003 Discharge
13
11
9
7
5
1 Jun
1 Jul
1 Aug
1 Sep
1 Oct
1 Nov
150
100
50
0
-50
-100
-150

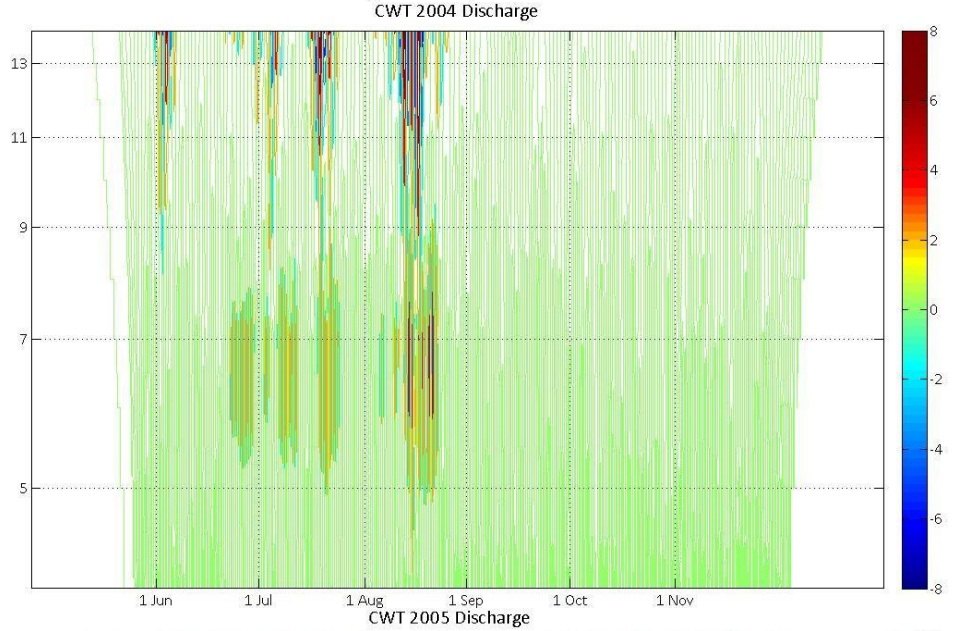
CWT 2004 Discharge
13
11
9
7
5
1 Jun
1 Jul
1 Aug
1 Sep
1 Oct
1 Nov
8
6
4
2
0
-2
-4
-6
-8


CWT 2005 Discharge
13
11
9
7
5
1 Jun
1 Jul
1 Aug
1 Sep
1 Oct
1 Nov
300
250
200
150
100
50
0
-50
-100
-150
-200

Appendix 5: Wavelet Coherence, Phase Difference and Average Coherence per Scale for Air Temp. and Discharge

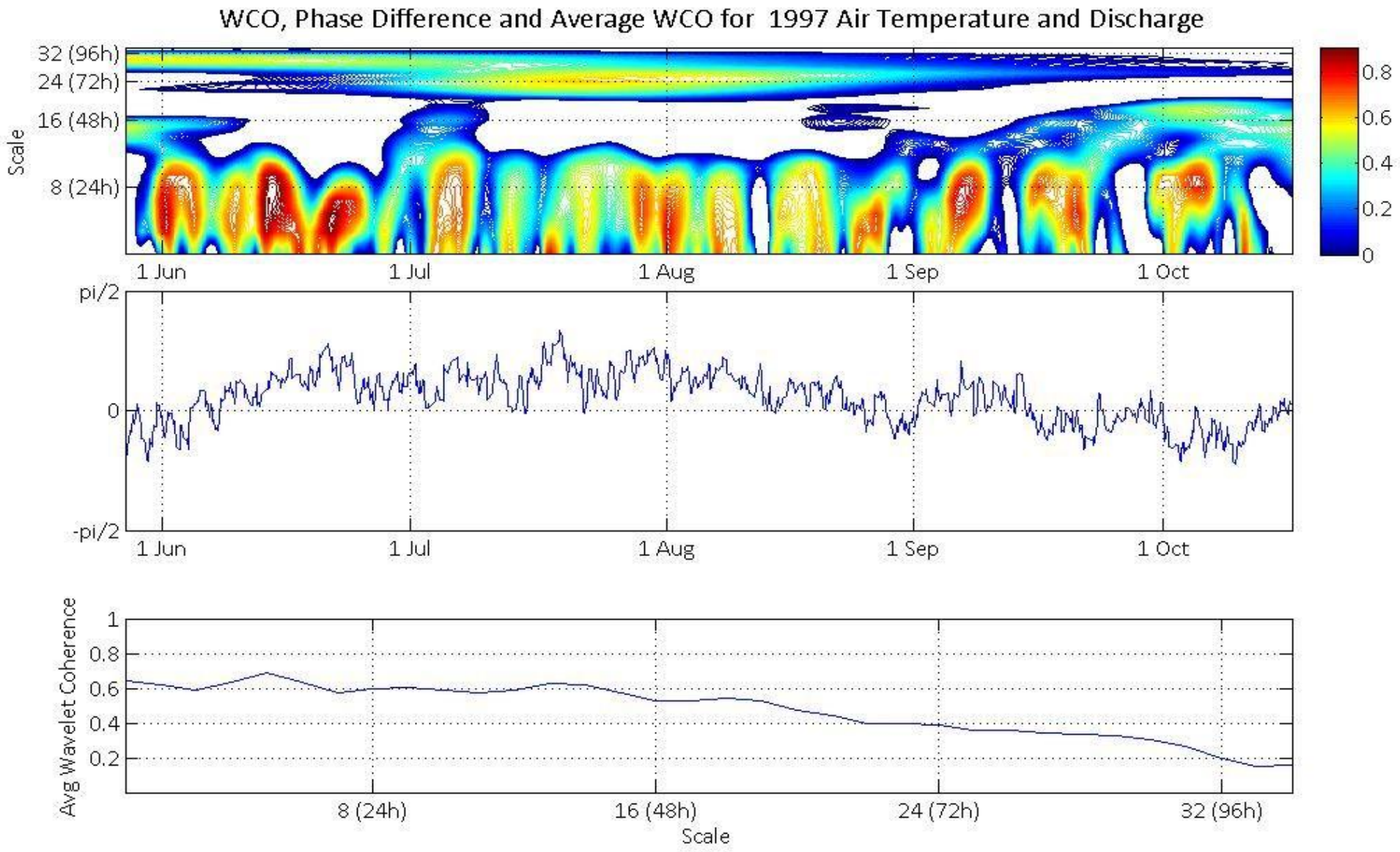

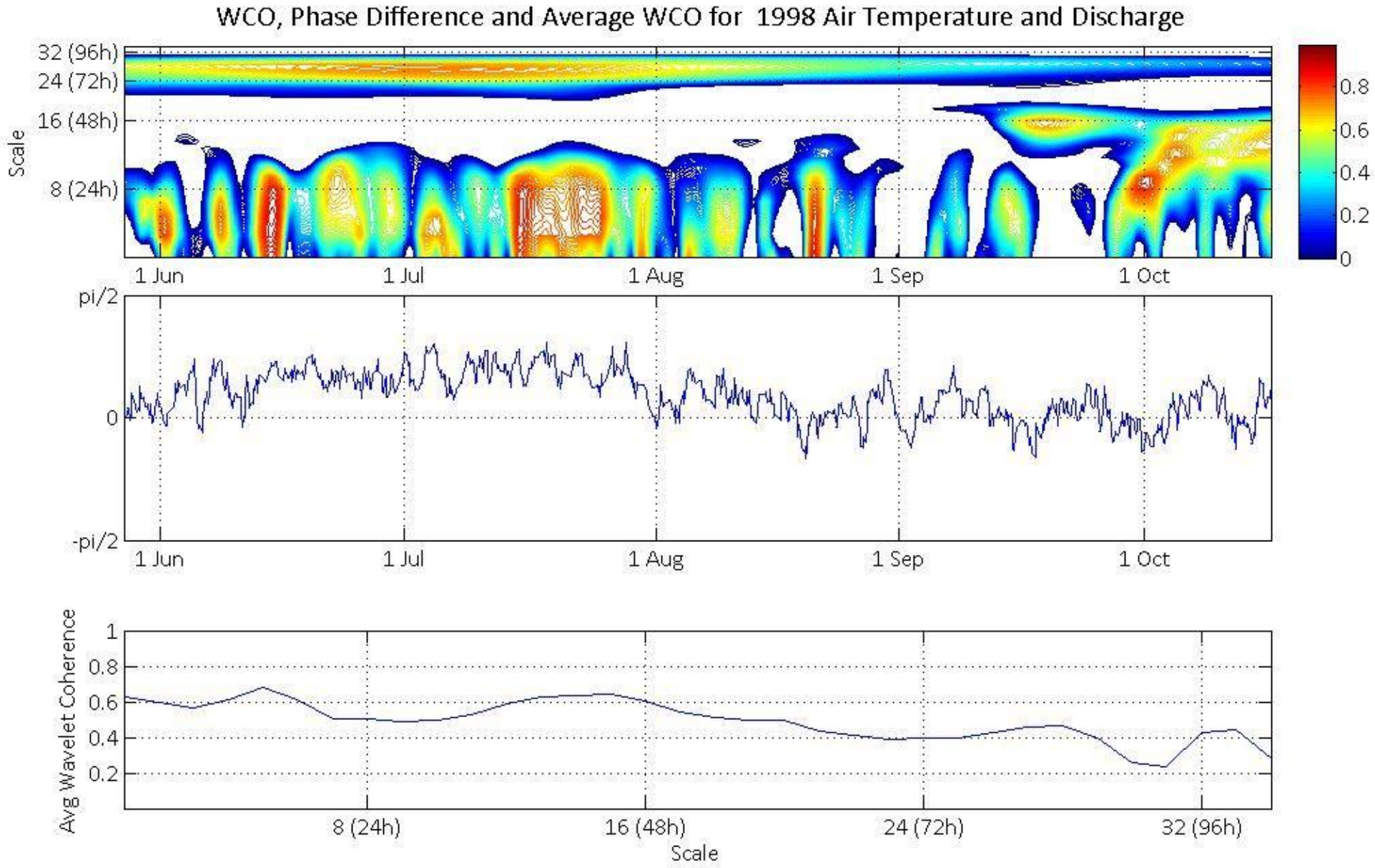
WCO, Phase Difference and Average WCO for 1998 Air Temperature and Discharge
Scale
32 (96h)
24 (72h)
16 (48h)
8 (24h)
1 Jun
1 Jul
1 Aug
1 Sep
1 Oct
0.8
0.6
0.4
0.2
0
pi/2
0
-pi/2
Avg Wavelet Coherence
1
0.8
0.6
0.4
0.2
8 (24h)
16 (48h)
24 (72h)
32 (96h)
Scale

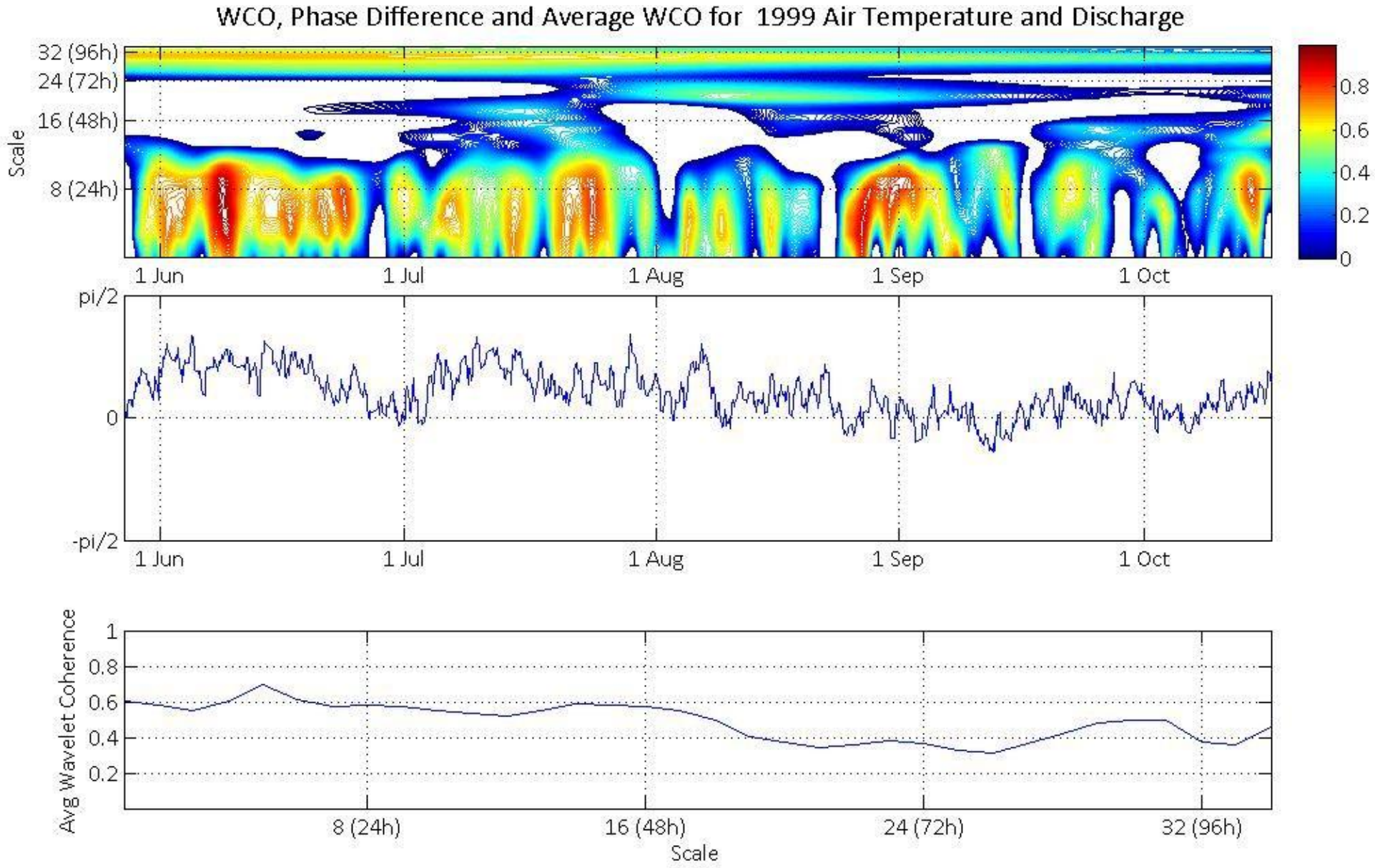
WCO, Phase Difference and Average WCO for 1999 Air Temperature and Discharge
Scale
32 (96h)
24 (72h)
16 (48h)
8 (24h)
1 Jun
1 Jul
1 Aug
1 Sep
1 Oct
0.8
0.6
0.4
0.2
0
pi/2
0
-pi/2
Avg Wavelet Coherence
1
0.8
0.6
0.4
0.2
8 (24h)
16 (48h)
24 (72h)
32 (96h)
Scale

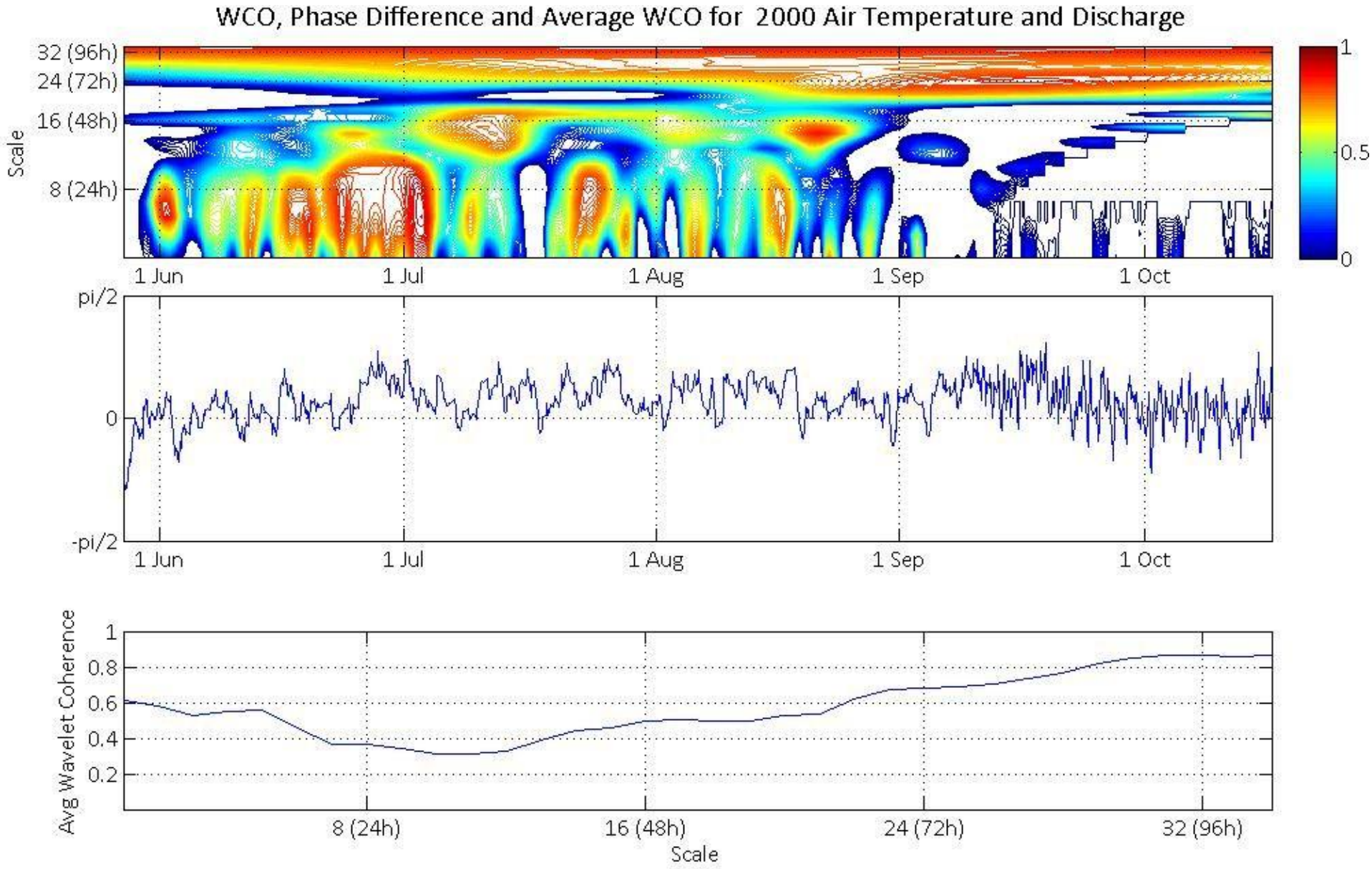
WCO, Phase Difference and Average WCO for 2000 Air Temperature and Discharge
Scale
32 (96h)
24 (72h)
16 (48h)
8 (24h)
1 Jun
1 Jul
1 Aug
1 Sep
1 Oct
1
0.5
0
pi/2
0
-pi/2
Avg Wavelet Coherence
1
0.8
0.6
0.4
0.2
8 (24h)
16 (48h)
24 (72h)
32 (96h)
Scale

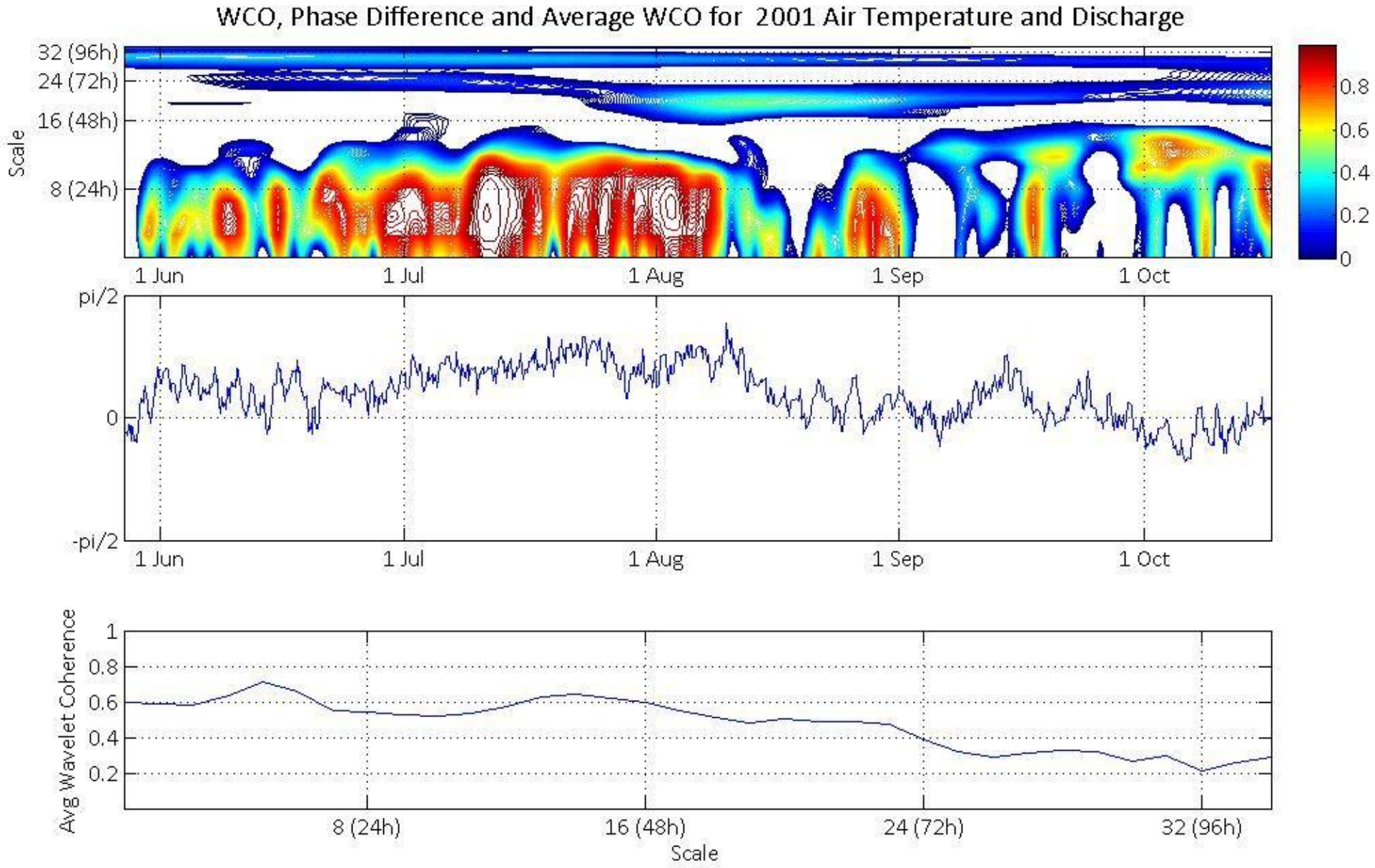
WCO, Phase Difference and Average WCO for 2001 Air Temperature and Discharge
Scale
32 (96h)
24 (72h)
16 (48h)
8 (24h)
1 Jun
1 Jul
1 Aug
1 Sep
1 Oct
0.8
0.6
0.4
0.2
0
pi/2
0
-pi/2
Avg Wavelet Coherence
1
0.8
0.6
0.4
0.2
8 (24h)
16 (48h)
24 (72h)
32 (96h)
Scale

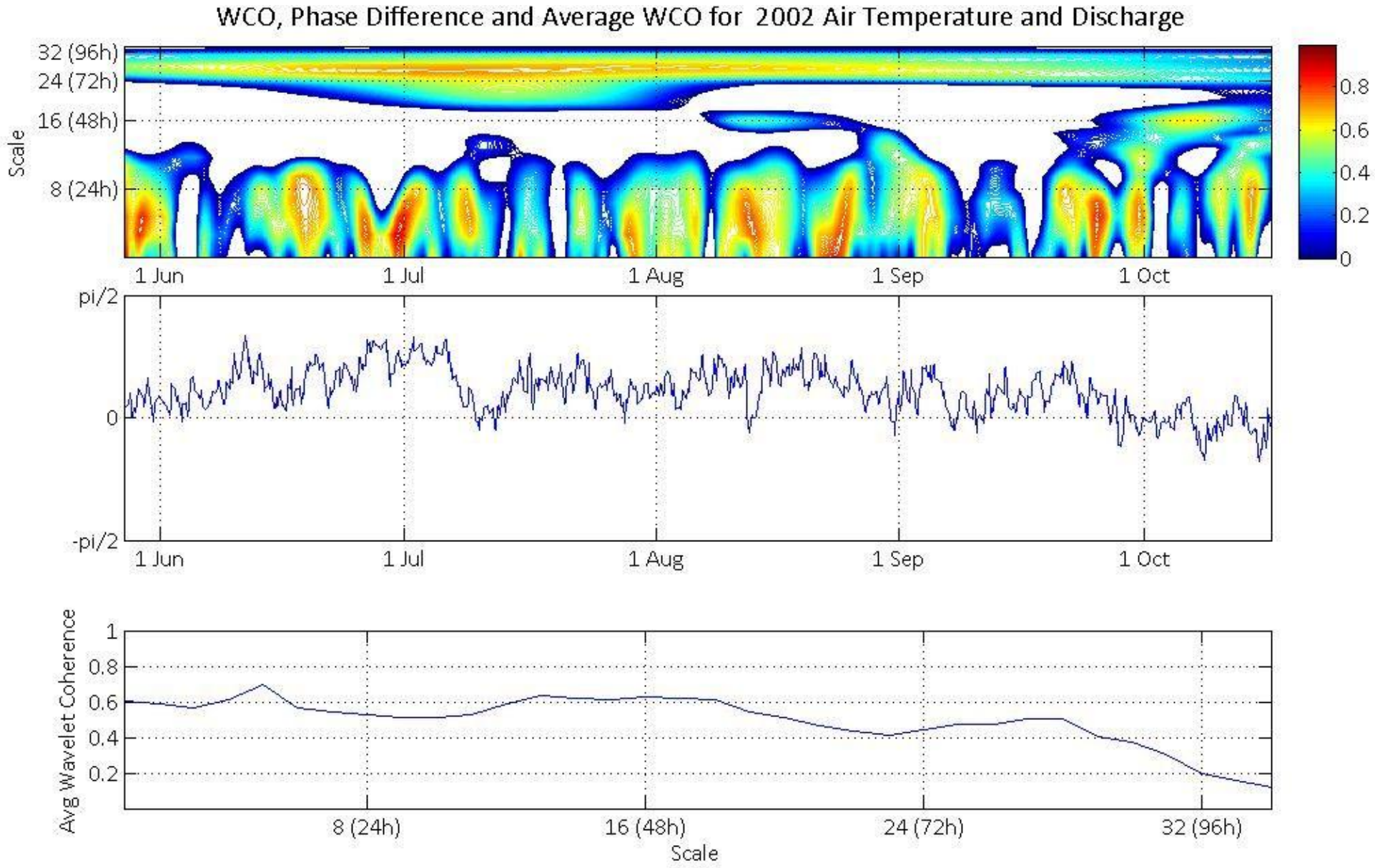
WCO, Phase Difference and Average WCO for 2002 Air Temperature and Discharge
Scale
32 (96h)
24 (72h)
16 (48h)
8 (24h)
1 Jun
1 Jul
1 Aug
1 Sep
1 Oct
0.8
0.6
0.4
0.2
0
pi/2
0
-pi/2
Avg Wavelet Coherence
1
0.8
0.6
0.4
0.2
8 (24h)
16 (48h)
24 (72h)
32 (96h)
Scale

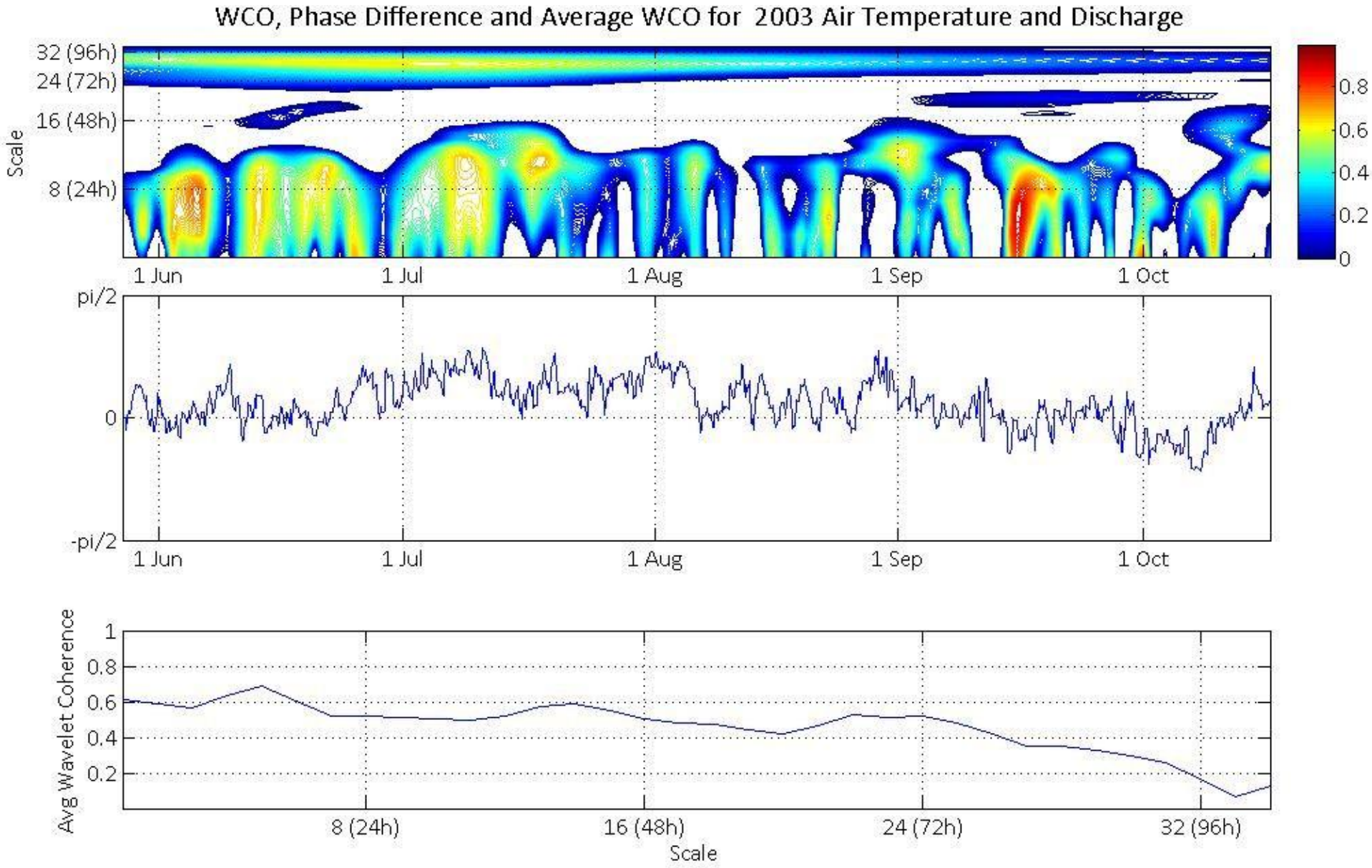
WCO, Phase Difference and Average WCO for 2003 Air Temperature and Discharge
Scale
32 (96h)
24 (72h)
16 (48h)
8 (24h)
1 Jun
1 Jul
1 Aug
1 Sep
1 Oct
0.8
0.6
0.4
0.2
0
pi/2
0
-pi/2
Avg Wavelet Coherence
1
0.8
0.6
0.4
0.2
8 (24h)
16 (48h)
24 (72h)
32 (96h)
Scale

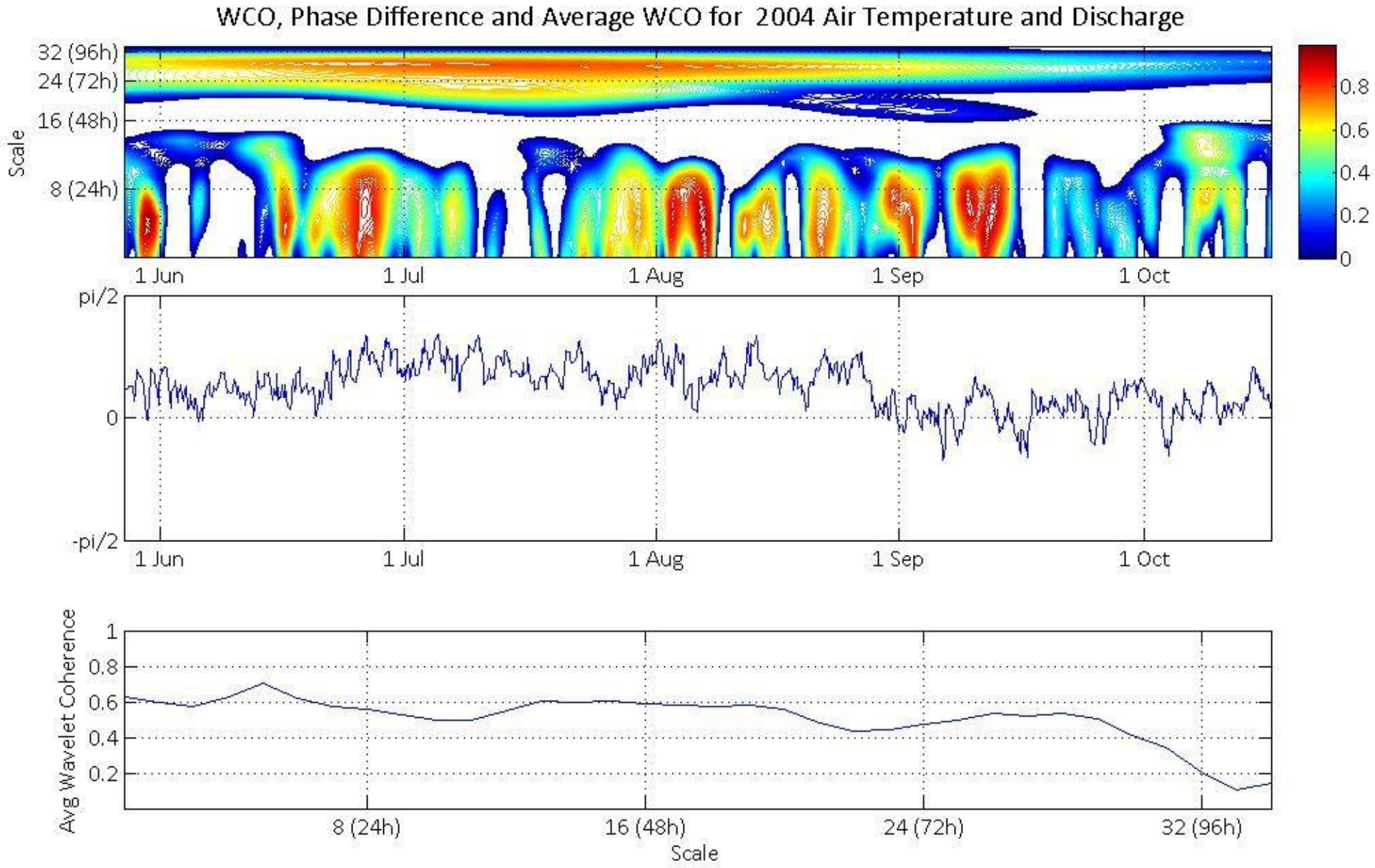
WCO, Phase Difference and Average WCO for 2004 Air Temperature and Discharge
Scale
32 (96h)
24 (72h)
16 (48h)
8 (24h)
1 Jun
1 Jul
1 Aug
1 Sep
1 Oct
0.8
0.6
0.4
0.2
0
pi/2
0
-pi/2
Avg Wavelet Coherence
1
0.8
0.6
0.4
0.2
8 (24h)
16 (48h)
24 (72h)
32 (96h)
Scale

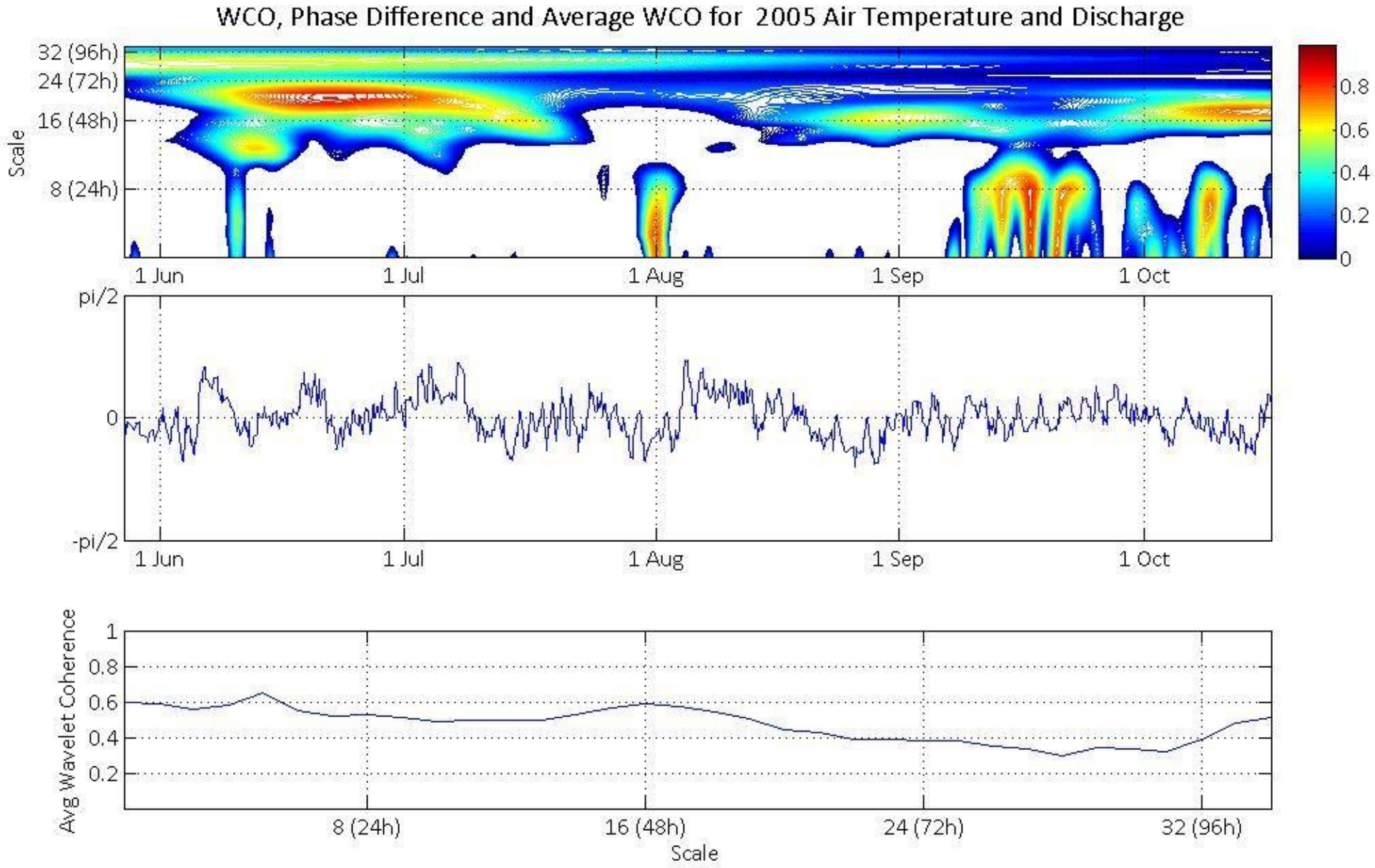
WCO, Phase Difference and Average WCO for 2005 Air Temperature and Discharge
Scale
32 (96h)
24 (72h)
16 (48h)
8 (24h)
1 Jun
1 Jul
1 Aug
1 Sep
1 Oct
0.8
0.6
0.4
0.2
0
pi/2
0
-pi/2
Avg Wavelet Coherence
1
0.8
0.6
0.4
0.2
8 (24h)
16 (48h)
24 (72h)
32 (96h)
Scale

Appendix 6: Wavelet Coherence, Phase Difference and Average Coherence per Scale for Net SW Rad. and Discharge

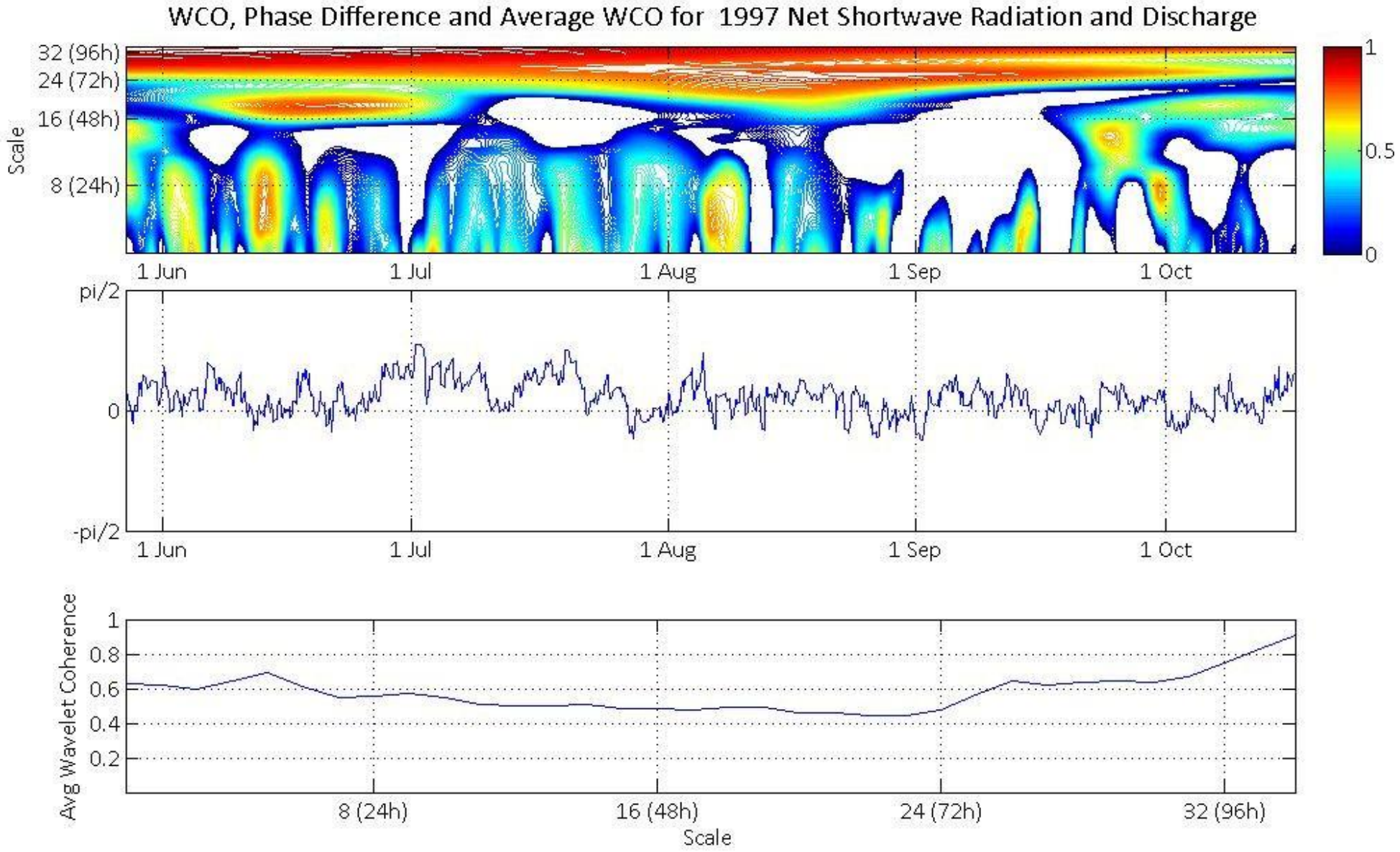

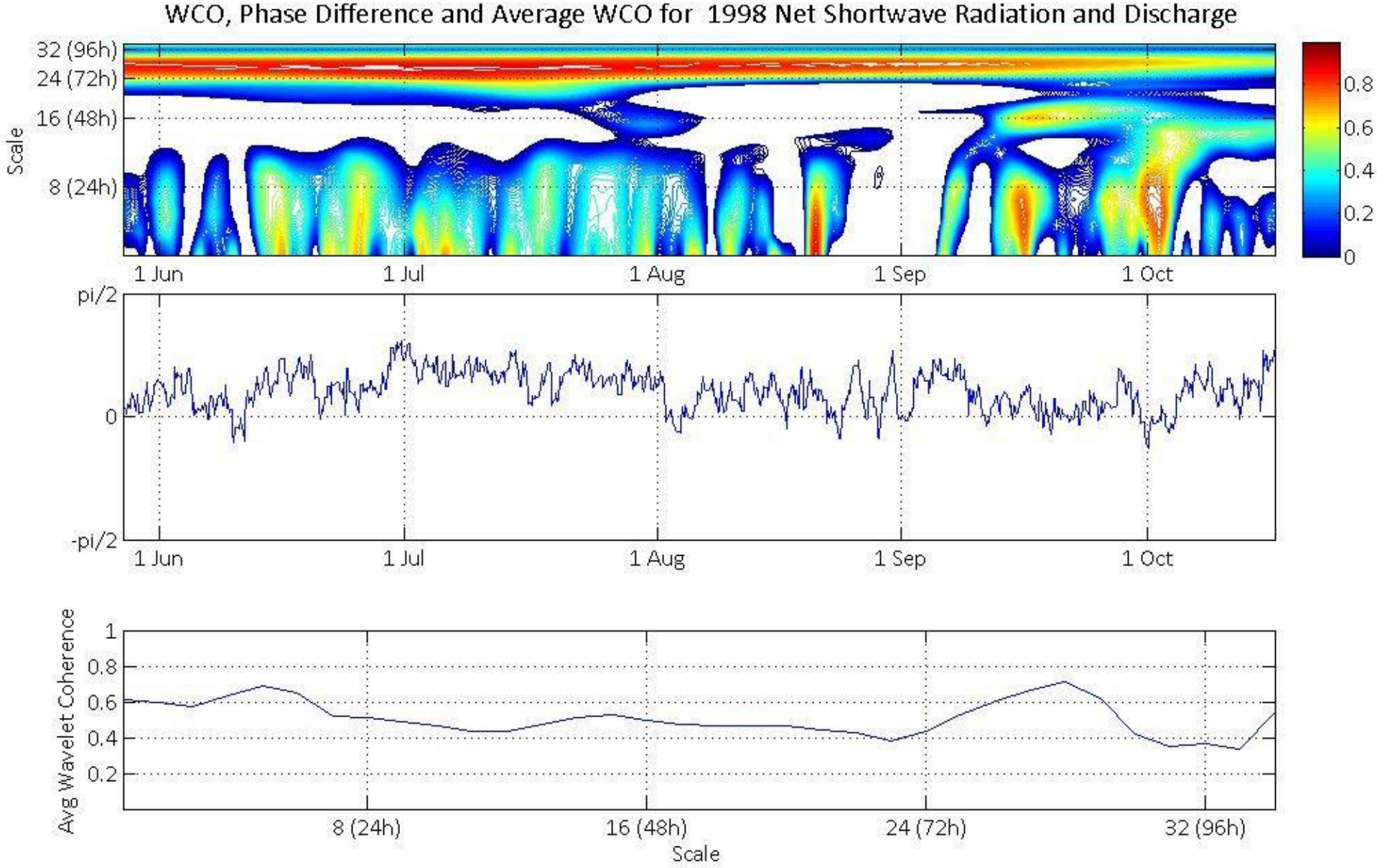
WCO, Phase Difference and Average WCO for 1998 Net Shortwave Radiation and Discharge
Scale
32 (96h)
24 (72h)
16 (48h)
8 (24h)
1 Jun
1 Jul
1 Aug
1 Sep
1 Oct
0.8
0.6
0.4
0.2
0
pi/2
0
-pi/2
Avg Wavelet Coherence
1
0.8
0.6
0.4
0.2
8 (24h)
16 (48h)
24 (72h)
32 (96h)
Scale

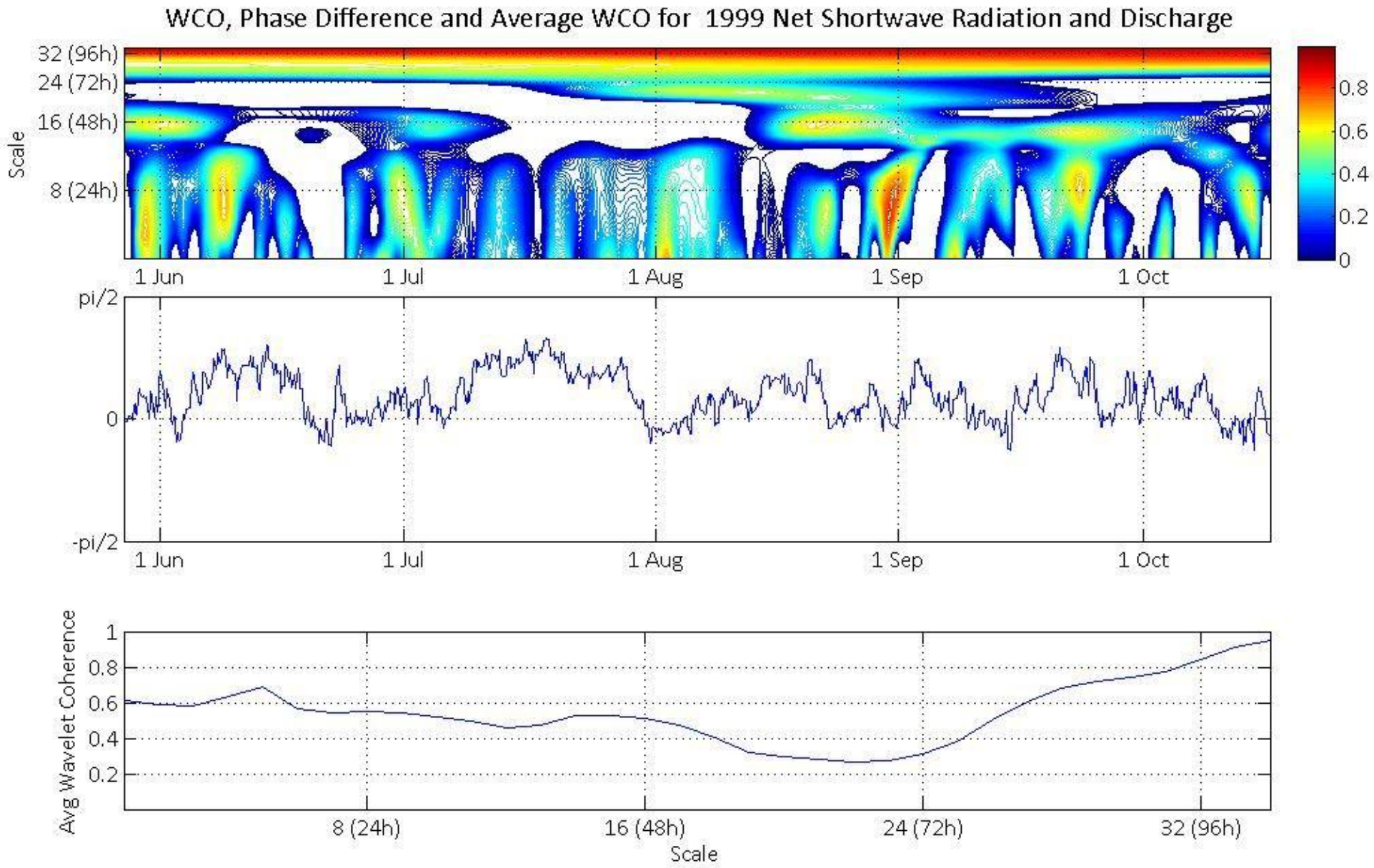
WCO, Phase Difference and Average WCO for 1999 Net Shortwave Radiation and Discharge
Scale
32 (96h)
24 (72h)
16 (48h)
8 (24h)
1 Jun
1 Jul
1 Aug
1 Sep
1 Oct
0.8
0.6
0.4
0.2
0
pi/2
0
-pi/2
Avg Wavelet Coherence
1
0.8
0.6
0.4
0.2
8 (24h)
16 (48h)
24 (72h)
32 (96h)
Scale

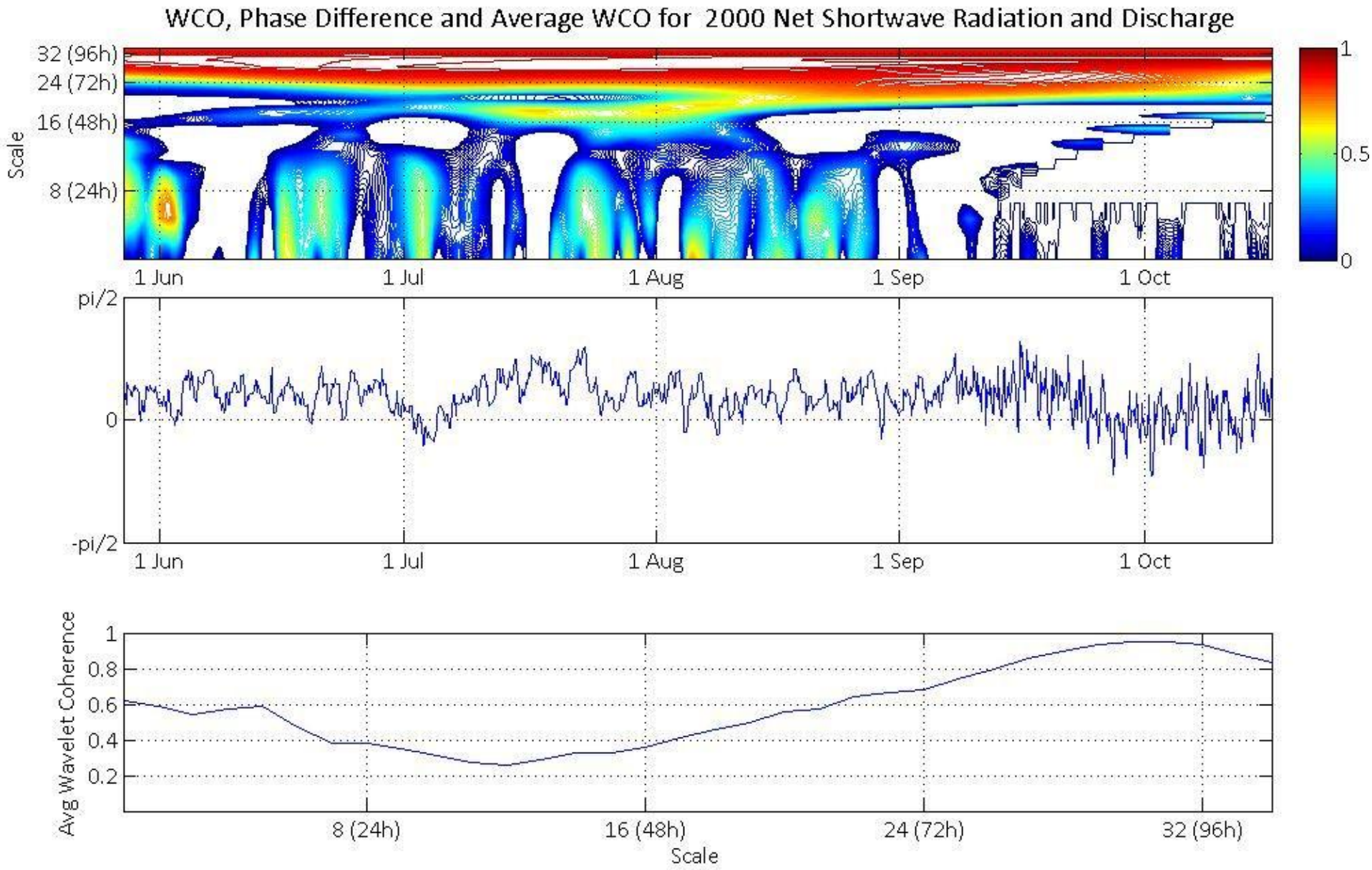
WCO, Phase Difference and Average WCO for 2000 Net Shortwave Radiation and Discharge
Scale
32 (96h)
24 (72h)
16 (48h)
8 (24h)
1
0.5
0
1 Jun
1 Jul
1 Aug
1 Sep
1 Oct
pi/2
0
-pi/2
Avg Wavelet Coherence
1
0.8
0.6
0.4
0.2
8 (24h)
16 (48h)
24 (72h)
32 (96h)
Scale

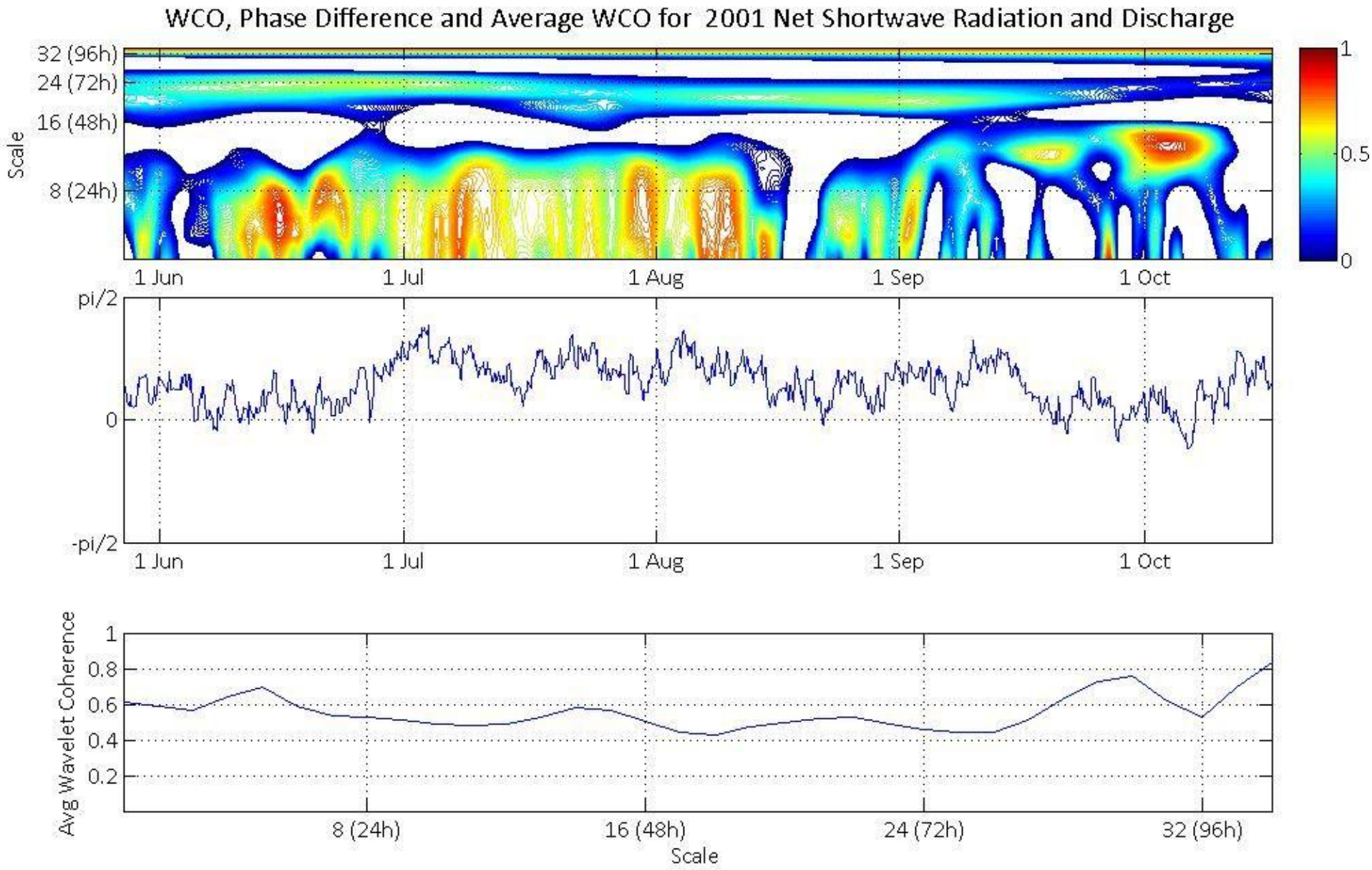
WCO, Phase Difference and Average WCO for 2001 Net Shortwave Radiation and Discharge
Scale
32 (96h)
24 (72h)
16 (48h)
8 (24h)
1
0.5
0
1 Jun
1 Jul
1 Aug
1 Sep
1 Oct
pi/2
0
-pi/2
1 Jun
1 Jul
1 Aug
1 Sep
1 Oct
Avg Wavelet Coherence
1
0.8
0.6
0.4
0.2
8 (24h)
16 (48h)
24 (72h)
32 (96h)
Scale

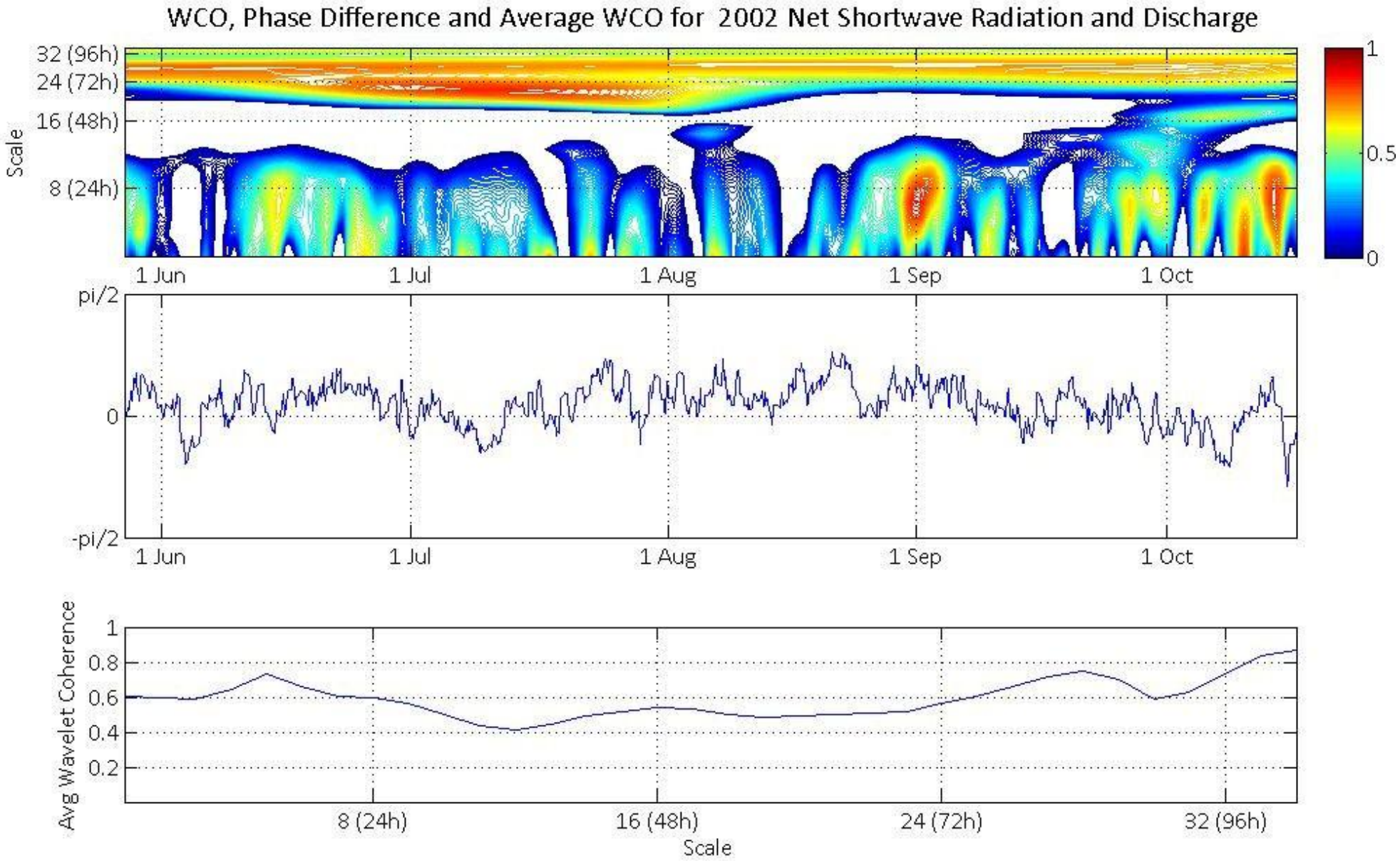
WCO, Phase Difference and Average WCO for 2002 Net Shortwave Radiation and Discharge
Scale
32 (96h)
24 (72h)
16 (48h)
8 (24h)
1
0.5
0
1 Jun
1 Jul
1 Aug
1 Sep
1 Oct
pi/2
0
-pi/2
Avg Wavelet Coherence
1
0.8
0.6
0.4
0.2
8 (24h)
16 (48h)
24 (72h)
32 (96h)
Scale

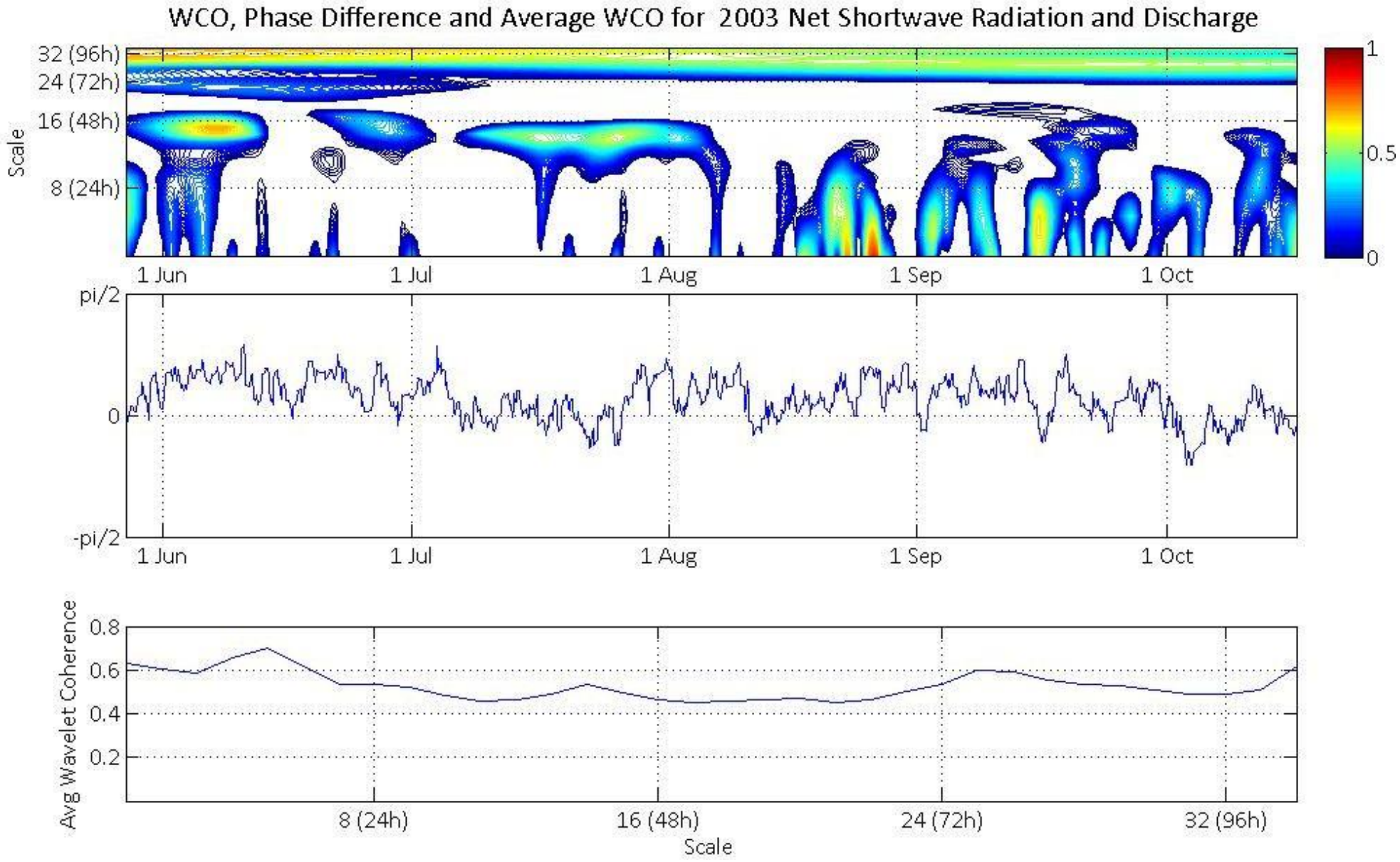
WCO, Phase Difference and Average WCO for 2003 Net Shortwave Radiation and Discharge
Scale
32 (96h)
24 (72h)
16 (48h)
8 (24h)
1
0.5
0
1 Jun
1 Jul
1 Aug
1 Sep
1 Oct
pi/2
0
-pi/2
Avg Wavelet Coherence
0.8
0.6
0.4
0.2
8 (24h)
16 (48h)
24 (72h)
32 (96h)
Scale

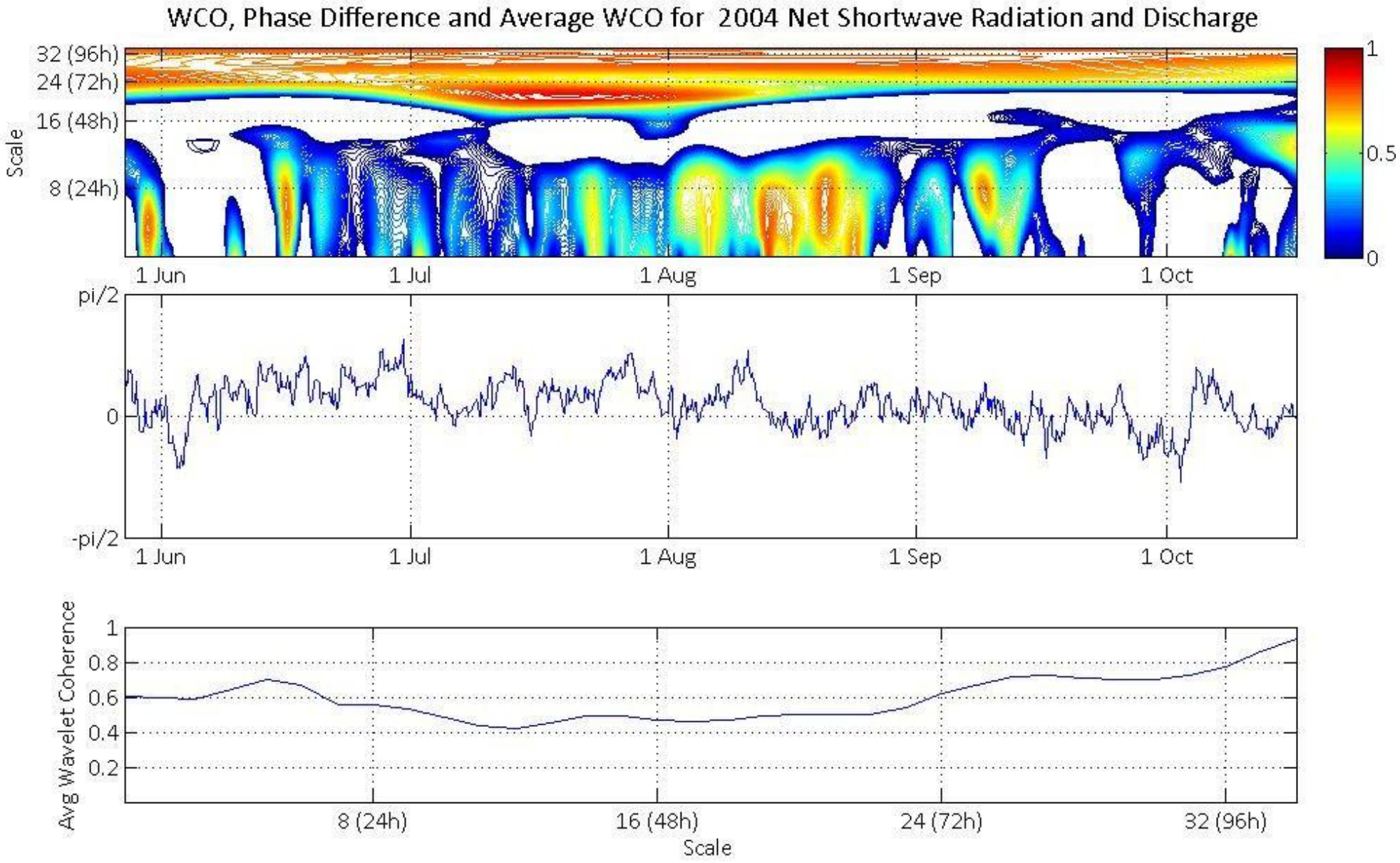
WCO, Phase Difference and Average WCO for 2004 Net Shortwave Radiation and Discharge
Scale
32 (96h)
24 (72h)
16 (48h)
8 (24h)
1
0.5
0
1 Jun
1 Jul
1 Aug
1 Sep
1 Oct
pi/2
0
-pi/2
Avg Wavelet Coherence
1
0.8
0.6
0.4
0.2
8 (24h)
16 (48h)
24 (72h)
32 (96h)
Scale

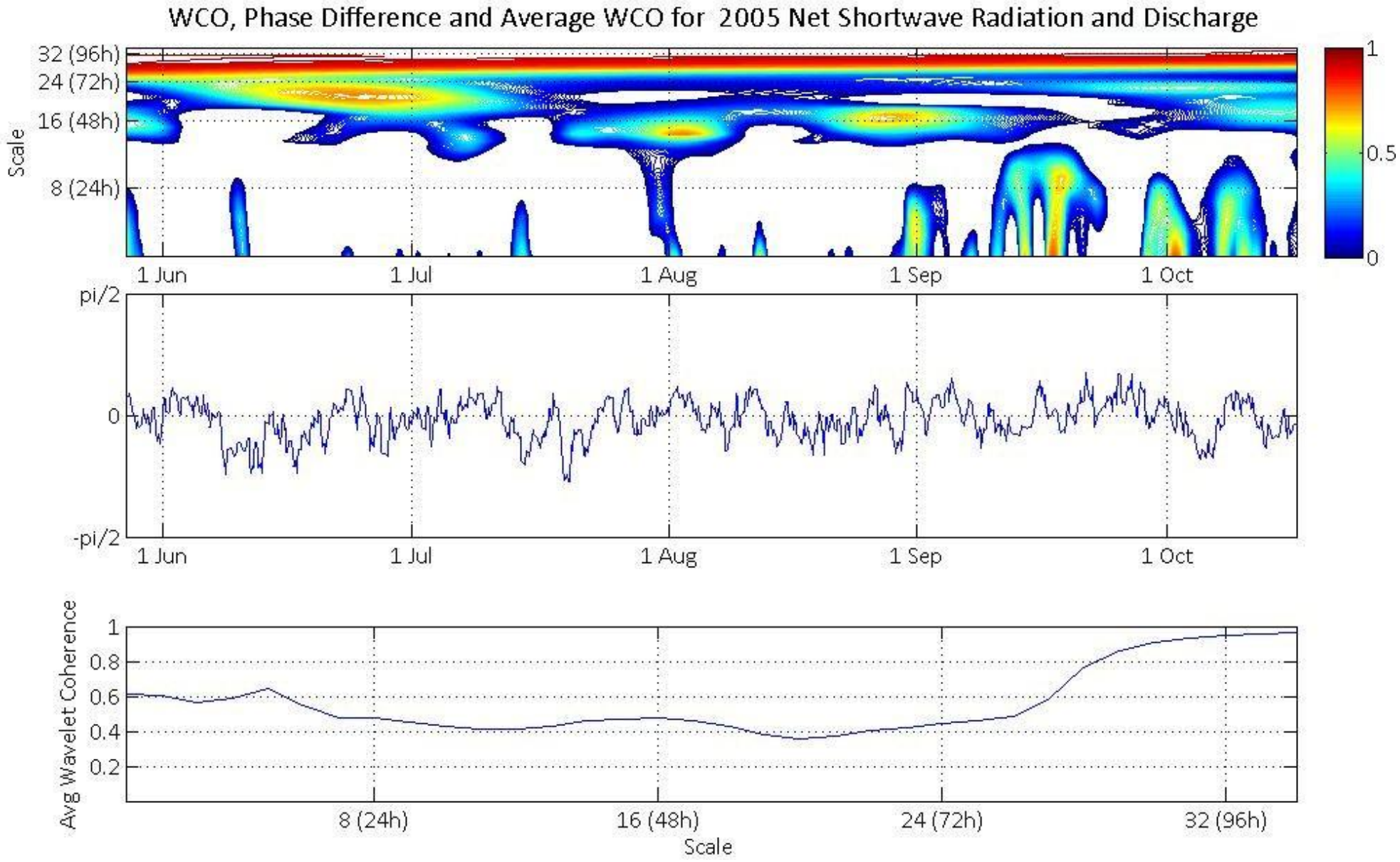
WCO, Phase Difference and Average WCO for 2005 Net Shortwave Radiation and Discharge
Scale
32 (96h)
24 (72h)
16 (48h)
8 (24h)
1 Jun
1 Jul
1 Aug
1 Sep
1 Oct
1
0.5
0
pi/2
0
-pi/2
Avg Wavelet Coherence
1
0.8
0.6
0.4
0.2
8 (24h)
16 (48h)
24 (72h)
32 (96h)
Scale